Reduced-Order Modeling of Turbulent Reacting Flows Using Inertial Manifold Theory

by

Maryam Akram

A dissertation submitted in partial fulfillment
of the requirements for the degree of
Doctor of Philosophy
(Mechanical Engineering)
in The University of Michigan
2021

Doctoral Committee:

Professor Venkat Raman, Chair
Assistant Professor Jesse Capecelatro
Professor Karthik Duraisamy
Associate Professor Eric Johnsen

Maryam Akram
akramrym@umich.edu
ORCID iD: 0000-0002-8409-5435

In the name of Allah, most benevolent, ever merciful.

For my parents, Morteza & Nahid.

ACKNOWLEDGEMENTS

First and foremost, I wish to thank my advisor, Professor Venkat Raman. I am very grateful for the opportunity to join your research team as a Ph.D. student. I have learned so much from you, and this dissertation would not have been possible without you. I am thankful for your intellectual support and insight along the way. I also wish to thank you for your support outside of research. I had many ups and downs during my graduate school, and you have been incredibly supportive and helpful. I always feel that you have my best interests at heart, and I am welcome to seek your advice.

I would like to thank my dissertation committee members, Professors Eric Johnsen, Karthik Duraisamy, and Jesse Capecelatro for their time, advice, and constructive feedback. I truly appreciate your support.

I was lucky to share my graduate school experience with amazing colleagues. Malik, Shivam, Supraj, Takuma, and Yihao, I have learned a lot from all of you. Thank you for the insightful discussions and your technical support. Special thanks to Malik for our long constructive discussions about inertial manifolds. But more importantly, thank you for all the fun time we have had through these years. Shivam and Supraj, thank you for being such amazing friends. Thank you, Shivam for all the weekly hikes and afternoon tea times during the pandemic year.

I want to thank my friends in Ann Arbor. You have been my surrogate family on this side of the planet and an integral part of my life at graduate school. Thank you for your support and all the good memories you made for me.

I want to thank my best friends, Maryam, Haleh, and Zamzam! You have always

been there for me. I love you, and I am truly thankful for having you in my life.

Lastly, I wish to thank my family whom I miss deeply. It has been six years since the last time we were together, but I always felt your love and support in every day and every moment. Negar, you are the funniest sister ever. Anytime I was down, you were there to cheer me up. Maman and Baba, I know these years were not easy for you, but I never heard you complaining about this unjust situation. You have always put my goals and happiness ahead of yours. I love you all, and I am so blessed to have you.

TABLE OF CONTENTS

LIST OF FIGURES

Figure

LIST OF TABLES

Table

LIST OF ABBREVIATIONS

IM Inertial manifold

AIM approximate inertial manifold

PDE partial differential equations

NSE Navier-Stokes equations

Re Reynolds

CFD computational fluid dynamics

DNS Direct numerical simulation

SGS sub-grid scales

RANS Reynolds-averaged Navier-Stokes

LES Large eddy simulation

ADM approximate deconvolution method

ROM reduced-order model

POD proper orthogonal decomposition

PDF probability density function

ODE ordinary differential equation

KSE Kuramoto-Sivashinsky equation

HIT homogeneous isotropic turbulence

ROM Reduced-order models

FDF filtered density function

SOR successive over-relaxation

ILDM intrinsic low-dimensional manifold

CSP computational singular perturbation

ABSTRACT

Turbulent flows found in aerodynamics, propulsion, and other energy conversion systems pose an inherent computational challenge for extensive predictive simulations. Over the last few decades, a statistical approach for reduced-order modeling of turbulence has become the dominant framework for prediction. However, there exists a range of problems that the statistical approaches are ill-suited for – problems driven not only by the chaoticity in the flow, but also by uncertainty in operating, boundary, or initial conditions. Since tails of the initial flow field distribution may drive transition events, there is a need to develop techniques that do not explicitly rely on the statistical representation of unresolved quantities.

The uniqueness of this work lies in the development of reduced-order models that can track distinct trajectories of the dynamical behavior of reacting turbulent flows without invoking ad-hoc assumptions about underlying small-scale turbulent motions or flame structure. Treatment of turbulent flows as finite-dimensional dynamical systems opens new paths for the development of a reduced-order description of such systems. For certain types of dynamical systems, a property known as the inertial manifold (IM) is known to exist, which allows for the dynamics to be represented in a sub-space smaller than the entire state-space. The primary concept in approximate IM (AIM) is that slow dominant dynamical behavior of the system is confined to a low-dimension manifold, and fast dynamics respond to the dynamics on the IM instantaneously. Decomposition of slow/fast dynamics and formulation of an AIM is accomplished by only exploiting the governing equations. Based on this concept, a computational analysis of the use of IMs for modeling reacting turbulent flows is

conducted.

First, the proposed modeling ansatz has been investigated for canonical turbulent flows. An AIM is constructed for the one-dimensional Kuramoto-Sivashinsky equation and the three-dimensional Navier-Stokes equations to assess different aspects of AIM formulation. An *a priori* study is conducted to examine the validity of AIM assumptions and to obtain an estimation of the inertial manifold or attractor dimension. Then a reduced-order model is developed and tested over a range of parameters.

Second, the theory of IM is extended to the development of reduced-order models of turbulent combustion. Unlike pre-generated manifold-based combustion models, here the combustion trajectory is tracked in a low-dimensional manifold determined *in-situ* without invoking laminar flame structures or statistical assumptions about the underlying turbulent flow. The AIM performance is assessed in capturing flame behaviors with varying levels of extinction and reignition.

CHAPTER I

Predictive Simulation of Turbulent Reacting Flows

Environmental concerns necessitate the development and design of efficient and robust modern combustion systems. In energy conversion and propulsion systems, the combustor is the most critical component operating in fragile conditions imposed by the system's environment which are sometimes unfavorable for combustion [5]. Combustors utilize turbulent flows as turbulence enhances transport and mixing of matter, momentum, and heat considerably. As a result, the study of turbulent combustion – a multi-physics process involving mixing, chemical reaction, different heat transfer mechanisms, and phase change – has become a cornerstone in aerospace and propulsion science. The dynamics of these processes reside in a wide range of length and time scales, and resolving their entirety is essential to capture their interaction. Figure 1.1 depicts such interactions in a model aircraft combustor. For flame stabilization, the combustor is equipped with a swirling airflow, and a secondary air injection is used to control emissions. Interaction of swirling flow and side jets creates strong recirculation zones with negative axial velocity in the middle of the combustor. Isolation of flow inside recirculation zones increases the residence time of the flow inside the combustor. This larger residence time then enables soot formation, which is intricately linked to the turbulence-chemistry interactions in turbulent combustion [1].

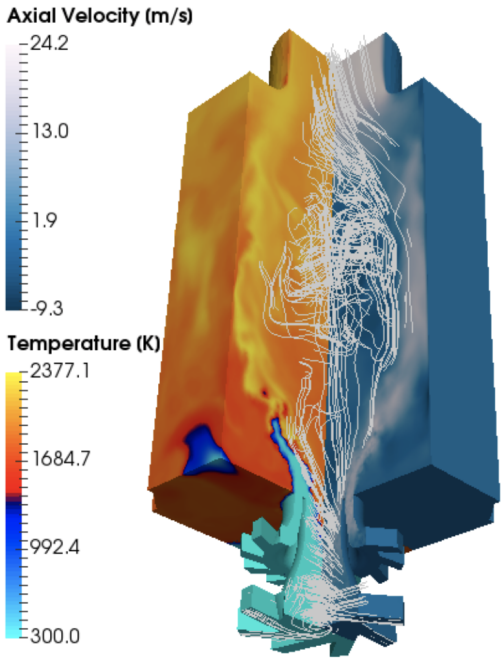

Figure 1.1: Numerical simulation of a model aircraft combustor with swirler and secondary jets. White lines show streamlines [1].

Combustors interact with other components located upstream and downstream in the flow path and experience numerous operating conditions in their lifetime. Reacting flows are governed by nonlinear partial differential equations (PDE) that are sensitive to initial and boundary conditions. A comprehensive study of all possible operating conditions needs numerous simulations. However, characteristics of practical reacting flows impose an inherent computational challenge [6]. So far, the majority of computational analyses of combustion systems have been limited to the design process focusing on specific concerns such as efficiency, emission reduction and strength of materials [7]. An outcome of this focus is that current frameworks are geared towards predicting statistically stationary flows, essentially systems operating at specific design conditions. However, there is a bigger gain to be made by analyzing these complex devices when deviating from the normal behavior, which the statistically stationary formulations by design neglect.

1.1 Transient events

Combustion devices are dominated by chaotic dynamics of turbulence, where small perturbations can grow exponentially leading to different dynamical behavior, including catastrophic failure. There exists a range of problems for which assumptions regarding statistical stationarity are not strictly valid. This includes transient problems such as inlet unstart in scramjets [8, 9] or high-altitude reignition [10, 11], which deal with transition events driven partially by the chaoticity in the flow but are ultimately influenced by uncertainty in operating, boundary, or initial conditions. In these problems, a well-developed turbulent flow may not be present and such an assumption may lead to errors in predicting the probability of transition events. Since tails of the distribution may drive transition events, there is a need to develop or explore techniques that do not explicitly rely on the statistical representation of reacting turbulent flows [7, 12].

Intermittent interactions of turbulence and combustion can cause such transient events, veering the device from its design point. Flame flashback in stationary gas turbines is one example of such events. Lean premixed combustion in gas turbine engines can control low emissions of NOx. However, swirling flow or a bluff body should be used to stabilize the flame and prevent flame blowout. Interaction of chemistry and fluid dynamics can cause an upstream flame propagation into the fuel injection nozzle, namely flame flashback. Flashback has an adverse effect on combustor operation and the durability of the burner. Due to the complex interaction of combustion and turbulence, the flashback is not fully understood; but various mechanisms have been found responsible for flame flashbacks such as combustion instabilities and intermittent low-momentum fluctuations of the core flow [13–15]. In general, a flashback occurs when burning velocity exceeds the flow velocity at least locally. For instance, in boundary layer flashback, the flame takes advantage of the low-momentum near-wall regions to creep upstream into the mixing chamber.

Figure 1.2 shows the experimental investigation of boundary layer flashback of swirling turbulent lean-premixed methane-air flames in a model combustor featuring a mixing tube with center body [2]. Here, the flame front, illustrated by chemiluminescence (blue light), overcomes near-wall low-momentum flow and propagates into the mixing chamber. This process can be triggered by increased fuel to oxidizer ratio, which can be due to the operator's decision about fuel rate or by large fluctuations of the transient airflow. The long presence of flame inside the mixing tube causes severe damages to the combustor.

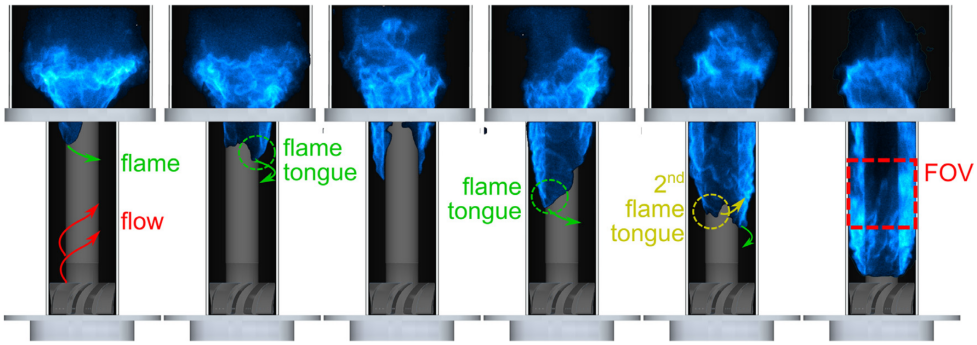

Figure 1.2: Chemiluminescence images of flame flashback in a premixed combustor with center body [2]. Time advances from left to right.

In most cases, unexpected disturbances are imposed by the system's environment and cannot be controlled. The designer's concern is to know if the system will recover from the transient event back into the nominal operating condition, or if it will diverge into another abnormality. For instance, in a flame flashback caused by fluctuations of incoming airflow, the flame can be pushed out of the flashback by an increased flow rate leading to a flame blowout. Figure 1.3 illustrates another intermittent transient event in a lean swirl premixed-combustor, where flame fluctuates intermittently between two states, one attached to the nozzle and the other detached from the nozzle. This intermittency may cause a transition into the detached flame state to eventually lead to flame blow-off [16]. While the reason behind flame fluctuations between the attached and lifted states is not clearly understood, it is hypothesized that perturba-

tions in the boundary conditions of the incoming flow may be the root cause, which further emphasizes the need to deviate from traditional statistical analysis [17]. Such perturbations can cause localized extinction in the flame base, leading to asymmetry in the aerodynamic stabilization of the flame and finally a flame lift-off.

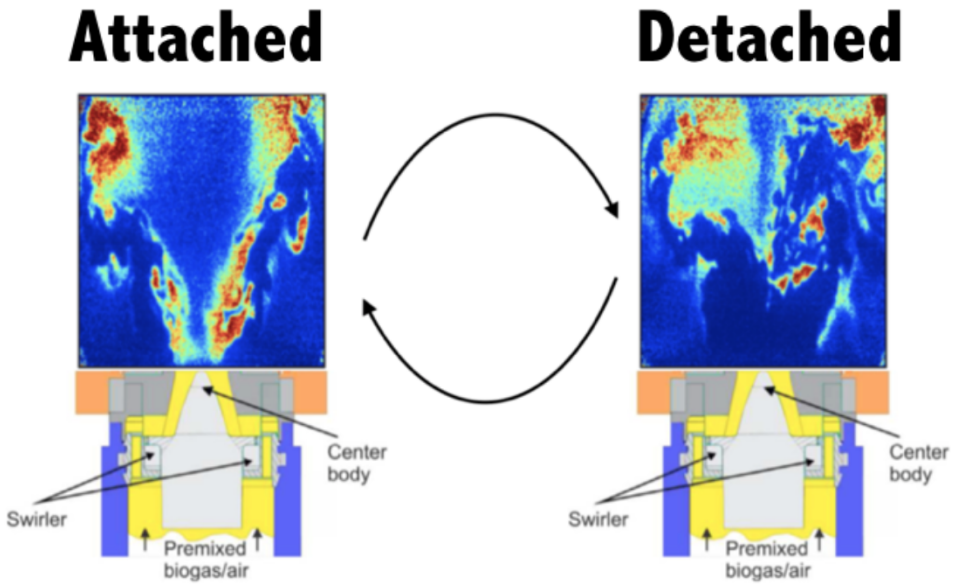

Figure 1.3: Intermittent oscillation of flame in a swirl premixed burner. Flame topology is shown by OH PLIF contours. Left: flame attached to the combustor nozzle. Right: flame detached from the combustor nozzle. Based on experiments of [3] and visualization of [4].

To prevent and control these events, combustion devices are overdesigned. Limited knowledge about triggers of transient events prevents revolutionary design practices in propulsion and energy conversion systems. Full-scale numerical simulation of these systems plays a vital role in the prediction of such events. However, an extensive analysis of all possible operating conditions is computationally expensive and infeasible. Since these systems are dominated by turbulent flows, the focus is on understanding and predicting turbulence.

1.2 Computational challenge

Turbulent flows found in nature and industrial applications are unsteady, irregular, random, and unpredictable. Turbulence is characterized by the significant variation of the velocity field in space and time without any pattern or periodicity. First visualizations of unsteady three-dimensional turbulent structures date back to more than five hundred years ago by Leonardo da Vinci, depicting turbulent eddies over a range of scales. However, a mathematical description of energy cascade from large eddies to smaller ones was provided by Richardson in the 1920s [18].

Turbulent flows consist of eddies of different sizes with various lengths and time scales. The large energy-containing eddies become unstable and break down into smaller eddies, and smaller eddies undergo the same process, turning into even smaller eddies. This process transfers kinetic energy from large scales into smaller scales until eddies are small enough that molecular viscosity dissipates the kinetic energy.

The range of eddy sizes in turbulence is controlled by the balance of inertial and viscous forces, which is quantified by the Reynolds (Re) number. As Re increases and inertial forces become more dominant, the range of scales increases. The large scales of turbulence are influenced by particular geometrical features of the flow. In 1941, Kolmogorov hypothesized that geometric properties of large eddies vanish through energy cascade, and small scales are homogeneous, isotropic, and universal in different flows. Kolmogorov's hypothesis states that at very high Re numbers, the smallest scale of turbulence, namely Kolmogorov scale η, is determined by the rate of energy transfer from large scales and molecular viscosity. Eddies with length scales of the same order as η are stable and get dissipated by viscosity. Then, Kolmogorov parameterized statistical properties of intermediate scales between dissipation range and large scales with only the rate of energy transfer [19, 20]. This intermediate range of scales is called the inertial subrange.

Energy transfer between different scales is due to nonlinear dynamics of the fluid

flow which is governed by the Navier-Stokes equations (NSE). This nonlinearity is the source of the multi-scale nature of turbulence. The inherent assumption in Kolmogorov's description of energy cascade is the local equilibrium of kinetic energy at the interface of eddies with different sizes. In general, it is assumed that smaller eddies adapt quickly to maintain dynamic equilibrium with the large scales production of kinetic energy. This local equilibrium interaction is assumed for eddies in inertial and dissipation ranges. Kolmogorov's theories provide valuable insight into the statistical properties of turbulent flows at very high Re numbers. However, it is now known that even for high Re, small scales are found to be anisotropic [21], and energy transfers in both directions among the scales at rates different from Kolmogorov's estimation [22, 23]. Additionally, Kolmogorov's theories of turbulence cannot predict higher-order statistics of turbulent flows which can expose intermittent effects and rare events [24]. Of these limitations, the latter is critical in engineering applications as discussed in Sec. 1.1. Ultimately, classic theories of turbulence are incapable of capturing such chaotic dynamics characteristic of intermittency and rare events. As such, a paradigm shift is essential for the prediction and control of turbulence in engineering applications.

Navier-Stokes equations describe turbulent motions at all length and time scales under any initial and boundary conditions. However, the NSE solution cannot be parameterized for turbulent flows. Direct methods solve these equations using computational fluid dynamics (CFD) techniques. Direct numerical simulation (DNS) of turbulent flows encompasses the entirety of temporal and spatial scales down to the Kolmogorov scale. For practical high Reynolds number flows the computational cost of DNS scales with Re^3 [25]. Turbulent combustion introduces more challenges to direct methods. Combustion extends the range of scales further; reaction zones can be smaller than the Kolmogorov scale and higher resolution computational grids are needed to capture them. Combustion of practical hydrocarbon fuels involves several

hundred and sometimes thousands of species and chemical reactions [26]. Timescales of these chemical reactions range from nanoseconds to minutes resulting in a stiff system of differential equations [27, 28]. Although advancements in high-performance computing have made invaluable progress in understanding the physics of canonical turbulent flames, DNS of practical reacting flows for extensive operating conditions is intractable due to its escalating computational cost. Reduced-order models (ROM) are essential to alleviate the computational cost of numerical simulation of realistic systems.

The primary ROM in the literature have been developed for turbulent flows, and then extended and modified for combustion systems. Among such methods, coarse-graining approaches are the most implemented because of their ability to resolve dominant motions of turbulent flows directly. These approaches use reconstruction and modeling techniques to account for small scales dynamics. Such models are developed based on turbulence theory and statistical assumptions on the small-scale characteristics. These assumptions are often made in an ad-hoc manner via Kolmogorov's theory of turbulence extended to turbulent flames, even though turbulence theory is valid only in the incompressible constant density cases. The presence of chemical reactions violates the validity of these assumptions [29, 30]. For instance, these models are developed assuming a forward cascade of energy between the scales, but combustion takes place at the molecular scales, and recent studies have shown a backscatter of energy to the larger scales [31, 32]. Moreover, these approaches provide a conditional statistical representation of the system, and they cannot track definite trajectories of the system which may lead to extreme events.

In the field of turbulence, there has been a long history of treating the flow as a chaotic dynamical system [33–35]. Any fluid system described by a set of PDEs can be formulated as a finite-dimensional dynamical system after appropriate spatial discretization. This approach to modeling complex systems has been particularly

successful in weather prediction [36], as dynamical systems-based methods provide access to properties about events that are otherwise difficult to assess using statistical tools. In certain dynamical systems, it is hypothesized that the trajectory followed by the flow in the full-dimensional system is confined to a low-dimensional subspace, known as the attractor of the system. There have been many attempts to characterize the size of this subspace [33–35, 37, 38]. While theoretical scaling suggests that the attractor dimension will increase as Re^n, where $n > 2$ in statistically stationary turbulence [39], more recent numerical studies have concluded that the attractor may be of lower dimensions. For instance, application to the Sandia flame series [38] showed that the dimension is much smaller than the degrees of freedom generated by discretization. In this dissertation, a different approach is used to approximate the attractor of reacting flows by utilizing the notion of inertial manifolds. A reduced-order model is developed for turbulent combustion which can track dynamics of the system on a lower-dimensional subspace without invoking ad-hoc assumptions about the underlying physics of turbulent flames.

1.3 Scope of the dissertation

With the above background, this dissertation investigates the applicability of inertial manifold theories in the development of predictive reduced-order models for turbulent reacting flows. First, a reduced-order modeling approach is constructed for reacting flows described as dynamical systems. Second, the proposed model is studied for turbulent flows and turbulent combustion. The dissertation is organized as follows:

Chapter II: In the next chapter, state-of-the-art approaches in modeling turbulence and turbulent combustion are reviewed. In particular, the limitations and successes of current models are discussed with a focus on transient events. In turbulence modeling, modeling efforts in coarse-graining approaches are reviewed. Then, prevalent methods in turbulent combustion models are discussed.

Chapter III: In this chapter, the theory of inertial manifolds is introduced, and properties of dissipative dynamical systems are discussed. Then, a general description of reacting flows in a dynamical systems framework is presented. Based on the inertial manifolds concept, a reduced-order model for the prediction of reacting flows is proposed. The proposed model can track distinct trajectories of the system in a lower-dimensional space.

Chapter IV: The reduced-order model developed in Chap. III is investigated for turbulent flows. A computational analysis of the use of inertial manifolds for modeling turbulent flows is conducted. Two canonical flows, the one-dimensional Kuramoto-Sivashinsky equation and homogeneous isotropic turbulence with different characteristics and dimensional complexities have been analyzed. The proposed model is tested both *a priori* and *a posteriori*.

Chapter V: The proposed model is tested for an initially non-premixed flame developing in a homogeneous isotropic turbulent field. The thermochemistry parameters of the problem are defined such that the chemical reaction rate is strongly temperature-dependent, and the interaction of turbulence mixing and chemical reaction results in different flame behaviors from equilibrium burning to localized extinction and reignition and finally global extinction. The modeling approach is investigated in the prediction of the dynamic interplay of micro-mixing and chemical reactions.

Chapter VI: In this chapter, the findings of this dissertation work are summarized. Concluding remarks about the dynamical system-based modeling approach are presented in this chapter. Finally, suggestions for continuing this work in the field of fluid dynamics and combustion and other engineering systems are discussed.

CHAPTER II

Reduced-Order Modeling of Multi-Scale Multi-Physics Problems

Modern combustion systems are dominated by turbulent flows and their chaotic behavior. Hence, turbulence modeling sets the ground for modeling other physical processes in these multi-physics systems. In this chapter, various approaches in turbulence modeling are reviewed, and their limitations and strengths are discussed. Then, combustion models are discussed. The goal of this chapter is to assess these models in the context of systems deviating from their design point.

2.1 Turbulence modeling

Computational analysis of turbulence is shadowed by the curse of dimensionality. Any attempt in turbulence modeling starts with the reduction of scales by projecting the dynamics of the entire flow field into a lower-dimensional space. Let $\mathcal{V}$ be the Hermitian space containing all possible realizations of the flow field, and $\boldsymbol{v}$ be an element of $\mathcal{V}$ describing the entire turbulent field governed by a set of partial differential equations,

$$\frac{\partial \boldsymbol{v}}{\partial t} = \mathcal{L}(\boldsymbol{v}) + \mathcal{N}(\boldsymbol{v}),\ \boldsymbol{v} \in \mathcal{V},\ t \in (0, t), \tag{2.1}$$

subject to the proper boundary and initial conditions. Here $\mathcal{L}$ and $\mathcal{N}$ are linear and nonlinear operators respectively, where the latter is the source of nonlinearity engaging all of the scales. Dimension-reduction can be achieved by projecting the entire flow field into a lower-dimensional space. Assume projection $\boldsymbol{P} : \mathcal{V} \rightarrow \mathcal{U}$, where $\mathcal{U}$ is not necessarily a subspace of $\mathcal{V}$. By applying projection $\boldsymbol{P}$ to Eq. 2.1, the governing equations of motions in the reduced system can be obtained,

$$\boldsymbol{P}\frac{\partial \boldsymbol{v}}{\partial t} = \boldsymbol{P}\mathcal{L}(\boldsymbol{v}) + \boldsymbol{P}\mathcal{N}(\boldsymbol{v}),\ \boldsymbol{P}\boldsymbol{v} \in \boldsymbol{P}\mathcal{V},\ t \in (0,t). \tag{2.2}$$

Let $\boldsymbol{u} = \boldsymbol{P}\boldsymbol{v}$ be an element of $\mathcal{U}$, describing the flow field in the reduced space. Thus, Eq. 2.2 can be written as

$$\frac{\partial \boldsymbol{u}}{\partial t} = \mathcal{L}(\boldsymbol{u}) + \boldsymbol{P}\mathcal{N}(\boldsymbol{v}),\ \boldsymbol{u} \in \mathcal{U},\ t \in (0,t), \tag{2.3}$$

assuming the projection operator is time-invariant, and the projection operator and linear operator $\mathcal{L}$, commute. The validity of these assumptions depends on the choice of the projection $\boldsymbol{P}$, and will be discussed for each modeling ansatz. Equation 2.3 describes evolution of the flow field in a lower-dimensional space $\mathcal{U}$. However, it still depends on the flow field realization in the original higher-dimensional space $\mathcal{V}$, because the projection operator and nonlinear operator do not commute,

$$\boldsymbol{P}\mathcal{N}(\boldsymbol{v}) \neq \mathcal{N}(\boldsymbol{P}\boldsymbol{v}). \tag{2.4}$$

This gives rise to the typical closure problem faced by all nonlinear multi-scale modeling approaches. Adding and subtracting $\mathcal{N}(\boldsymbol{u})$ to and from Eq. 2.3 gives,

$$\frac{\partial \boldsymbol{u}}{\partial t} = \mathcal{L}(\boldsymbol{u}) + \mathcal{N}(\boldsymbol{u}) + \big[\boldsymbol{P}\mathcal{N}(\boldsymbol{v}) - \mathcal{N}(\boldsymbol{u})\big],\ \boldsymbol{u} \in \mathcal{U},\ t \in (0,t). \tag{2.5}$$

The bracketed term in Eq. 2.5 contains the full-state solution, $\boldsymbol{v}$, which is an unknown variable in the reduced system. This unclosed term in Eq. 2.5 should be replaced by a model depending only on the projected variable $\boldsymbol{u}$,

$$\frac{\partial \boldsymbol{u}}{\partial t} = \mathcal{L}(\boldsymbol{u}) + \mathcal{N}(\boldsymbol{u}) + \Phi(\boldsymbol{u}),\ \boldsymbol{u} \in \mathcal{U},\ t \in (0, t). \tag{2.6}$$

Here, $\Phi(\boldsymbol{u})$ is a mapping from $\mathcal{U}$ to itself, containing the effect of scales discarded by the projection operator $\boldsymbol{P}$. In Eq. 2.6, $\mathcal{L}$ and $\mathcal{N}$ are some approximations of the respective operators in Eq. 2.1.

For brevity of arguments, $\mathcal{V}$ and $\mathcal{U}$ have been referred to as full space and resolved space respectively in the rest of this thesis. The space containing all the scales removed by the projection operator is called the unresolved space. Depending on the choice of projection operator and the modeling approach accounting for the unresolved space, turbulence models fall into several categories. The most common modeling strategies will be discussed here.

2.1.1 Reynolds-Averaged Navier-Stokes

In the Reynolds-averaged Navier-Stokes (RANS) approach, the projection operator is an averaging operator (either ensemble or temporal averaging) which decomposes the flow field into mean flow properties and their fluctuations. The projection operator affects all length scales, hence all scales in RANS are modeled. The goal is to reproduce statistics of the ensemble average of the flow field. To close the governing equations of mean flow evolution, the impact of turbulence fluctuations containing all information about turbulence unsteadiness has to be modeled. RANS models vary from algebraic relations added to the equations of motions of the mean flow to solving additional transport equations. DNS and recently data-driven approaches have been used to tune RANS model parameters [40], but these models have shown to be inaccurate when

turbulent flow deviates from the design conditions of such models. RANS models lack universal parameters, and model coefficients are pre-determined based on the flow configuration used as the validation set in model development. When flow behavior deviates from these configurations, those parameters are not valid anymore, and there is no mechanism for changing parameters during the simulation. RANS models have been used heavily for the simulation of practical turbulent flows because, unlike scale-resolving approaches, the computational cost of the RANS approach does not scale with Reynolds number. Since the focus of this dissertation is on scale-resolving approaches, RANS models will not be discussed further here.

2.1.2 Large Eddy Simulation

Large eddy simulation (LES) resolves the large energy-containing motions of turbulence directly, while the effects of small eddies are modeled. In LES, spatial filtering is applied to the instantaneous turbulent field to separate resolved and unresolved scales, such that all turbulent motions smaller than the filter width (Δ), are removed and need to be modeled. The premise of LES was built by Smagorinsky for atmospheric flows [41], and then it has been adapted for turbulent flows [42, 43]. The spatial decomposition implied by LES conforms with turbulence characteristics such as the cascade of energy from large scales to the smaller scales, and large scales dominating macroscopic features of turbulence. Unlike RANS, LES can capture three-dimensional unsteady structures of turbulence albeit at a higher computational cost. LES can also exploit computing power advancements by refining the filter width and resolving more scales, effectively bridging the gap between RANS and DNS in both computational cost and scale-resolving capabilities. Recent advancements in high-performance computing has made LES the frontier in turbulence modeling approaches [44–46].

Following the nomenclature in Sec. 2.1, the projection $\boldsymbol{P}$ in LES represents a spatial filtering kernel, such as Gaussian or sharp spectral filters, which acts as a

low-pass filter and attenuates scales smaller than the filter width. It is the effect of these sub-grid scales (SGS) on the resolved scales that need to be modeled. The general filtering operation was first introduced by Leonard [47] as the convolution of time-invariant spatial filters with the entire flow field,

$$\boldsymbol{u} = \int \mathcal{G}(r, \boldsymbol{x})\boldsymbol{v}(\boldsymbol{x} - r, t)\ \mathrm{d}r, \tag{2.7}$$

and the unresolved or subfilter field is defined as

$$\boldsymbol{w} = \boldsymbol{v} - \boldsymbol{u}. \tag{2.8}$$

Assuming that the filter kernel $\mathcal{G}$ is homogeneous and independent from $\boldsymbol{x}$, it commutes with differentiation. By applying the filtering operation to the Navier-Stokes equations, governing equations for the filtered (resolved) variables can be obtained in the form of Eq. 2.5,

$$\frac{\partial u_i}{\partial t} = -\frac{\partial \mathcal{G}(v_i v_j)}{\partial x_j} - \frac{\partial p}{\partial x_i} + \frac{1}{Re}\frac{\partial^2 u_i}{\partial x_j \partial x_j}, \tag{2.9}$$

where v_i and u_i are the entire and filtered velocity components in the i^{th} direction respectively, p is the filtered pressure field and Re is the Reynolds number. The first term on the right-hand side of this equation cannot be computed based on the filtered field quantities and is unclosed. Equation 2.9 can be written as

$$\frac{\partial u_i}{\partial t} = -\frac{\partial (u_i u_j)}{\partial x_j} - \frac{\partial p}{\partial x_i} + \frac{1}{Re}\frac{\partial^2 u_i}{\partial x_j \partial x_j} - \frac{\partial \tau_{ij}}{\partial x_j}, \tag{2.10}$$

where

$$\tau_{ij} = \mathcal{G}(v_i v_j) - u_i u_j. \tag{2.11}$$

The subfilter stress tensor, τ_{ij}, is a function of the unfiltered field and needs to be modeled.

Various LES approaches deal with filtering operation and closure of subgrid stress tensor differently. The projection or filtering operation can be done either explicitly or implicitly. In explicit filtering, scale decomposition is achieved by convolution of a filtering kernel with the governing equations. Hence, the kernel function appears in the governing equations of the filtered field. This approach provides more control over the numerics of LES and makes filter width independent from the computational grid spacing and numerical algorithm convergence. By refining filter width, LES resolves more scales and converges to an LES solution independent from the filter width. However, explicit filtering reduces the effective resolution of LES and cannot leverage available computing power entirely.

In implicit filtering, the filtering operator is defined implicitly based on the numerics of the simulation and LES grid resolution. The computational grid represents the resolved scales, and unresolved scales are not represented in the domain. Particularly, implicitly-filtered LES is an under-resolved turbulent simulation that uses additional terms to account for the SGS contributions to the resolved scales. Since the filter kernel does not appear in the governing equations, the implementation of different numerical approaches is easier. For a given computational grid, limited by the computing power, implicitly-filtered LES resolves more scales and has lower numerical errors. Refining filter width is equivalent to the refinement of the computational grid and convergence to a model-free DNS solution.

Modeling unresolved or subgrid scales in LES can also be done either explicitly or implicitly. In explicit modeling approaches, a subgrid-scale model is used to account for the effect of SGS, while in implicit modeling no subgrid-scale model is used. Dissipative characteristics of the numerical discretization approach account for the effects of SGS, assuming their contribution is purely dissipative. Table 2.1 compares different LES approaches, where $\mathcal{G}_\Delta(\boldsymbol{x})$ is the spatial filtering kernel, Δ is filter width and $\Delta_{\boldsymbol{x}}$ is grid spacing of computational domain.

LES approach in filtering/modeling	**Δ and $\Delta_{\boldsymbol{x}}$ relation**	**Governing equation of LES**
Explicit/Explicit	$\Delta_{\boldsymbol{x}} < \Delta$	$\frac{\partial \boldsymbol{u}}{\partial t} = \mathcal{L}(\boldsymbol{u}) + \mathcal{G}_{\Delta}\mathcal{N}(\boldsymbol{u}) + \Phi(\boldsymbol{u})$
Explicit/Implicit	$\Delta_{\boldsymbol{x}} < \Delta$	$\frac{\partial \boldsymbol{u}}{\partial t} = \mathcal{L}(\boldsymbol{u}) + \mathcal{G}_{\Delta}\mathcal{N}(\boldsymbol{u})$
Implicit/Explicit	$\Delta_{\boldsymbol{x}} = \Delta$	$\frac{\partial \boldsymbol{u}}{\partial t} = \mathcal{L}(\boldsymbol{u}) + \mathcal{N}(\boldsymbol{u}) + \Phi(\boldsymbol{u})$
Implicit/Implicit	$\Delta_{\boldsymbol{x}} = \Delta$	$\frac{\partial \boldsymbol{u}}{\partial t} = \mathcal{L}(\boldsymbol{u}) + \mathcal{N}(\boldsymbol{u})$

Table 2.1: Comparison of various LES formulations.

LES of practical flows has been dominated by implicitly-filtered explicitly-modeled approaches. In such efforts, only filter width appears in the SGS modeling of LES. *A priori* studies have shown that interaction of subgrid and resolved scales depends on the choice of filter [48, 49], but this has been ignored in practical LES applications. Spatial filters work very well for the decomposition of homogeneous flows, but in the case of more complex geometries, non-uniform filters should be used. These filters do not commute with spatial differentiation, and they introduce additional unclosed terms [50, 51]. The success of LES in the prediction of turbulent flows in various applications is due to the direct simulation of macroscopic features which are controlled by large energy-containing scales. However, the prediction of large-scale evolution requires accurate modeling of the effect of small scales.

2.1.2.1 Sub-grid scale modeling in LES

Initially, SGS models for LES have been adapted from RANS modeling approaches which yielded better results because the resolved part of the flow in LES is predicted more accurately. Although various approaches have been developed for SGS modeling, the inherent assumption among them is local equilibrium between resolved and unresolved scales. Local equilibrium assumes that the production of kinetic energy at resolved scales balances its dissipation at SGS, and small scales are only responsible

for the forward cascade of energy to the molecular level where kinetic energy is finally dissipated by viscosity. In general, LES models consider universal characteristics for small-scale features of turbulent flows in different applications. In particular, small-scale structures are assumed to be homogeneous and isotropic. Such assumptions are valid in fully-developed, unbounded high Reynolds number turbulent flows. In many applications, turbulent flows are transitional at relatively low Reynolds numbers and/or wall-bounded, and such assumptions are violated. Research in LES modeling has tackled many of such limitations by relaxing these assumptions selectively. For instance, wall models are introduced to account for momentum transfer by small scales in near-wall regions [43, 49]. Some of the more prevalent LES modeling approaches are discussed below.

Eddy-viscosity models

Eddy viscosity models are the predominant models in LES practices. These models are based on the turbulent-viscosity hypothesis introduced by Boussinesq in 1877 [52]. According to this hypothesis, turbulence responds to straining effects rapidly, analogous to viscous stress in molecular processes. It also assumes that this response is linearly proportional to the strain rate of the flow. Hence, the sub-grid stress tensor can be modeled as

$$\tau_{ij} = -\nu_T\left(\frac{\partial u_i}{\partial x_j} + \frac{\partial u_j}{\partial x_i}\right) \tag{2.12}$$

where ν_T is the eddy viscosity that needs to be specified. Equation 2.12 implies that stress tensor and strain rates are perfectly aligned and correlated by a scalar, the eddy viscosity. This assumption is not generally true even for simplest turbulent flow configurations [53, 54]. The eddy viscosity was first modeled by Smagorinsky [41],

$$\nu_T = (C_s\Delta)^2(S_{ij}S_{ij})^{0.5} \tag{2.13}$$

where C_s is a constant, and S_{ij} is the rate of strain tensor of the resolved field,

$$S_{ij} = \frac{1}{2}\left(\frac{\partial u_i}{\partial x_j} + \frac{\partial u_j}{\partial x_i}\right). \tag{2.14}$$

The constant C_s needs to be specified *a priori*, and it is either derived from theoretical analysis such as Kolmogorov cascade or tuned by DNS or experimental data [55, 56]. Hence prior knowledge about the turbulent regime and small scales statistics is required, which is limiting for practical turbulent flows in complex geometries. Even for canonical flows, studies have shown discrepancies between parameters obtained from exact measurements and theoretical approaches, and theoretical values are shown to be too dissipative [57, 58]. Unlike theoretical expectations, filter width rarely lies in the inertial subrange of turbulent scales, or turbulence is not fully developed to sustain such inertial range, which explains such discrepancies. Even with an appropriate specification of the model parameter, the Smagorinsky model fails to capture backscatter, transfer of energy from subgrid scales to the resolved scales [59, 60]. This is particularly important in transitional flows and near-wall regions, where small scales transfer momentum to the large scales [61, 62].

Dynamic modeling procedure

LES modeling has leaped forward by dynamic modeling procedures which can determine model parameters *in situ*. Following the Germano identity [63], dynamic modeling assumes any physical characteristic of the flow is independent of filter width. Therefore, information at resolved scales can be used to determine model coefficients. By applying a second filtering operation with larger filter width ($\mathcal{G}_{\alpha\Delta}, \alpha > 1$), the LES field is coarse-grained. Then, considering the SGS model is a function of filter width and a vector of parameters $\boldsymbol{C}$, the Germano identity implies

$$\widehat{\Phi}(\boldsymbol{u}, \Delta, \boldsymbol{C}) = \Phi(\widehat{\boldsymbol{u}}, \alpha\Delta, \boldsymbol{C}), \tag{2.15}$$

where $\widehat{\cdots}$ denotes the second filtering operation. Equation 2.15 involves fields at resolved scales that are available in LES, and model parameters can be determined as a function of time and space during the simulation. Dynamic modeling procedures can capture local features of small scales and relax the homogeneity and universality assumptions to some extent. Considering the Germano identity for the Smagorinsky subgrid-scale model, Lily provided a minimization problem for finding the Smagorinsky constant dynamically [64]. Dynamic Smagorinsky models have overcome many shortcomings of the original model. For instance, dynamic modeling can capture near-wall structures, and unlike original Smagorinsky it is not too dissipative in transitional flows [61, 65]. However, there are some mathematical and implementational challenges for dynamic modeling in practical problems. To solve Eq. 2.15 for model parameters, it is assumed that parameters commute with filtering, but when the dynamically determined coefficient varies spatially strongly this assumption is violated. Besides, in many applications model parameters are not scale-independent, and the location of the filter width in turbulent scales affects dynamic parameter determination directly [66]. Moreover, stability issues can occur when dynamic procedure predicts large negative values of Smagorinsky constant and unphysical backscatter of energy to the large scales. Attempts to fix these issues lead to again limiting the locality of dynamic models.

Scale similarity approaches

Scale similarity model (SSM) [67] approximates the SGS stress tensor by applying a second spatial filtering operation to the LES field, similar to the dynamic modeling procedure. However here the proportionality constant in Germano identity is determined to reproduce the exact average SGS kinetic energy. The premise of SSM is that the contribution of the small resolved scales to the large resolved scales is similar to the contribution of the unresolved scales to the small resolved scales. SSM predicts the correct rate of energy flux to the subgrid scales and backscatter of energy reason-

ably. Unlike eddy viscosity models, SSM cannot predict adequate SGS dissipation, and an additional relaxation regularization is required. Bardina et al. proposed a mixed-model of scale-similarity and eddy-viscosity models to account for the twofold SGS contribution: 1) energy transfer from large scales, and 2) dissipation of energy contained in the SGS [68]. This model has a superior performance in transitional flows, but the ratio of each component of the SGS model needs to be determined either *a priori* or during the simulation by assuming some form of equilibrium between production and dissipation of kinetic energy at filter width.

Higher fidelity approaches try to approximate the unfiltered field or its local quantities of interest from the information at the resolved scales without invoking the universality and homogeneity of the subgrid field. These models are developed mostly on the scale similarity premise, i.e. the contribution of the small resolved scales to the large resolved scales is similar to the contribution of the unresolved scales to the small resolved scales. These models do not suffer from limiting assumptions of eddy-viscosity models, and they can predict backscatter of energy without any adverse effects on numerical stability [69–72].

Approximate deconvolution models

A generalized form of the scale similarity model with repeated filtering is the approximate deconvolution method (ADM) [73]. In ADM, the unfiltered field is recovered using the information of the LES field. Hence, nonlinear terms of the governing equation of the LES field can be computed directly, and the closure problem is solved. To reconstruct the unfiltered field, it is assumed that the filtering operator (projection $\boldsymbol{P}$) is invertible, and by applying its inverse to the filtered (LES) field, the entire flow field can be recovered. Assuming $\boldsymbol{Q} = \boldsymbol{P}^{-1}$ as the inverse of the filtering operator, the unfiltered flow field can be recovered as

$$\boldsymbol{v}^* = \boldsymbol{Q}\boldsymbol{u}. \tag{2.16}$$

However, compact practical filters used in LES formulations are noninvertible, and an approximation to $\boldsymbol{Q}$ is essential. The inverse operator is approximated by assuming $\boldsymbol{P}$ has an inverse and it can be expanded by an infinite series. The series can be truncated at n as an approximation of $\boldsymbol{P}^{-1}$,

$$\boldsymbol{Q} = \boldsymbol{P}^{-1} = \sum_{i=0}^{n} (\boldsymbol{I} - \boldsymbol{P})^i, \tag{2.17}$$

which requires the convergence criteria: $||\boldsymbol{I} - \boldsymbol{P}|| < 1$, where $\boldsymbol{I}$ is the identity operator. This approximation imposes a computational challenge to the ADM approach as the series convergence rate is slow. To balance accuracy and computational cost, $n < 5$ is usually considered. The approximated inverse filtering operator $\boldsymbol{Q}$ is repeated filtering of the filtered field, and if the filtering operator is an orthogonal operator, such as the sharp spectral filter, it cannot recover any information beyond the cut-off wavenumber. The ADM approach can recover only part of the information lost by convolution of the filtering operator with resolved scales. In wavenumber space, the inverse operator affects only scales between the filter wavenumber and the Nyquist wavenumber of the computational grid. Therefore, it is essential to implement ADM with explicitly filtered LES or use a grid spacing smaller than the filter width in implicitly filtered LES. The unfiltered field cannot recover any information of the scales smaller than the grid spacing, and the effect of these scales cannot be modeled by just replacing the unfiltered field $\boldsymbol{v}$ by the recovered field $\boldsymbol{v}^*$ in the nonlinear term of the LES governing equations (Eq. 2.9).

To model interaction between resolved field and unrepresented sub-grid scales, another modeling component is introduced to ADM. In one approach, a dissipative term is added to the LES governing equations to remove energy transferred from the resolved scales to the nonrepresented field [74]. Since this relaxation term is purely dissipative, it cannot account for the local backscatter of energy from the unresolved

scales to the LES field. Also, the rate of dissipation needs to be determined by trial and error at each time step. In another study, these shortcomings of ADM are addressed by matching specific subgrid moments of the true field [75, 76]. However, this approach requires the exact shape of the energy spectrum in the subgrid range, which is assumed *a priori*.

The deconvolution approach is particularly interesting since it extracts unresolved fields directly from the resolved fields, implying that a single unresolved field is linked to each resolved field. This is a simplification of the ideal LES formulation of Langford and Moser [77], in the sense that the optimal evolution is obtained by assuming that the distribution of sub-filter fields for a given filtered field is a delta function. Approximate deconvolution methods provide a mathematical framework to recover the subgrid scales, compute the nonlinear term directly and close the LES governing equations, but there are some underlying mathematical issues to be addressed. Questions such as how much of the unresolved information can be recovered, or whether the ADM approximation of the inverse of the filter is justified should be addressed. In LES, the spatial filtering operator maps the infinite-dimensional solution to a lower-dimensional space. Depending on the type of filter and numerical implementation, the LES field is not necessarily a subspace of the original field. For instance, in the case of the sharp spectral filter and Galerkin methods, the LES field is a subspace of a full-dimensional system. But this is not true for box filters and finite difference schemes. In any case, if deconvolution of the filter can recover all of the discarded information, then the LES field is identical to the unfiltered field; it is only represented by a different set of basis functions. This is more apparent when the LES field is a subspace of a full-dimensional system. In this case, if the filtering operator is an orthogonal projection, nothing can be recovered from the unresolved scales; and if the projection is an oblique projection, deconvolution can at best recover the parallel component of the complement space.

There exist other LES modeling approaches that do not rely on traditional spatial

filters for the separation of scales. Such models use projection-based decomposition for scale separation. For instance, variational multi-scale LES uses a variational projection to decompose the range of scales in groups of large resolved scales, small resolved scales, and unresolved scales [78, 79]. In this approach, the direct contribution of the SGS physics is confined to the small resolved scales, and large resolved scales are solved directly, i.e. without any modeling, but influenced indirectly by the subgrid-scale model due to the inherent coupling of all scales. This approach provides a robust scale separation for wall-bounded flows, where inhomogeneous spatial filters are avoided. It also does not require near-wall modeling of small-scales decay [80].

The above discussion has been limited to constant density flows. However, variable-density low-Mach number flows and compressible flows are ubiquitous in engineering applications. In particular, turbulent combustion requires a variable-density formulation of the Navier-Stokes equations. Subgrid scale models have been extended for variable-density and compressible flows [81, 82]. The goal of LES is resolving only the large energy-containing scales, while the effect of small scales is modeled. Modeling the physics of the smallest scales reduces the computational cost significantly, allowing analysis of high Re number flows both in canonical and practical geometries [83, 84]. LES success in accurate prediction of large-scale features of turbulent flows has been extended to modeling of other physical phenomena such as turbulent combustion [85]. Although LES provides an unsteady three-dimensional description of flow, it is still an optimized statistical representation of large-scale flow dynamics [77]. LES models the contributions of small scales represented by an ensemble average of all possible sub-grid fields for a distinct resolved field. In many applications, there is an interest in distinct realizations of the large-scale flow motions, specifically when the trajectory of the system deviates from normal behavior. In this sense, LES cannot track definite trajectories of the system which may lead to extreme events.

2.1.3 Data-driven approaches

Recent advancements in high-performance computing and experimental techniques have generated abundant data sets of turbulent flows in various applications. Leveraging data in turbulence modeling is not recent though; DNS results or experimental data have been used for tuning model parameters and validation purposes in RANS and LES approaches for decades. With advancements in machine learning techniques, the calibration process has been generalized to the model itself rather than being limited to its parameters, and a stochastic representation of models for the unresolved scales has been achieved. In addition to model calibration, data has been exploited to identify and quantify uncertainties in structures of turbulence models and their parameters [40, 86].

With the development of more efficient statistical inference algorithms and access to large data sets, data-driven approaches have been developed to fit more complex functional forms of models [87–89]. Other studies have investigated reconstruction of the unfiltered field from the information at resolved scales using deep learning generative models, similar to approximate deconvolution methods [90, 91].

Besides exploiting data for turbulence closure modeling, data-driven techniques have been used to identify coherent structures of turbulent flows and derive ROMs. Among these data-driven ROMs, proper orthogonal decomposition (POD) methods are the most common, where data sets are post-processed to decompose dynamics of the Navier-Stokes equations into energetic coherent structures and residual scales [92–94]. In other studies, neural networks are trained to extract spatio-temporal structures of turbulence and predict temporal evolution of turbulent field [95]. Data-driven approaches provide invaluable insight into turbulence modeling and identifying coherent structures of turbulence. However, they face several challenges such as availability of consistent data and observing physical constraints [86]. Finally, they only provide stochastic representations of the flow field that have been optimized in

some form.

2.1.4 Dynamical systems-based ROMs

Projection-based scale separation provides a theoretical framework for model reduction largely used in dynamical systems. Any fluid system described by a set of partial differential equations can be formulated as a finite-dimensional dynamical system after appropriate spatial discretization. This approach to modeling complex systems has been particularly successful in weather prediction [36], as dynamical systems-based methods provide access to properties about events that are otherwise difficult to assess using statistical tools. From a theoretical perspective, the focus has been on the structure of the dynamical system in phase space, which is composed of the N-dimensional state space defined by the degrees of freedom describing the discretized system. The spatial and temporal evolution of the turbulent flow can then be expressed as a trajectory in this state space.

In certain systems dominated by coherent structures, the long-time behavior of the system is dictated by dynamics confined to a low-dimensional subspace of the full N-dimensional state space. All trajectories of the system are attracted to this low-dimensional manifold, which contains the attractor of the system [96–98]. Constantin et al. [97] showed that the dimension of the attractor scales nonlinearly with the Reynolds number of the flow. However, direct estimations of this attractor dimension for turbulent flows using the Kaplan-Yorke conjecture [99] showed that attractor dimensions are orders of magnitude lower than the number of degrees of freedom required by DNS [38, 100].

In this regard, it is interesting to note that one of the original premises for the use of dynamical systems is the development of reduced-order models, but this approach has been fraught with challenges for the following reasons [101]. First, the possible high-dimensionality of the attractor led to the conclusion that a highly reduced model

cannot be easily determined [102]. Second, phenomenological approaches such as the intermittency model [103] did not directly provide a path to other spatially extended systems. Finally, there have been fundamental theoretical issues as to whether such reduced models can capture the chaoticity of the flow [101]. In light of these challenges, the recent focus on data-driven sciences has renewed interest in dynamical systems-based modeling of turbulent flows [104–106]. For instance, techniques for describing turbulent boundary layers have been formulated from these reduced-order modeling concepts [107].

The reduced-order description of reacting turbulent flows proposed in this dissertation is based on dynamical system representation of turbulent flows. The attractor of the system is sought and approximated by leveraging the properties of the governing equations. The dynamics of the system have been tracked on this lower-dimensional attractor using the inertial manifold theory.

2.2 Combustion modeling

The primary modeling frameworks in the literature have been developed for turbulent flows, and then extended and modified for combustion systems. Among such methods, large eddy simulation is the most implemented one because of its ability in modeling turbulent physical processes relevant to combustion applications [7, 108, 109]. In LES, the large energy-containing scales are resolved directly, while the small-scales contributions are modeled. Combustion is controlled by molecular diffusion of reactants at scales competing with the smallest scales of turbulence and needs to be exclusively modeled in all LES formulations. While this may seem to contradict the premise of LES, combustion in canonical [110–114] and practical [115–118] applications have been successfully modeled. In general, LES is far more accurate compared to the Reynolds-averaged Navier-Stokes equations when the large-scale mixing controls the combustion process, for instance in flames far away from extinction [108].

Combustion modeling in practical devices faces two key challenges: 1) combustion is controlled by molecular diffusion of reactants at scales competing with the smallest scales of turbulence, and 2) the chemistry mechanism of practical hydrocarbon fuels may involve thousands of species [26]. This makes direct simulations infeasible even with foreseeable advancements in computing power. Combustion models address these challenges by including a statistical representation of small scales and developing reduced chemistry mechanisms containing much fewer species. These issues are generally addressed independently, introducing another modeling need to couple them, namely the combustion model.

2.2.1 Reduced chemistry mechanisms

Chemical mechanisms of practical fuels contain few hundreds and sometimes thousands of species [27]. It is essential to develop surrogate chemical mechanisms containing a far fewer number of species. For simple hydrocarbon fuels, reduced mechanisms with tens of species can represent a range of chemistry pathways accurately [119, 120]. In general, reduced mechanisms are developed assuming that the entire chemical composition can be represented by a lower-dimensional manifold spanned by a small number of species. Such manifolds have been developed with different assumptions [121], for example, reaction manifolds are developed by assuming species conservation is controlled only by chemical reaction. Reaction manifolds are built by decomposition of species into manifold (resolved) species and unresolved species based on chemical reaction rates and their properties. Intrinsic low-dimensional manifolds (ILDM) [122], quasi-steady state manifolds [123, 124] and manifolds determined by computational singular perturbation [125] are all reaction manifolds.

Reaction-diffusion manifolds account for both chemical reaction and molecular diffusion in species gradient. Since turbulent straining can intensify scalars gradient and molecular diffusive fluxes, these manifolds are more relevant to turbulent flames. The

most prevalent reaction-diffusion manifolds are flamelet manifolds [126, 127], flamelet generated manifolds [128] and flame prolongation of ILDM [129]. A combustion model defines coupling between reaction and diffusion, which is determined based on specific flame structure and combustion mode i.e. premixed or non-premixed combustion regime.

2.2.2 Flamelet approaches

In turbulence modeling, the small unresolved scales are assumed to be in equilibrium and respond instantaneously to the large scales. This assumption manifests in several ways, and when combined with the universality of the statistics of small scales, leads to known models for sub-filter scales such as the Smagorinsky closure [63] or the algebraic model for variance [126, 130]. Even when this equilibrium assumption is relaxed, it is selectively eased to add more nonequilibrium physics. For instance, in the transported kinetic energy model [131], the dissipation rate spectrum reaches a statistically stationary state, but it is based on non-local effects. Similar modifications can be made for scalar energy as well [114, 132].

While the above discussion deals with the modeling of turbulence or non-reactive scalars, a similar local equilibrium assumption is used in the construction of combustion models [133, 134]. The primary success of LES is due to the accuracy of this assumption for reactive scalars, which has enabled the development of a variety of combustion models [126, 135–138]. Of these the most commonly used technique is the flamelet or flame-generated manifold approach. The general formulation of a flamelet model can be described as a mapping

$$\phi = \mathcal{G}(\xi), \tag{2.18}$$

where $\phi \in \mathbb{R}^{N_s}$ is the local thermochemical composition vector, and $\xi \in \mathbb{R}^{N_M}$ is

a nominal set of mapping variables for the combustion model $\mathcal{G}$, with $M < N_s$. In general, $\mathcal{G}$ is obtained through another modeling assumption: a single or set of canonical flames are sufficient to represent the range of thermochemical composition space accessed by the target configuration of interest. It is assumed that reaction occurs in thin flamelets, at scales smaller than resolved turbulent scales; and the reaction zone is steady and laminar similar to canonical one-dimensional flames. The equilibrium assumption implies that the flame reaches an equilibrium structure as the large-scale eddies evolve in time. Similar to the sub-filter scale models for turbulence, nonequilibrium flame-structure models can be developed that invoke the equilibrium notion in different ways. For instance, in the unsteady flamelet formulation, it is assumed that the flame responds to strain rate variations with a lag, but still conforms to the diffusion or any other canonical flame structure [127, 139].

Depending on the choice of canonical flames, such as counterflow or burner-stabilized laminar flames, the composition state can be accessed by a set of parameters including a nonreactive scalar such as mixture fraction in non-premixed flames. In LES of turbulent flames, the composition manifold is pre-computed and pre-tabulated, and only the filtered manifold parameters are solved during the simulation. Tabulation techniques are then used to find the local composition state. Pre-generation of combustion manifolds, such as flame-generated manifold [128], flamelet-progress variable [126], or unsteady flamelets [127] reduces the computational cost while providing excellent predictive capabilities for stable flames far from extinction [7].

In practical systems, the development of such manifold methods faces some inherent hurdles. The primary issue is that manifolds are pre-generated by using an auxiliary system. It has been shown that the choice of the auxiliary system has a direct impact on the results [11, 140–143]. Essentially, it is assumed that the flame structure is similar to that of the auxiliary system, which is difficult to ensure in complex flows. This assumption has been the focus of research in flamelet approaches,

involving multiple strategies to address the extrapolation of canonical flame structure to practical calculations [144–146].

A second issue concerns the necessary models once a manifold is selected. LES provides only the filtered mapping variables, and the small-scales effect should be modeled. In flamelet approaches, the subfilter closure is obtained as

$$\widetilde{\phi} = \int \mathcal{G}(\xi) P(\xi) \mathrm{d}\xi, \tag{2.19}$$

where $\widetilde{\phi}$ is the set of filtered mapping variables, and P is the sub-filter joint probability density function (PDF) of the input variables. Determination of both P and $\mathcal{G}$ closes the combustion modeling. The small-scale closure is achieved either by assuming a functional form for the subfilter joint PDF or by solving transport equations of P. In either case, closures for sub-filter variance of manifold parameters [114, 130], as well as the one-point one-time distribution functions [147, 148] are needed. These models can also impact simulation predictions, especially when local extinction and reignition become important [132, 149].

2.2.3 Transported PDF approaches

Transported PDF approaches reduce combustion modeling into determining only P by considering a unity mapping in Eq. 2.18, $\phi = \xi$. Without any assumption of a low-dimensional manifold in the composition space, detailed chemistry, or a reduced chemistry mechanism, is solved during LES or RANS computations. Therefore, PDF methods are general for any combustion regime, and they are more successful when flame structure deviates from normal behavior such as in events of extinction and reignition. However, they increase the computational cost of the simulation, as modeled conservation equations of joint-PDF of fluid properties and thermochemical composition should be solved. Contrary to flamelet approaches, there is no limiting

assumption about flame structure, and reaction computations are not pre-processed. While PDF methods are generally more expensive, considering non-equilibrium effects in flamelet approaches requires higher-dimensional manifolds, which increases tabulation cost and requires *a priori* knowledge about the flame structure.

The major advantage of PDF methods is that reaction rates are treated directly, and only molecular diffusion needs to be modeled by mixing models. In general, mixing models are developed based on the equilibrium between dissipation and the production of kinetic energy. Mixing models developed for inert mixing have been used for reactants mixing in PDF methods. However, studies have shown that chemical reactions can steepen species gradients and enhance molecular mixing, and more advanced models are required.

Other closures such as the linear eddy model [150], conditional moment closure [151] and multiple mapping conditioning can be cast in a similar framework. Alternative approaches, such as the filtered density function (FDF) method [152, 153], face related issues in terms of the modeling of small-scale mixing. The overall conclusion is that such equilibrium assumptions are often made in an ad-hoc manner via Kolmogorov's theory of turbulence extended to turbulent flames, even though turbulence theory is valid only in the incompressible constant density cases. A few direct numerical simulations have shown that such assumptions might be erroneous [29, 30].

In this regard, similar to turbulence modeling in LES, different approaches have been considered for modeling turbulent flames. The deconvolution-based modeling procedure [154–156] assumes that given the large scale field, the unresolved scales can be reconstructed, albeit only to some accuracy, to directly obtain sub-filter models. In particular, such methods have been linked to an explicit filtering procedure, where different filter shapes are explicitly assumed and the unresolved fields are recovered using an inversion procedure [157]. While deconvolution methods have been relatively

successful in turbulent flows, chemical reaction rates are very sensitive to the shape of filter and approximations of its inverse [158]. Other approaches such as the variational multiscale method [159, 160] invoke the equilibrium assumption in some form.

2.3 Summary

In this chapter, various approaches in modeling reacting flows have been reviewed with a focus on scale resolving approaches. The discussion depicts the state of the art in turbulence and turbulent combustion modeling, limitations of current approaches, and what needs to be addressed towards an adaptive modeling approach. In general, the majority of computational analyses of reacting flows have been limited to the design process focusing on specific concerns such as efficiency, emission reduction, and strength of materials. An outcome of this focus is that current frameworks are geared towards predicting statistically stationary flows, essentially systems operating at specific design conditions. To analyze and predict system dynamics when deviating from normal behavior, the development of models which can track distinct trajectories of reacting flows is essential. Since these systems are dominated by turbulence, small perturbations can potentially cause large changes in behavior, including catastrophic failure. Hence, developing models that circumvent statistical representations of small scales is crucial to ensure the predictive accuracy of the models.

CHAPTER III

Approximate Inertial Manifold Approach

Any fluid system described by a set of partial differential equations can be formulated as a finite-dimensional dynamical system after appropriate spatial discretization. Treatment of reacting flows as dynamical systems opens new paths for modeling and development of reduced-order descriptions of such systems. Starting from the mid-1980s, there has been growing recognition that treating an appropriately spatially-discretized set of governing equations as a finite-dimensional dynamical system provides access to properties about events that are otherwise difficult to assess using statistical tools. This approach to modeling complex systems has been particularly successful in weather prediction [36].

From a theoretical perspective, the focus has been on the structure of the dynamical system in phase space, which is composed of the N-dimensional state space defined by the degrees of freedom describing the discretized system. For instance, if a fluid domain is discretized using n_g grid points, and at each point n_v variables are solved, the state space dimension is $N = n_g \times n_v$. Note that this estimation is dependent on the type of numerical scheme used [37]. The spatial and temporal evolution of the turbulent flow can then be expressed as a trajectory in this state space. In many systems dominated by coherent structures, the long-time behavior of the system is dictated by dynamics confined to a low-dimensional subspace of the full N-dimensional state space. All

trajectories of the system are attracted to this closed subset of the phase space, known as the attractor. Schematic visualization of an attractor is presented in Fig. 3.1 with multiple trajectories of the system.

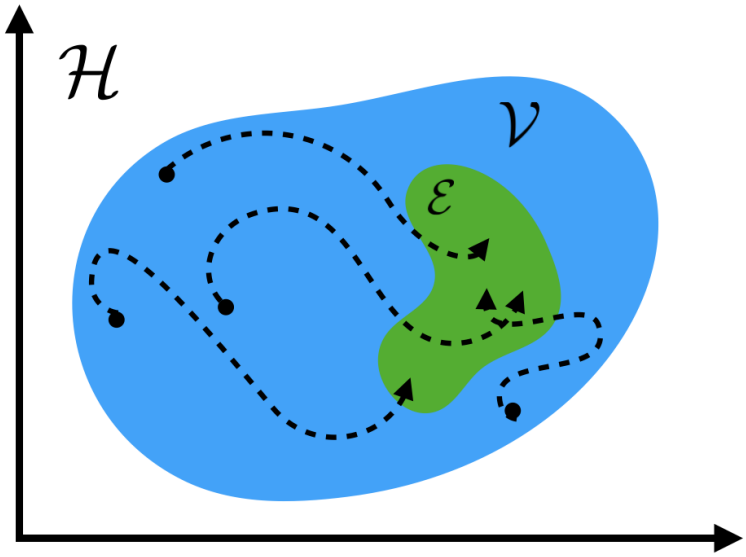

Figure 3.1: Schematic of the phase space representation of a dynamical system. The plane represents the Hermitian space dynamics reside in. The blue subset is the state-space, $\mathcal{V}$. Initial conditions are represented by black dot. Trajectories are shown as dashed black lines. The green subspace is the attractor, $\mathcal{E}$.

Constantin et al. [97] showed that the dimension of the attractor scales nonlinearly with the Reynolds number of the flow. However, direct estimations of this attractor dimension for turbulent flows using the Kaplan-Yorke conjecture [99] showed that attractor dimensions are orders of magnitude lower than the number of degrees of freedom required by DNS [34, 38, 100].

In this regard, one of the original premises for the use of dynamical systems is the development of reduced-order models, but this approach has been fraught with challenges for the following reasons [101]. First, the possible high-dimensionality of the attractor led to the conclusion that a highly reduced model cannot be easily determined [102]. Second, phenomenological approaches such as the intermittency

model [103] did not directly provide a path to other spatially extended systems. Finally, there have been fundamental theoretical issues as to whether such reduced models can capture the chaoticity of the flow [101]. In light of these challenges, the recent focus on data-driven sciences has renewed interest in dynamical systems-based modeling of turbulent flows [104–106]. For instance, techniques for describing turbulent boundary layers have been formulated from these reduced-order modeling concepts [107].

The inertial manifold theory provides a path to locate the attractor in specific dynamical systems. In dissipative infinite-dimensional dynamical systems described by partial differential equations, the long-time behavior of trajectories can be studied in an invariant finite-dimensional subset of phase space called the Inertial manifold (IM) [98]. These manifolds, when they exist, attract all trajectories of the system exponentially and therefore contain the global attractor. The dynamics of the inertial manifold can be described by a finite-dimensional system of ordinary differential equation (ODE), called the inertial form, which completely describes the long-time dynamical behavior of the original infinite-dimensional system.

3.1 The inertial manifold theory

Consider a set of partial differential equations that describe the evolution of any fluid system. The variables of interest are given by the set $\boldsymbol{\xi} = \{\xi_1, \xi_2, \cdots, \xi_{n_v}\}$, and the equations are written as

$$\frac{\partial \boldsymbol{\xi}}{\partial t} + \nabla \cdot \mathcal{N}(\boldsymbol{\xi}) + \nabla \cdot \mathcal{L}\boldsymbol{\xi} + S(\boldsymbol{\xi}) = 0, \tag{3.1}$$

where $\mathcal{N}$ is a nonlinear operator, $\mathcal{L}$ is a linear operator, and S is a volumetric source term. In the context of reacting flows, $\boldsymbol{\xi}$ will include all transported variables such as momentum, energy, and reacting scalars. The nonlinear term creates a spectrum of length scales, which introduces the inherent computational complexity in solving these

equations. For reacting scalars, including species mass fractions and temperature, the volumetric chemical source term involves contributions from many fast reactions, which introduces an additional source of nonlinearity. Since the range of scales is dependent on some intrinsic parameter (such as Reynolds number), these equations are computationally intractable for any practical flow and require some form of modeling that reduces the range of scales.

The reacting flow can be cast in a dynamical system framework after proper spatial discretization of Eq. 3.1, $\mathcal{D} : \boldsymbol{\xi} \rightarrow \boldsymbol{v}$, with $\mathcal{D}$ being the discretization operation. In this discretized form, the governing equations can be written as

$$\frac{d\boldsymbol{v}}{dt} + \mathcal{A}\boldsymbol{v} + \mathcal{R}(\boldsymbol{v}) = 0, \ \boldsymbol{v}(t=0) = \boldsymbol{v}_0, \tag{3.2}$$

where $\boldsymbol{v}$ is the discrete set of variables, $\mathcal{A}$ is the discretized linear term, and $\mathcal{R}$ is the discretized nonlinear term including the chemical source term. To apply the inertial manifold theory, $\mathcal{A}$ is taken to be an unbounded, linear, self-adjoint operator defined on the Hilbert space $\mathcal{H}$, where dynamics of the system reside in; hence $\mathcal{A}^{-1}$ is compact.

3.1.1 The squeezing property

Let $\boldsymbol{S}(t) : \boldsymbol{v}(0) \rightarrow \boldsymbol{v}(t)$ be the semigroup of operators defining the solutions of Eq. 3.2; and $\boldsymbol{S}(t)u_0$, and $\boldsymbol{S}(t)v_0$, be two solutions of Eq. 3.2, where $u_0, v_0 \in \mathcal{H}$. The squeezing property states that for every $r > 0$, there is a k depending on r and the linear operator such that if $|\mathcal{A}u_0| \leq r$ and $|\mathcal{A}v_0| \leq r$, then

$$|\boldsymbol{S}(t)u_0 - \boldsymbol{S}(t)v_0| \leq \exp(kt)|u_0 - v_0|, \text{ for all } t \geq 0. \tag{3.3}$$

The squeezing property of Eq. 3.2 was proved by Foias and Temam [161] and Constantin et al. [162]; this property is independent of the existence of an inertial manifold.

3.1.2 Definition of an inertial manifold

A subset $\mathcal{M} \subseteq \mathcal{H}$ is an inertial manifold if it satisfies the following properties [98]:

1. $\mathcal{M}$ is a finite dimensional Lipschitz manifold,

2. $\mathcal{M}$ is invariant, i.e., $\boldsymbol{S}(t)\mathcal{M} \subseteq \mathcal{M}$, for all $t \geq 0$,

3. $\mathcal{M}$ attracts exponentially all solutions of Eq. 3.2, i.e.,

$$\lim_{t\to\infty} \text{dist } (\boldsymbol{S}(t)\boldsymbol{v}_0, \mathcal{M}) = 0, \tag{3.4}$$

   for every $\boldsymbol{v}_0 \in \mathcal{H}$.

The third property implies that an inertial manifold must contain the universal attractor of the dynamical system. The proof of this property relies on the squeezing property of the semigroup $\boldsymbol{S}(t)$.

Since $\mathcal{A}^{-1}$ is compact and self-adjoint, the set of eigenvectors of $\mathcal{A}$ forms an orthonormal eigenbasis for the Hilbert space $\mathcal{H}$; and eigenvalues of $\mathcal{A}$ satisfy,

$$0 < \lambda_1 \leq \lambda_2 \leq \ldots, \lambda_j \to \infty \text{ as } j \to \infty. \tag{3.5}$$

The main requirement for the existence of an inertial manifold is the existence of a relatively large gap in the spectrum of the linear operator. If there is a $m > 1$ such that a sufficiently large gap between λ_m and λ_{m+1} exists, an inertial manifold with dimension m can be constructed spanned by the first m eigenvectors of the linear operator.

An orthogonal projection operator P can be defined onto a subset of the Hilbert space spanned by the first m eigenvectors of $\mathcal{A}$. An inertial manifold can be constructed as a graph of a Lipschitz function,

$$\Phi : \boldsymbol{P}\mathcal{H} \to \boldsymbol{Q}\mathcal{H} \tag{3.6}$$

where $\boldsymbol{Q} = \mathcal{I} - \boldsymbol{P}$ is the complement projection of $\boldsymbol{P}$. With this definition of the orthogonal projection and the complement projection, the squeezing property (Eq. 3.3) can be stated as [98, 163],

$$\begin{aligned} |\boldsymbol{Q}(\boldsymbol{S}(t)u_0 - \boldsymbol{S}(t)v_0)| &\leq \gamma |\boldsymbol{P}(\boldsymbol{S}(t)u_0 - \boldsymbol{S}(t)v_0)| \\ |\boldsymbol{S}(t)u_0 - \boldsymbol{S}(t)v_0)| &\leq k_2 \exp(-k_3 \lambda_{m+1} t)|u_0 - v_0| \end{aligned} \tag{3.7}$$

where $\gamma > 0$, k_2 and k_3 are constants. Inertial manifold is a subset of the state space spanned by the first m eigenfunctions of $\mathcal{A}$, such that the largest eigenvalue of the eigenbasis spanning inertial manifold ($\mathcal{A}|_{P\mathcal{H}}$) is λ_m, and the smallest eigenvalue corresponding to the eigenbasis of the orthogonal space ($\mathcal{A}|_{Q\mathcal{H}}$) is λ_{m+1} [98, 164]. Hence, the inertial manifold is m-dimensional. The squeezing property (Eq. 3.7) implies that the difference between two trajectories of the system reduces exponentially, and the exponential rate is proportional to the eigenvalue of the slowest eigenmode of the complement space. When an IM exists, it contains the attractor of the system. Figure 3.2 provides a schematic representation of the IM in the state space.

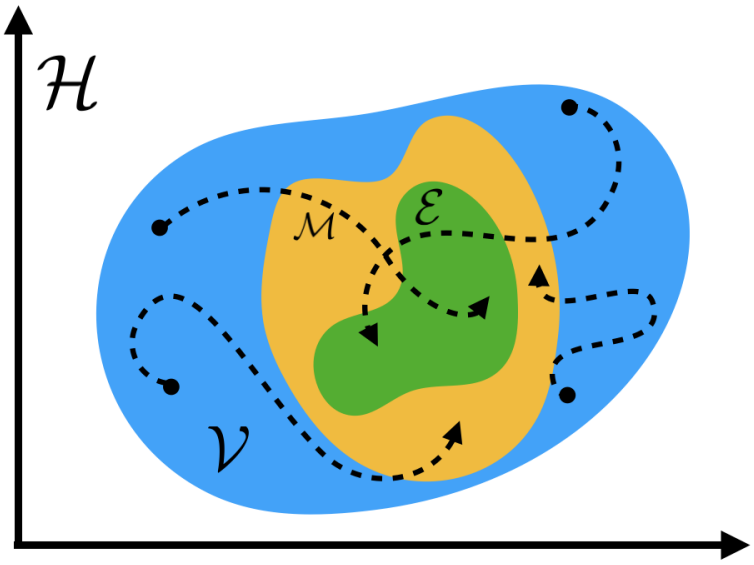

Figure 3.2: Schematic of the inertial manifold of a dynamical system. The plane represents the Hermitian space dynamics reside in. The blue subset is the phase space, $\mathcal{V}$. The initial conditions are represented by black dot. The trajectories are shown as dashed black lines. The green subspace is the attractor $\mathcal{E}$, and the inertial manifold is the yellow subspace, $\mathcal{M}$.

3.1.3 Construction of an inertial manifold

To construct the inertial form which describes the dynamics of the system on the inertial manifold, the orthogonal projection operator $\boldsymbol{P}$ is applied to the phase-space to split it into the manifold variables ($\boldsymbol{u}$) and the orthogonal subset ($\boldsymbol{w}$),

$$\boldsymbol{u} = \boldsymbol{P}\boldsymbol{v},\ \boldsymbol{w} = (\mathcal{I} - \boldsymbol{P})\boldsymbol{v} = \boldsymbol{Q}\boldsymbol{v},\ \boldsymbol{v} = (\boldsymbol{u}, \boldsymbol{w}). \tag{3.8}$$

The complement projection $\boldsymbol{Q}$ maps its operand to the null-space of the projection operator $\boldsymbol{P}$. Formally, IMs are realized as graphs of functions $\Phi : \boldsymbol{P}\mathcal{H} \rightarrow \boldsymbol{Q}\mathcal{H}$. For the form of the discretized system considered here (Eq. 3.2), the goal is to describe the dynamics in terms of $\boldsymbol{u}$ alone. The state space of the original dynamical system is N-dimensional with $\boldsymbol{v} \in \mathbb{R}^{n_g \times n_v}$, the inertial form is $m \times n_v$ dimensional with

$m << n_g$.

Such a decomposition of the state space can be achieved by any set of orthogonal eigenbases of the full-dimensional state space. The dissipative linear operator, with a set of positive ascending eigenvalues, provides a clear path for decomposition into the resolved and unresolved subspaces. However, finding the eigenvalues of all of the linear and nonlinear terms of the governing equation can give more information about dominant dynamics. This method is more expensive computationally since the Jacobian of the dynamical system needs to be computed at each time step. Several reduced-order mechanisms are developed based on such decomposition, such as intrinsic low dimensional manifolds [122] and the computational singular perturbation [165, 166].

The goal is to describe the dynamical features of the flow in this lower-dimensional manifold instead of the full-dimensional system. By applying the projection operator to the discrete governing equations (Eq. 3.2), the evolution equations for the resolved and unresolved fields can be obtained as

$$\frac{d\boldsymbol{u}}{dt} + \mathcal{A}\boldsymbol{u} + \boldsymbol{P}\mathcal{R}(\boldsymbol{v}) = 0,\ \boldsymbol{u}(t=0) = \boldsymbol{P}\boldsymbol{v}_0, \tag{3.9}$$

and

$$\frac{d\boldsymbol{w}}{dt} + \mathcal{A}\boldsymbol{w} + \boldsymbol{Q}\mathcal{R}(\boldsymbol{v}) = 0,\ \boldsymbol{w}(t=0) = \boldsymbol{Q}\boldsymbol{v}_0, \tag{3.10}$$

where $\boldsymbol{v}_0$ is the initial condition associated with the full state-space representation. In Eqs. 3.9 and 3.10, the fact that orthogonal projections commute with the linear operator is used,

$$\begin{aligned} \boldsymbol{P}\mathcal{A} = \mathcal{A}\boldsymbol{P},\ &\rightarrow \boldsymbol{P}\mathcal{A}\boldsymbol{v} = \mathcal{A}\boldsymbol{u} \\ \boldsymbol{Q}\mathcal{A} = \mathcal{A}\boldsymbol{Q},\ &\rightarrow \boldsymbol{Q}\mathcal{A}\boldsymbol{v} = \mathcal{A}\boldsymbol{w}. \end{aligned} \tag{3.11}$$

As $\boldsymbol{P}$ and $\boldsymbol{Q}$ are orthogonal projections in the Hilbert space $\mathcal{H}$, they commute with the linear operator $\mathcal{A}$, and its powers [33].

The main challenge in closing the inertial form is in the projected nonlinear term $\boldsymbol{P}\mathcal{R}(\boldsymbol{v})$, which cannot be described using only $\boldsymbol{u}$. By constructing the inertial manifold graph: $\boldsymbol{w}(t) = \Phi(\boldsymbol{u}(t))$, the inertial form is closed. Now $\boldsymbol{v}(t) = \big(\boldsymbol{u}(t), \Phi(\boldsymbol{u}(t))\big)$ is a solution of Eq. 3.2 if and only if $\boldsymbol{u}(t)$ and $\boldsymbol{w}(t) = \Phi(\boldsymbol{u}(t))$ satisfy Eqs. 3.9 and 3.10.

3.1.4 Uniqueness of the inertial manifold graph

Given a continuous bounded function $\sigma : \mathbb{R} \to \mathcal{H}$, there is a bounded unique solution for equation

$$\frac{d\psi}{dt} + \mathcal{A}\psi = \sigma, \tag{3.12}$$

as $t \to -\infty$. Integrating Eq. 3.12 between s and t for $s < t$ gives,

$$\psi(t) = e^{-(t-s)\mathcal{A}}\psi(s) + \int_s^t e^{-(t-\tau)\mathcal{A}}\sigma(\tau)\mathrm{d}\tau. \tag{3.13}$$

Using the boundedness assumption, for $s \to -\infty$,

$$\psi(t) = \int_{-\infty}^t e^{-(t-\tau)\mathcal{A}}\sigma(\tau)\mathrm{d}\tau, \tag{3.14}$$

which shows the uniqueness of ψ. In Eqs. 3.12-3.14, ψ and σ can be replaced by $\boldsymbol{w}$ and $-\boldsymbol{Q}\mathcal{R}(\boldsymbol{v})$, respectively, with $\boldsymbol{v} = \Big(\boldsymbol{u}, \Phi(\boldsymbol{u})\Big)$. Then $\boldsymbol{w}(t)$ is given by,

$$\boldsymbol{w}(t) = \int_{-\infty}^t e^{-(t-\tau)\mathcal{A}}\boldsymbol{Q}\mathcal{R}(\boldsymbol{u} \oplus \Phi(\boldsymbol{u}), \tau)\mathrm{d}\tau, \tag{3.15}$$

for all $t \in \mathbb{R}$. In particular, $\boldsymbol{w}(0)$ is given by

$$\boldsymbol{w}(0) = \int_{-\infty}^0 e^{\tau\mathcal{A}}\boldsymbol{Q}\mathcal{R}(\boldsymbol{u} \oplus \Phi(\boldsymbol{u}), \tau)\mathrm{d}\tau. \tag{3.16}$$

Note that $\boldsymbol{w}(0)$ depends on Φ, and with $\boldsymbol{u}(0) \in \boldsymbol{P}\mathcal{H}$, a formal mapping for the manifold is built. Equation 3.15 is identical to the Mori-Zwanzig formulation for reduced-order modeling of dynamical systems [167, 168]. The original dynamical system is cast into a lower-dimensional subset. However, the integral known as the memory term needs to be computed by solving the orthogonal dynamical system. Reduced-order models of turbulent systems have been developed following the Mori-Zwanzig formalism and approximating the orthogonal dynamical system solution [169–171].

In the past, numerous studies have demonstrated the properties of inertial manifolds for specific systems [98, 172, 173]. These include analysis of the stability of the manifolds to perturbations [98], the exponential convergence of trajectories to the manifold [172], and questions regarding the suitability of this manifold approximation for representing the evolution of a dynamical system [172, 174]. These studies demonstrated that an IM is a reliable framework for describing the long-time dynamics of the system, and it can be a powerful approach for developing reduced-order models that describe the underlying dynamical system. An example is the class of Galerkin-based IMs, also known as Galerkin manifolds [39, 174].

Current proofs on the existence of an IM rely on the presence of arbitrarily large gaps in the spectrum of the linear operator of the dynamical system [98]. The existence of an inertial manifold has been proven for many dissipative PDEs [98, 175], describing different physical systems such as reaction-diffusion systems [176–179], hydrodynamic instabilities [180, 181] and interfacial instabilities [98, 176, 182, 183]. However, it is important to recognize that these theoretical foundations are based on strong restrictions [98, 175], and a rigorous extension to real-life problems, such as an end application in multi-physics engineering processes, is a work in progress. Whether the spectral gap condition is necessary for the existence of an IM is still being explored. As such, it might be possible to prove the existence of the inertial manifold with weaker conditions [98].

3.2 Approximate inertial manifolds

Current theories on the existence of an inertial manifold strictly require a spectral gap, delineating time scales associated with the modes on the orthogonal space from those of the inertial manifold. However, not all of the properties of an IM, for instance, the squeezing property, require the spectral gap condition to be satisfied. It might be possible to develop a theory of inertial manifolds that uses weaker conditions [98, 179]. Furthermore, these theoretical results cannot provide an explicit form for the inertial manifold. As a result, an approximation of the inertial manifold is necessary, which leads to the formulation of an approximate inertial manifold (AIM). AIMs can be developed to approximate either the true inertial manifold [172, 177, 184] or a neighborhood of the global attractor of the system [33, 185–187]. In this latter case, while the existence of an IM is unknown, AIM still describes a subset of the phase space which approximates a neighborhood of the global attractor [174]. Figure 3.3 shows a sketch of an AIM in the phase space. While the inertial manifold is shown here, there is no need for an IM to exist; and AIM can enclose a neighborhood of the attractor.

In this vein, one approach considered in this work is the direct approximation of the inertial manifold [39, 174, 187, 188], where the dynamics of the system can be simplified in a subspace of the state space, naturally leading to the construction of a reduced-order model. Here, the dynamics of the system are tracked on an AIM. The main assumption is that the dynamics in the complement space of the IM and full state-space are enslaved by the dynamics on the IM. In other words, the motion in the complement space responds instantaneously to changes in the trajectory on the AIM. While this assumption is justified by the theoretical studies discussed above [33, 98, 172], their validity needs to be scrutinized more rigorously. Many studies have been conducted on approximate inertial manifolds for dissipative systems, estimating their dimension and the rate of exponential convergence of dynamics to the AIM

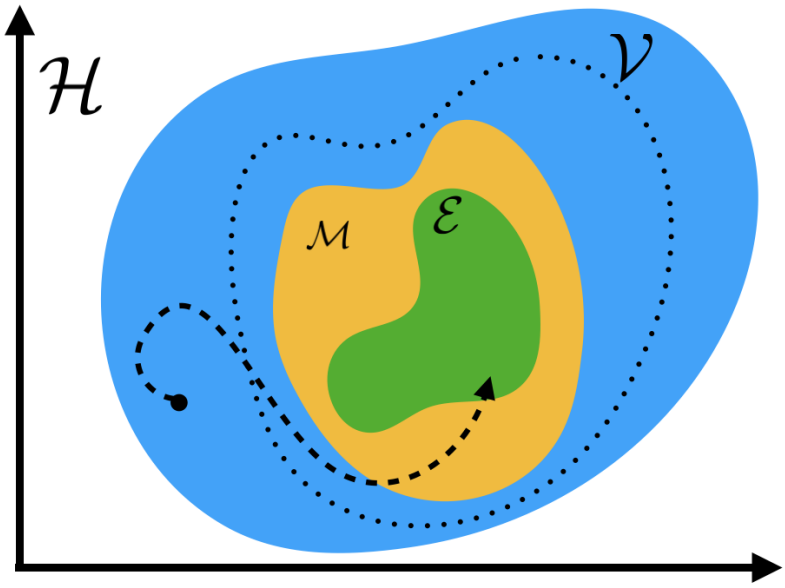

Figure 3.3: Schematic of the approximate inertial manifold of a dynamical system. The plane represents the Hermitian space, and the blue subset is the phase space, $\mathcal{V}$. A trajectory is shown as a dashed black line. The green subspace is the attractor $\mathcal{E}$, and the inertial manifold is the yellow subspace, $\mathcal{M}$. The AIM is enclosed by the dotted line.

merely for dimension reduction [174, 189].

The concept of ROMs based on inertial manifolds for turbulence modeling was first introduced by Temam [33], where the interaction law between small and large scales guarantees the existence of an inertial manifold of the system. This work was followed by AIM-inspired ROM algorithms developed for different systems, including reaction-diffusion systems [98, 190], the Kuramoto-Sivashinsky equation (KSE) [172, 174, 183] and the two-dimensional Navier-Stokes equations [33, 39, 191, 192]. In a more recent work, an AIM was developed as a suitable solution of the three-dimensional Navier-Stokes equations in Fourier space, and its properties were analyzed [193]. While almost all of these studies treat the governing equations using a Fourier-based spectral discretization, finite difference and finite volume-based PDE discretizations have also been considered [194, 195].

Recently, data-driven approximate inertial manifolds have been constructed using machine learning and data assimilation techniques [196–199]. These techniques can be used to either determine the structure of the AIM model (including its dimension) or to track the dynamics with prior knowledge about its structure. Furthermore, AIMs enable the study of qualitatively different dynamical behaviors such as the transition to turbulence. For instance, bifurcations of the Kuramoto-Sivashinsky equation have been studied over a range of parameters using an AIM projected in two dimensions by symmetry reduction techniques [200]. Here, the manifold was computed and visualized for different dynamical behaviors of the system, which is intractable in the full state space. Despite these extensive studies, there is limited computational exploration of AIMs and, in particular, their suitability for modeling turbulent reacting flows. The focus of this work is to address this gap by systematically studying the AIM approach for a set of canonical reacting flows.

3.2.1 Mathematical formulation of an AIM

The objective is to develop a reduced-order model predicting the dynamical behavior of the system in a low-dimensional manifold described by dynamics of a subset of the variables of interest. Unlike the predominant approach in turbulence modeling which uses a spatial filtering operator for separation of variables, here the governing equations are leveraged to define an orthogonal projection operator $\boldsymbol{P}$ which decomposes the vector of variables ($\boldsymbol{v}$) into the resolved $\boldsymbol{u}$ and the unresolved $\boldsymbol{w}$ subsets. The projection $\boldsymbol{P}$ is performed on the space spanned by the first m eigenfunctions of the linear operator $\mathcal{A}$. The choice of m depends on the spectral properties of the linear operator [33, 201]. By applying the projection operator to Eq. 3.2, the governing equations for the resolved and unresolved variables are obtained in Eqs. 3.9- 3.10.

The full - discrete - set of variables $\boldsymbol{v}$ has dimension $N = (n_g \times n_v)$. The projection operators

a) $\boldsymbol{P}$ has dimension $(m \times n_v, n_g)$, and

b) $\boldsymbol{Q}$ has dimension $(n_g - m \times n_v, n_g)$.

Therefore,

a) $\boldsymbol{u} = \boldsymbol{P}\boldsymbol{v} \in \mathbb{R}^{m \times n_v}$,

b) $\boldsymbol{w} = \boldsymbol{Q}\boldsymbol{v} \in \mathbb{R}^{n_g - m \times n_v}$.

Dimensions of $\boldsymbol{u}$ and $\boldsymbol{w}$ sum to N to avoid Eqs.3.9- 3.10 give rise to an overdetermined set of equations. Therefore, there exist matrices $\boldsymbol{P}^*$ and $\boldsymbol{Q}^*$ such that,

$$\begin{aligned} \boldsymbol{v} &= \boldsymbol{P}^*\boldsymbol{u} + \boldsymbol{Q}^*\boldsymbol{w} \\ \mathcal{I} &= \boldsymbol{P}^*\boldsymbol{P} + \boldsymbol{Q}^*\boldsymbol{Q}. \end{aligned} \tag{3.17}$$

For tracking the dynamics of the approximate inertial manifold by only the resolved variables, the projected nonlinear term $\boldsymbol{P}\mathcal{R}(\boldsymbol{v})$ should be modeled as it cannot be described using only $\boldsymbol{u}$. The goal is to reconstruct $\boldsymbol{w}$ given only information of $\boldsymbol{u}$ and compute the nonlinear terms with the recovered full-dimensional vector of variables. Using IM theories, it is assumed that the dynamics of $\boldsymbol{w}$ respond instantaneously to the dynamics of $\boldsymbol{u}$. With the approximation $\mathrm{d}\boldsymbol{w}/\mathrm{d}t = 0$ [185], Eq. 3.10,

$$\frac{d\boldsymbol{w}}{dt} + \mathcal{A}\boldsymbol{w} + \boldsymbol{Q}\mathcal{R}(\boldsymbol{v}) = 0, \tag{3.18}$$

results in

$$\mathcal{A}\boldsymbol{w} + \boldsymbol{Q}\mathcal{R}(\boldsymbol{v}) = 0. \tag{3.19}$$

The above nonlinear equation can be iterated starting from an initial guess to obtain a converged solution for $\boldsymbol{w}$,

$$\boldsymbol{w}^* = -\mathcal{A}^{-1}\boldsymbol{Q}\mathcal{R}(\boldsymbol{u}, \boldsymbol{w}). \tag{3.20}$$

With this approximation of the unresolved dynamics, the nonlinear term $\boldsymbol{P}\mathcal{R}(\boldsymbol{u},\boldsymbol{w})$, and hence the governing equations of the resolved modes $\boldsymbol{u}$, are closed,

$$\frac{d\boldsymbol{u}}{dt} + \mathcal{A}\boldsymbol{u} + \boldsymbol{P}\mathcal{R}(\boldsymbol{u},\boldsymbol{w}^*) = 0,\ \boldsymbol{u}(t=0) = \boldsymbol{P}\boldsymbol{v}_0. \tag{3.21}$$

The concept of the inertial manifold is introduced for dissipative dynamical systems with a linear positive unbounded operator, whose eigenvectors provide an orthonormal basis for the Hilbert space the dynamics reside in. Current theories on the existence of an IM require a sufficiently large spectral gap in the eigenvalues of the linear operator, which provides a natural way for the orthogonal decomposition of the state space. Therefore, considering the eigenvalues of the linear operator for projection is a computationally efficient choice for this problem. However, finding the eigenvalues of the full right-hand side of the equation can give more information about dominant dynamics. The computational cost of evaluating the eigenvalues of the full right-hand side can be prohibitive in higher-dimensional systems, but lower-dimensional approximate inertial manifolds can be tracked [165, 166].

In the following chapters, this approximation of the inertial manifold has been investigated for turbulent flows and turbulent combustion. In all systems considered, the proposed AIM is analyzed both *a priori* and *a posteriori*. In the *a priori* analysis, first the full-dimensional system of equations is solved using direct methods. Then, the solution is decomposed into the resolved and unresolved variables by projections $\boldsymbol{P}$ and $\boldsymbol{Q}$, respectively. The unresolved variables are approximated by the exactly resolved scales using Eq. 3.20 and are compared against the exact unresolved modes. This analysis provides an insight into whether approximation $\mathrm{d}\boldsymbol{w}/\mathrm{d}t = 0$ is justified. In the *a posteriori* analysis, the proposed closure for the resolved variables is used to forecast the dynamics of the system in a low-dimensional approximate IM rather than the full-dimensional system. The modeled system is then compared against the

exact resolved solution obtained from direct methods.

3.3 Summary

First, reacting turbulent flows are cast as a dynamical system, and properties of governing equations are discussed. Second, the inertial manifold theory is introduced, which provides a path for developing reduced-order models. A ROM is proposed based on the IM theory, which decomposes the dynamics of the system into resolved and unresolved scales similar to conventional modeling approaches discussed in Chap. II. However, in this approach, the governing equations of the system are leveraged for the decomposition of scales and closure of the model.

CHAPTER IV

AIM-Based Turbulence Modeling

In this chapter, the approximate inertial manifold proposed in chapter III is constructed for two canonical turbulent flows, the one-dimensional Kuramoto-Sivashinsky equation and homogeneous isotropic turbulence (HIT) governed by the Navier-Stokes equations. Current theories prove the existence of an inertial manifold for the KSE and provide an estimate of the lowest dimension of such manifold [183]. The KSE has been studied extensively by approximate inertial manifolds. However, the range of parameters considered in previous works is such that the spatiotemporal chaotic behavior is not reached. Here, the KSE is studied in the fully chaotic regime to assess different aspects of AIM formulation. Also, the AIM approach is tested for homogeneous isotropic turbulence, which is the first such study to the authors' knowledge. Compared to KSE, HIT introduces two challenges: 1) current theories cannot prove the existence of an IM for the Navier-Stokes equations even in two dimensions, 2) there is a dimensional jump compared to any other system an AIM is constructed for in previous studies.

4.1 A priori analysis of AIM for turbulent flows

First, an *a priori* study is conducted to examine the validity of AIM assumptions and to obtain an estimation of inertial manifold dimension for each of these systems over

a range of parameters. Accordingly, this study does not focus on model development, since the full-dimensional dynamical system is solved for the *a priori* analysis. However, the formulation provides a clear path to develop an AIM-based ROM as explained in Chap. III.

4.1.1 Kuramoto-Sivashinsky equation-based spatiotemporal chaos

The Kuramoto-Sivashinsky equation has been used as a surrogate for studying turbulence and interfacial instabilities [202–204]. The KSE is a convection-diffusion equation written as

$$\begin{aligned} &\frac{\partial \xi}{\partial t} + \xi \frac{\partial \xi}{\partial x} + \frac{\partial^2 \xi}{\partial x^2} + \mu \frac{\partial^4 \xi}{\partial x^4} = 0 \ , \ x \in R, \ t > 0 \\ &\xi(x,t) = \xi(x+L,t); \ \xi(x,0) = g(x), \end{aligned} \tag{4.1}$$

where t is time, x is physical space, ξ is the solution of the equation, L is the spatial period, and μ is viscosity. The dynamics of the system are controlled by two parameters: L and μ. It is then possible to define a Reynolds number type parameter as $\mathrm{Re} = \frac{L}{2\pi\sqrt{\mu}}$ [205], where the extent of spatiotemporal chaos is determined similar to the conventional use of this non-dimensional number. The range of scales in the system can be modified by changing Re. In this study, viscosity is kept constant at $\mu = 0.001$, and the length of the domain is varied in the range of $[10\pi, 64\pi]$. The AIM will be investigated for this range of parameters.

To cast the KSE in a dynamical system framework, spectral discretization is used. Let v be the Fourier transform of ξ,

$$v(k,t) = \mathcal{F}(\xi(x,t)) = \frac{1}{L} \int_0^L \xi(x,t) e^{-iq_k x} dx, \tag{4.2}$$

where $q_k = \frac{2\pi k}{L}$, $k \in \mathbb{Z}$, and $\mathcal{F}$ is the Fourier transform operator. In discretized form, n_F Fourier coefficients are used for v, denoted by v_k with $k \in [-n_F/2+1, n_F/2]$. The

governing equation of the system in spectral space is obtained as a Galerkin projection of the Fourier modes,

$$\frac{d}{dt}v_k + (\mu q_k^4 - q_k^2)v_k + \frac{iq_k}{2} \sum_{\substack{1 \le |l| \le n_F/2 \\ 1 \le |k-l| \le n_F/2}} v_l v_{k-l} = 0. \tag{4.3}$$

Fourier modes with large wavenumbers have low amplitude and can be neglected at sufficiently large n_F. The exact solution of the full-dimensional system is obtained by solving Eq. 4.3 using the exponential time difference fourth-order Runge-Kutta method (ETDRK4) [206, 207] with standard 3/2 de-aliasing. The initial condition of the dynamical system in physical space (Eq. 4.1) is $g(x) = \sin(x)(1 + \cos(x))$. For the range of domain sizes considered here, this computation can become expensive. The required grid resolution is provided in Tab. 4.1. For this reason, an MPI-based domain decomposition approach is used to solve the system on distributed memory computers.

4.1.1.1 Numerical stability requirements

The KSE exhibits spatiotemporal chaos, where infinitesimal perturbations exponentially grow over time. Therefore, the numerical resolution (in time and space) used to resolve the system has a significant impact on the accuracy and stability of the solution. The range of scales found in the system increases with the length of the domain. As a result, the number of Fourier modes needed to resolve the dynamics also changes. Figure 4.1 shows a typical $x - t$ plot of the solution ξ for a Reynolds number 316.23 using 4096 Fourier modes. Initially, spatial variations retain the physical structure of the initial conditions. At $t > 0.15$, transition to a chaotic regime is observed. However, with 1024 Fourier modes for the same Reynolds number, the solution becomes unstable after the transition to the chaotic regime and blows up.

These simulations with coarser resolution represent truncated systems without any subgrid model.

As expected, when sufficient spatial resolution is not available, the energy dissipation is not fully captured and there can be a pile-up of energy at the small scales, which leads to numerical instability. Since one of the objectives of this work is to determine whether an AIM approximation is useful as a modeling path, the errors associated with the AIM process will be compared to those of the minimum resolution needed to evolve the governing equations stably. In other words, if the AIM approach shows good accuracy when using a smaller number of Fourier modes, it will provide a computational benefit when compared to the minimum resolution needed to solve the equations stably. Table 4.1 shows the required minimum resolution for the stability of the solution for different Re values as well as the maximum resolution used in the high fidelity solution of this study. By increasing the number of Fourier modes beyond the minimum resolution, the size of structures captured in the chaotic regime decreases. A grid convergence study is done at each Re number. The highest resolution grid is considered as the exact solution, and the L_2 norm of the difference between coarser grids solution and exact solution is monitored as convergence metric. The high fidelity simulation is called DNS in this study since the governing equations are solved without any modeling. When discussing the AIM resolution (m in Chap. III), the minimum resolution will be used as a reference.

Case	Length of domain	Re	N_{min}	N_{DNS}
A	10π	158.11	1024	2048
B	20π	316.23	2048	4096
C	36π	569.21	4096	8192
D	64π	1011.93	8192	16384

Table 4.1: Grid convergence study of the KSE for different Re numbers. N_{min} denotes the minimum number of modes required to obtain a stable solution. N_{DNS} is the number of modes used to obtain the high fidelity solution.

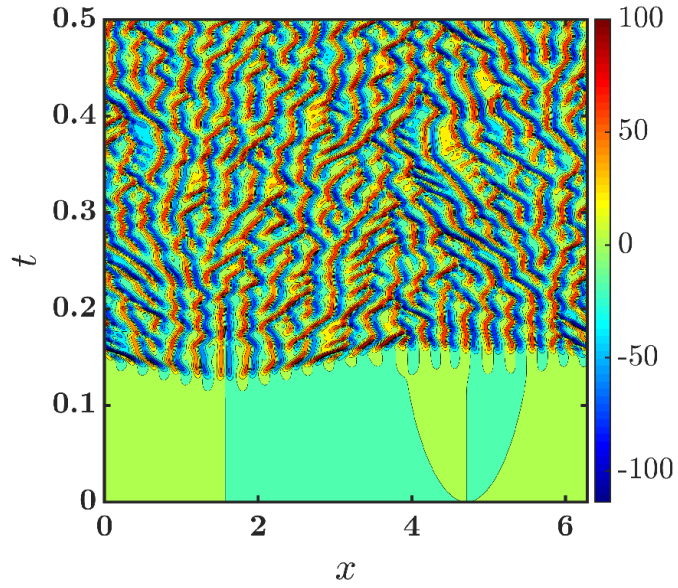

Figure 4.1: Solution of the KSE, $\xi(x,t)$, for $Re = 316.23$, $N_{DNS} = 4096$. Only part of the computational domain is shown.

4.1.1.2 Construction of an AIM for the KSE

The existence of an IM has been proven for the KSE [183, 208]. In the IM formulation, Eq. 4.3 can be arranged as Eq. 3.2 with the linear operator $\mathcal{A} = \mu q_k^4$ and $\mathcal{R}(v) = -q_k^2 v_k + i\frac{q_k}{2}\sum v_l v_{k-l}$ or their physical space analog. The KSE has two linear operators, but only one of them (μq_k^4) satisfies properties of $\mathcal{A}$ (i.e., linear, unbounded, and self-adjoint) required by the theory of inertial manifolds. While the second-derivative term ($-q_k^2$) is responsible for instability at large scales, the fourth-derivative term provides damping at the small scales. In this formulation, the projection operator is defined in the spectral domain by the first m eigenvectors of $\mathcal{A}$; $\boldsymbol{P}$ is a diagonal matrix with μq_k^4 as its diagonal entries. By applying the projection operators into Eq. 4.3, governing equations of resolved and unresolved subspaces are obtained,

$$\frac{d}{dt}u_k + (\mu q_k^4 - q_k^2)u_k + \frac{iq_k}{2}\boldsymbol{P}\Bigg(\sum_{\substack{1 \le |l| \le n_F/2 \\ 1 \le |k-l| \le n_F/2}} v_l v_{k-l}\Bigg) = 0, \tag{4.4}$$

and

$$\frac{d}{dt}w_k + (\mu q_k^4 - q_k^2)w_k + \frac{iq_k}{2}\boldsymbol{Q}\Bigg(\sum_{\substack{1 \le |l| \le n_F/2 \\ 1 \le |k-l| \le n_F/2}} v_l v_{k-l} \Bigg) = 0. \tag{4.5}$$

Resolved variables are $\boldsymbol{u} = (v_{-m/2}, ..., v_{m/2})$, and the unresolved variables are $\boldsymbol{w} = (v_{-n_F/2+1}, ..., v_{-(m+1)/2}, v_{(m+1)/2}, ..., v_{n_F/2})$. With the AIM approximation, the unresolved modes can be sought as the solution of

$$w_k^{j+1} = (\mu q_k^4)^{-1}\Bigg(q_k^2 w_k^j - \frac{iq_k}{2}\boldsymbol{Q}\Bigg(\sum_{\substack{1 \le |l| \le n_F/2 \\ 1 \le |k-l| \le n_F/2}} (u, w^j)_l (u, w^j)_{k-l} \Bigg)\Bigg), \tag{4.6}$$

where j is the index of iteration. Equation 4.6 is solved by an iterative method. It is shown that Eq. 4.6 has a unique solution [183]. However, seeking the fixed-point solution of this equation can be expensive, since the nonlinear term should be computed at each iteration. Most of the following analysis has been done with $j = 1$ unless otherwise mentioned. This provides a first-order approximation of the unresolved dynamics, which is a common practice in an approximation of inertial manifolds [174, 183]. The second-derivative term does not appear in Eq. 4.6 for $j = 1$, and the nonlinear term is computed only by the resolved variables. With this approximation, $\boldsymbol{w} = \Phi(\boldsymbol{u})$, and an AIM is constructed as $\Phi : \boldsymbol{P}\mathcal{H} \to \boldsymbol{Q}\mathcal{H}$.

4.1.1.3 Validity of the AIM formulation for the KSE

One of the key assumptions in the AIM methodology is that the linear operator dominates and controls the unresolved dynamics. In the KSE, the linear operator is dissipative in nature. If dissipation dominates the unresolved dynamics, the energy of high wavenumber modes is exponentially dissipative and asymptotically small. This fact reinforces the notion that long-time dynamics of the system lie in the inertial

manifold. This assumption is evaluated using the energy budget of the governing equation for case A in Tab. 4.1. Figure 4.2 shows the energy budget for different quantities in the unresolved dynamics, each plotted using an AIM resolution of $m = 158$, which is equal to the number of linearly unstable modes in this case. The number of linearly unstable modes is found by linearizing Eq. 4.3 at its trivial solution and computing the eigenvalues of its linear operator. Eigenvalues with positive real parts correspond to the linearly unstable modes. In this case, the eigenvalues are: $\lambda_k = q_k^2(1 - \mu q_k^2)$, which gives [Re] eigenvalues with positive real part, where [Re] is the integer part of Re.

To obtain the linear and nonlinear terms in Eqs. 4.4 and 4.5, the solution $\boldsymbol{v}$ from the high fidelity computation is projected onto the resolved and unresolved spaces using the operators $\boldsymbol{P}$ and $\boldsymbol{Q} = \mathcal{I} - \boldsymbol{P}$, respectively. For the KSE, $\boldsymbol{P}$ is the projector onto the span of the first m eigenvectors of the linear operator $\mathcal{A} = \mu q_k^4$. The nonlinear operator is computed using the DNS data and is then projected onto the resolved and unresolved spaces.

The energy budget, defined as the magnitude of each term for the evolution in spectral space, is shown in Figs. 4.2 and 4.3. For the unresolved scales, the magnitude of the linear term is comparable to that of the nonlinear term. This trend holds for the first unresolved mode as well as the average of all the unresolved modes. The linear operator gains more energy at the small scales because of the strong dissipative nature of the KSE. On the other hand, for the resolved modes (shown in Fig. 4.3), the nonlinear term is substantial compared to the linear term, which is consistent with the chaotic nature of this system. It is also seen that the average of all resolved terms shows that both operators are of roughly similar magnitude. This is because the modes close to the cut-off wavenumber (i.e., close to $m = 158$) have a robust linear term (as seen for the first unresolved mode). As m is increased, the unresolved modes will be increasingly dominated by the linear operator.

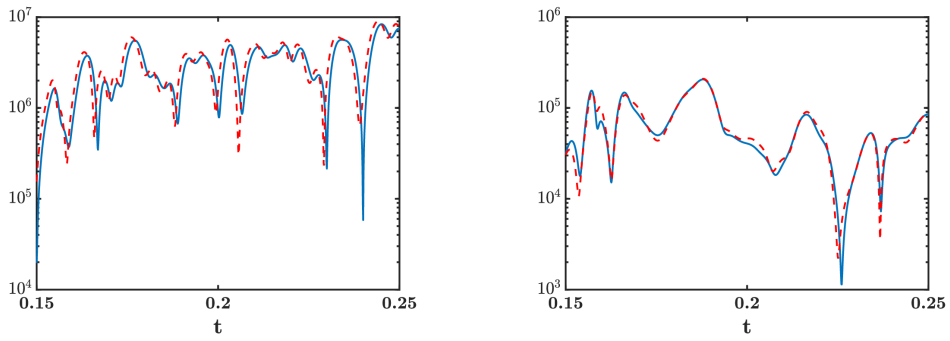

Figure 4.2: Energy budget for the unresolved dynamics (Eq. 4.5) of the KSE for $\mathrm{Re} = 158.11$, $m = 158$. Linear term ($\mathcal{A}\boldsymbol{w}$): —, nonlinear term ($\boldsymbol{Q}\mathcal{R}(\boldsymbol{u}, \boldsymbol{w})$): - -. Left: energy budget of the first unresolved mode. Right: average energy budget of the unresolved dynamics.

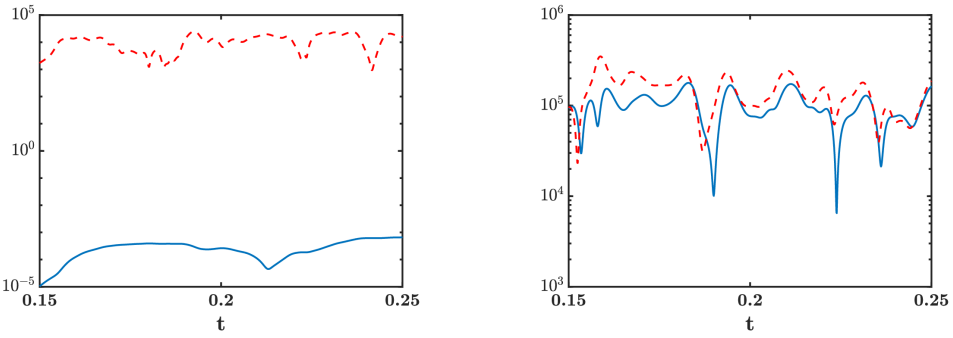

Figure 4.3: Energy budget for the resolved dynamics (Eq. 4.4) of the KSE for $\mathrm{Re} = 158.11$, $m = 158$. Linear term ($\mathcal{A}\boldsymbol{u}$): —, nonlinear term ($\boldsymbol{P}\mathcal{R}(\boldsymbol{u}, \boldsymbol{w})$): - -. Left: energy budget of the first resolved mode, right: average energy budget of the resolved dynamics.

An interesting aspect of the results in Figs. 4.2-4.3 is that the first unresolved mode has more energy than the resolved modes. Figure 4.4 shows the energy spectrum of the KSE for $\mathrm{Re} = 158.11$. The vertical dashed line marks the cut-off wavenumber in the AIM projection for $m = 158$. At this AIM resolution, the cut-off wavenumber is in the inertial range of the energy spectrum, and it is discernible that the energy of the first unresolved mode is more than the energy of some of the resolved scales. This behavior in the KSE energy spectrum is because of the destabilizing effect (second derivative term) in large scales which increases energy towards higher modes before

viscosity becomes dominant. This shows that decomposition in AIM is not about relative energy content alone, but the separation of time scales. In the following sections, it is shown that even with such differences in energy content the method is relatively accurate. This provides confidence in the transferability of the model to situations where at least a portion of the small scales might have more energy than some of the larger scales.

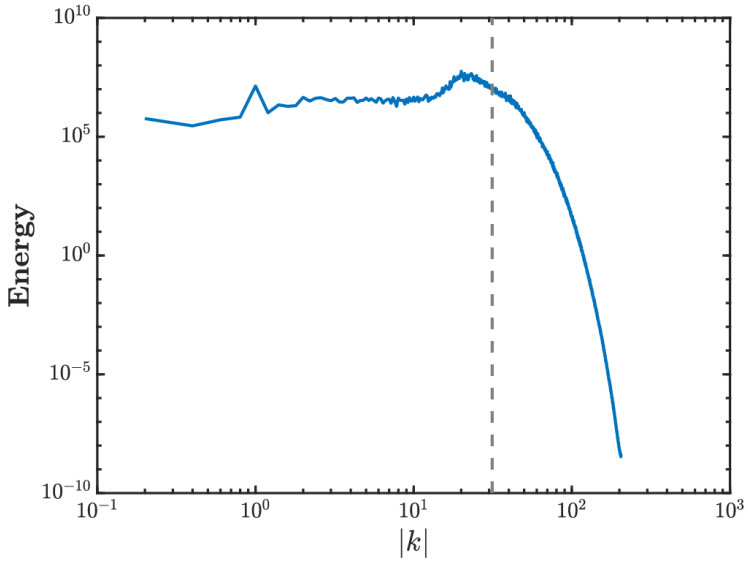

Figure 4.4: Energy spectrum of the KSE for Re = 158.11.

4.1.1.4 Dimension of AIM

The primary AIM outcome is the determination of the unresolved dynamics based on the evolution of the resolved scales. To understand the accuracy of this approach, an *a priori* analysis is conducted. As mentioned in Chap. III, current theories can prove the existence of an IM for some dissipative systems, although they cannot determine its dimension and topology explicitly. Therefore, an estimation of the inertial manifold is essential. As the IM attracts all trajectories exponentially, its approximation must contain a thin neighborhood of the IM. Therefore, m should be larger than the dimension of the IM. However, obtaining this dimension is a computational challenge

in itself, and is currently infeasible [34, 37, 38, 209]. Previous studies have estimated the dimension of IM for the KSE and provided an upper-bound scaling with different powers of Re [174, 183]. Here, the relation of the AIM accuracy to this dimension estimate is assessed.

For each Re, different projection operators leading to various resolutions of AIM are considered, and unresolved quantities are approximated by Eq. 4.6. They are then compared against the high fidelity solution of the dynamical system projected onto the unresolved subset. The results are first shown in Fig. 4.5, where the real part of the first unresolved mode is plotted. It is seen that as m increases, the AIM assumption becomes increasingly accurate, with the predicted field accurately tracking the exact quantity in time. Note that the number of resolved modes m is well below the minimum required to reach stability with a truncated system (Tab. 4.1). Figure 4.6 shows the evolution of the average of unresolved quantities with time. It is seen that, similar to the first unresolved mode, increasing the AIM dimension (m) increases the accuracy of the results. However, the improvement is not as marked as for the first unresolved mode. From these figures, it is concluded that the modes closest to the resolved space are more responsive to the resolved-scale dynamics. This trend is shown more clearly in Sec. 4.1.1.5.

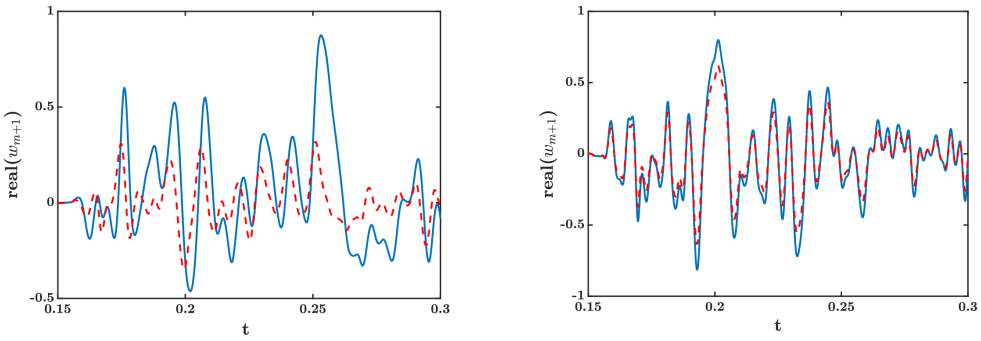

Figure 4.5: Effect of the AIM resolution m, on approximation of the dominant unresolved mode (w_{m+1}) for Re = 1011.93. DNS:—, AIM: - -. Left: $m = 1024$, right: $m = 2048$.

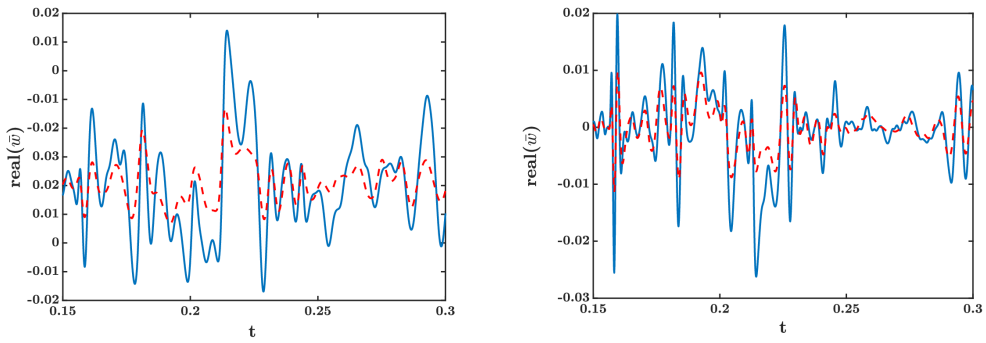

Figure 4.6: Effect of the AIM resolution on approximation of the average of unresolved dynamics ($\bar{w}$) for Re = 1011.93. DNS:—, AIM: - -. Left: $m = 1024$; right: $m = 2048$.

Even though the AIM estimation degrades at higher wavenumbers, the overall performance improves with increasing AIM resolution. Figure 4.7 shows the L_2-norm of the difference between the $\boldsymbol{w}$ field obtained using AIM (Eq. 4.6) and the unresolved sub-space of the full system solution (Eq. 4.3), expressed in the spectral space as a function of AIM resolution over the range of Re numbers. Regardless of the Re number used, after an initial reduction, the error appears to plateau before decreasing further. Incidentally, the switch from the plateau to the second convergence branch occurs when AIM resolution m exceeds the bifurcation parameter, Re. Given that prior work has shown that the dimension of the inertial manifold scales as Re [174, 183], this result suggests that strong convergence properties can be obtained for resolutions higher than the dimension of the inertial manifold. At low m, it is postulated that the initial error reduction occurs primarily because the resolved modes increasingly capture the key macroscopic features. A constant rate of convergence is not expected due to the highly nonlinear nature of the resolved scales dynamics [210].

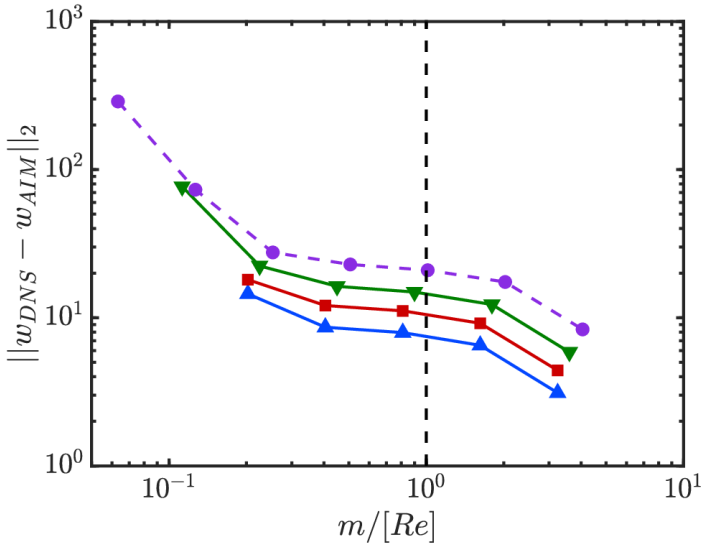

Figure 4.7: Effect of AIM resolution on estimation of the unresolved dynamics $||\boldsymbol{w}_{DNS} - \boldsymbol{w}_{AIM}||_2$. Re = 158.11: ▲, Re = 316.23: ■, Re = 569.21: ▼, Re = 1011.93: ●. Vertical dashed line marks m = [Re].

While the comparisons so far have been in spectral space, it is illustrative to consider the physical space features captured by the AIM model. For this purpose, two different resolutions of the AIM are considered for Re = 158.11. Figures 4.8 and 4.9 show the different fields for the AIM resolutions $m = 128$ and $m = 256$, corresponding to the full-dimensional reconstructed field and the unresolved dynamics, respectively. For a clearer representation of the small scales, only part of the simulation domain is shown for the chaotic regime ($t > 0.15$). Before the transition to this regime, the dynamics are laminar and captured by large wavelength resolved-scale modes.

Figure 4.8 compares the AIM-reconstructed fields ($\mathcal{F}^{-1}(\boldsymbol{u}, \boldsymbol{w}_{AIM})$) by two different AIM resolutions against the high fidelity (DNS) solution. The reconstructed field retains the features of the full field, even at the lower resolutions considered. For $m = 256$, the AIM-reconstructed field appears to retain most of the details of the flow qualitatively. However, these are full-dimensional fields reconstructed from the AIM approximation and resolved fields. In Fig. 4.9, a comparison of the exact and approximated unresolved fields is revealing of the effect of the AIM dimension in

approximating the unresolved modes. In particular, it is seen that the extrema in the reconstructed field are smaller in magnitude in comparison to those of the original field. While this improves with the resolution, there remain differences in the spatiotemporal structures at $m = 256$.

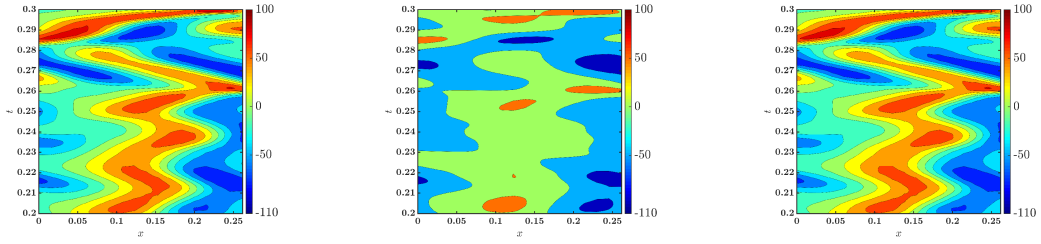

Figure 4.8: KSE solution in physical space for Re $= 158.11$, $n_g = 2048$. Left: full-dimensional solution ($\xi(x,t)$) obtained by DNS; reconstructed solution by AIM with $m = 128$ (middle) and $m = 256$ (right).

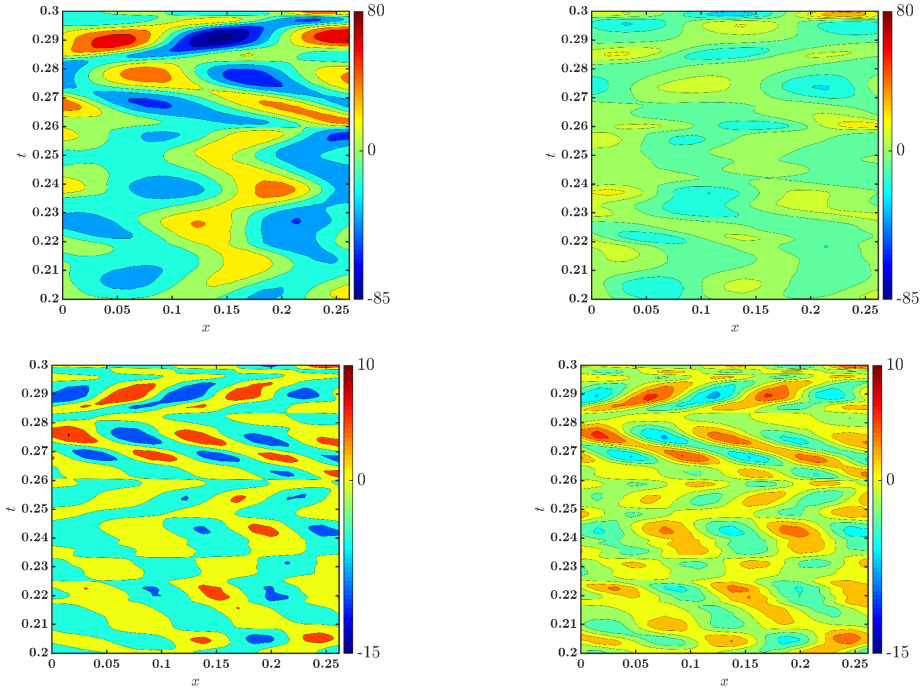

Figure 4.9: Unresolved dynamics of the KSE solution in physical space for Re $= 158.11$, $n_g = 2048$; Top left: DNS solution ($\boldsymbol{Q}\xi(x,t)$) for $m = 128$, top right: AIM estimation by Eq. 4.6 for $m = 128$, bottom left: DNS solution ($\boldsymbol{Q}\xi(x,t)$) for $m = 256$ and bottom right: AIM estimation by Eq. 4.6 for $m = 256$.

4.1.1.5 Accuracy of statistical features

While the focus so far has been on the ability of AIM to capture the dynamics of the underlying system, it is essential to understand the impact on the statistical properties of the system. For this purpose, the two-point spatial correlation $R(r,t) = \langle \xi(x,t)\xi(x+r,t) \rangle$, is computed for the DNS and AIM-reconstructed fields. Figure 4.10 (left) shows the convergence of the AIM solution to the exact solution by increasing the dimension of the AIM. Although the highest AIM resolution, (m), is significantly lower than the DNS resolution and the minimum resolution required for stability, it can capture the exact two-point correlation fairly accurately. Figure 4.11 shows the energy spectrum plotted in spectral space. Discrepancies in the modeled spectrum can be observed, especially at high wavenumbers. Nevertheless, AIM captures the energy of the largest unresolved scales quite accurately (for $|k| \in [50, 100]$), indicating that their dynamics are indeed enslaved to the largest resolved scales. However, the small scales appear to have lower energy in the AIM reconstruction, indicating that the approach to the manifold is not purely determined by the scale-specific time-scale, which tends to be smaller at larger wavenumbers. This behavior is also seen in the spatial correlations of the unresolved dynamics alone, $\boldsymbol{w}$. Figure 4.10 (right) shows that for larger separations ($r/L > 0.05$) the two-point correlation is well represented by the AIM reconstruction of the small-scales, while the amplitude of these correlations is not captured at shorter separation distances.

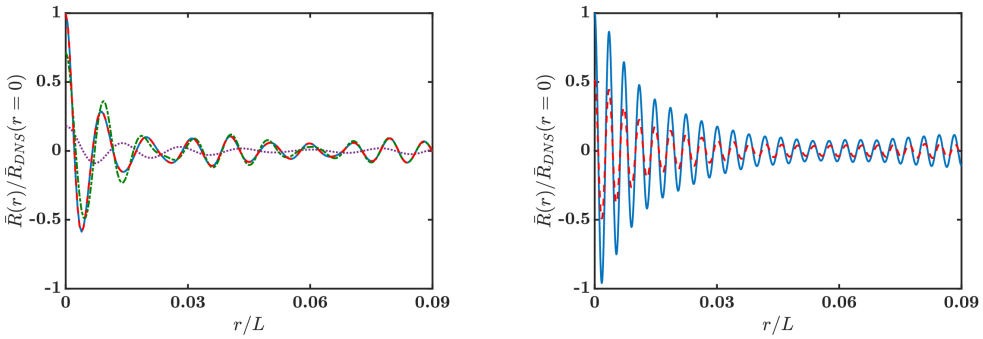

Figure 4.10: Spatial two-point correlation of velocity field in physical space for $\mathrm{Re} = 158.11$. Left: convergence to DNS by increasing AIM resolution m, obtained for full vector of variables (u, w). DNS: —; AIM, $m = 64$: ···; AIM, $m = 128$: - · -; AIM, $m = 256$: - -. Right: Spatial-correlation of unresolved space (w) for $m = 256$. DNS: —; AIM: - -. In both plots, all values are normalized by the corresponding spatial correlation at $r = 0$ obtained by DNS.

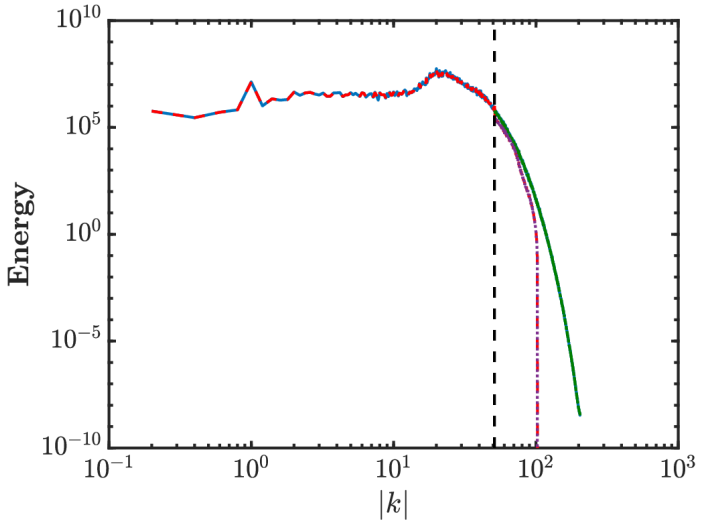

Figure 4.11: Energy spectrum for $\mathrm{Re} = 158.11$, $m = 256$. DNS: —; AIM: - -; exact subgrid spectrum: - · -; subgrid spectrum approximated by AIM: · · ·. The vertical dashed line marks the cut-off wave number.

The energy spectrum and the two-point correlation show that the AIM approximation deteriorates at the smallest scales in the unresolved dynamics. However, the approximation can be improved by seeking the fixed-point solution of Eq. 4.6 with more iterations. Figure 4.12 (left) shows that with $j = 3$ in Eq. 4.6, the AIM approx-

imation has improved considerably at higher wavenumbers, and the energy spectrum is reconstructed at the smallest scales. The rate of convergence is controlled by the quadratic nonlinearity in Eq. 4.6 which correlates with different scales. Figure 4.12 (right) compares the normalized error of the energy spectrum of the unresolved modes obtained using different numbers of iterations. At each iteration, the number of unresolved modes correlated with the resolved dynamics is doubled because of the quadratic nonlinearity. By considering more iterations, the information in the resolved and larger unresolved scales is transferred to the smaller scales, which improves the performance of the approximation. Since the dimension of the unresolved dynamics is finite, increasing the number of iterations after some point does not improve the approximation anymore. In the discussions above, only the $j = 1$ solution is considered, since this provides a first-order approximation of the unresolved dynamics.

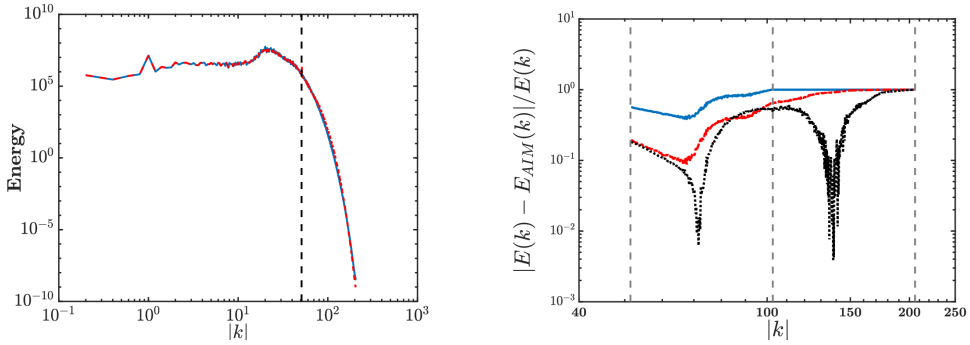

Figure 4.12: Left: Energy spectrum for Re = 158.11, $m = 256$. The unresolved dynamics are reconstructed by Eq. 4.6 with $j = 3$; DNS: —, AIM: - -. Right: relative error in energy spectrum of the unresolved dynamics for Re = 158.11, $m = 256$, when unresolved dynamics are approximated by Eq. 4.6 with $j = 1$: —, $j = 2$: - - and $j = 3$: -·-. Vertical dashed lines mark wavenumbers k_m, $2k_m$ and $4k_m$.

4.1.2 Homogeneous isotropic turbulence

In this section, the performance of the proposed AIM is assessed *a priori* for a canonical

turbulent flow evolving in a cube of side length 2π m. This problem represents a jump in complexity for two reasons: 1) the dimensionality of the discretized system is increased by orders of magnitude; 2) the existence of an IM has not yet been proven for the Navier-Stokes equations [98]. The flow is considered incompressible, and the three-dimensional Navier-Stokes equations govern the state of the system

$$\begin{aligned} &\frac{\partial \xi_i}{\partial t} + \xi_j \frac{\partial \xi_i}{\partial x_j} = -\frac{1}{\rho}\frac{\partial p}{\partial x_i} + \mu \frac{\partial}{\partial x_j}(\frac{\partial \xi_i}{\partial x_j}) + B\xi_i \\ &\frac{\partial \xi_i}{\partial x_i} = 0, \end{aligned} \tag{4.7}$$

where ξ_i is the velocity component in the i^{th} direction, p is the hydrodynamic pressure, μ is the kinematic viscosity and ρ is the density. Statistical stationarity is achieved by using a turbulent forcing technique that compensates for the viscous dissipation. A linear forcing scheme is used with a uniform constant-coefficient B [211, 212]. It should be mentioned that IM theories are developed for nonstationary systems [98, 163], but for decaying turbulence, the Re number and subsequently dimension of the attractor are decreasing. Therefore, it is not fair to assess an AIM with a fixed dimension for long-term prediction of dynamical or statistical features of decaying turbulence.

4.1.2.1 HIT solution and numerical specifications

Similar to the procedure used for the KSE, Eq. 4.7 is expressed in Fourier space using $\xi_i = \sum_{\vec{k}} v_i(\vec{k}, t) e^{\vec{k}.\vec{x}}$. A Galerkin projection of the equation leads to a system of ODEs that govern the evolution of the Fourier coefficients $v_i(\vec{k}, t)$,

$$\begin{aligned} &\frac{d}{dt} v_i(\vec{k}, t) + \mu |k|^2 v_i(\vec{k}, t) - B v_i(\vec{k}, t) + k_i \frac{\vec{f}.\vec{k}}{|k|^2} - f_i = 0 \\ &f_i = -\mathcal{F}(\frac{\partial \xi_i \xi_j}{\partial x_j})_{\vec{k}}, \end{aligned} \tag{4.8}$$

which is solved in a domain of $2\pi \times 2\pi \times 2\pi$ m with periodic boundary conditions. Similar to the KSE, a pseudo-spectral method with dealiasing is used for the non-linear

term. Exact time integration is used for the linear viscous term, and second-order Runge Kutta (RK2) is used for the other terms. Since small incompressibility errors can grow fast in a spectral formulation, it is necessary to remove the divergence error at every time step [213, 214]. At each time step, the velocity field is projected on the divergence-free space following the procedure explained in [213, App. A1].

Four different spatial resolutions are used to investigate the accuracy of the AIM methodology for different Reynolds numbers. The simulation details are provided in Tab. 4.2. The Taylor microscale Reynolds number $Re_\lambda = \frac{u'\lambda_g}{\mu}$ and the Kolmogorov length scale $\eta = (\frac{\mu^3}{\epsilon})^{1/4}$ are monitored over the initialization time to make sure the turbulent field is fully developed, where λ_g is computed as $\sqrt{15\frac{\mu}{\epsilon}}u'$ [6, Chap. 6], u' is the fluctuating velocity and ϵ is the dissipation of turbulent kinetic energy. At each resolution, the flow statistics are monitored for approximately 1000 eddy turnover times (τ) to ensure a fully-developed, forced, statistically stationary flow field. The long transient time is chosen to make sure that the forcing method does not lead to instability and energy pile-up at small scales. The AIM investigation period is started when the flow becomes statistically stationary. Figure 4.13 shows one snapshot of the magnitude of vorticity vector for different grid resolutions.

Case	Grid Resolution	Re_λ	$\eta/\Delta x$	Forcing coefficient (B)
I	32^3	15.7	1.22	0.1370
II	64^3	27.1	1.12	0.3275
III	128^3	39.34	1.18	0.825
IV	256^3	51.67	1.36	1.8

Table 4.2: Numerical setup for *a priori* analysis of AIM for HIT.

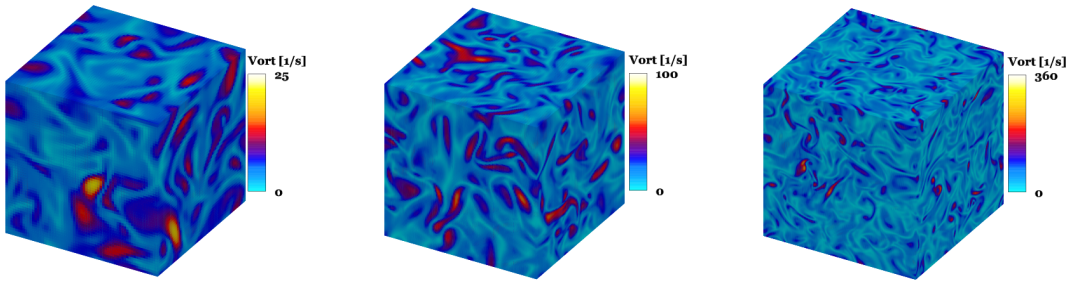

Figure 4.13: Instantaneous magnitude of vorticity vector obtained for different grid resolutions, left: $n_g = 64^3$, middle: $n_g = 128^3$ and right: $n_g = 256^3$.

4.1.2.2 Construction of an AIM for HIT

Equation 4.8 can be rearranged as Eq. 3.2 using the linear operator $\mathcal{A} = \mu|k|^2$, with $\mathcal{R}(\boldsymbol{v})$ containing all other terms. It should be noted that the constant forcing term is not included in the linear operator because it does not satisfy properties required by the theory of inertial manifolds (Chap. III). The projection operator $\boldsymbol{P}$, that defines the resolved subspace is spanned by the first m eigenvectors of the linear operator $\mathcal{A} = \mu|\vec{k}|^2$, and it is parameterized using a three-dimensional wavenumber k_m such that all the modes with wave numbers $\sqrt{k_x^2 + k_y^2 + k_z^2} \leq k_m$ are included in the resolved space. The number of modes satisfying this requirement is the dimension of AIM, (m). For example, $k_m = 2$ leads to $m = 23$. In the following sections, different values of k_m are used to examine the convergence properties of AIM. Figure 4.14 shows the separation of the resolved and unresolved subspaces in the wavenumber space. The highest wavenumber of the discretization is limited by the dealiasing, and higher modes are insignificant in the calculations.

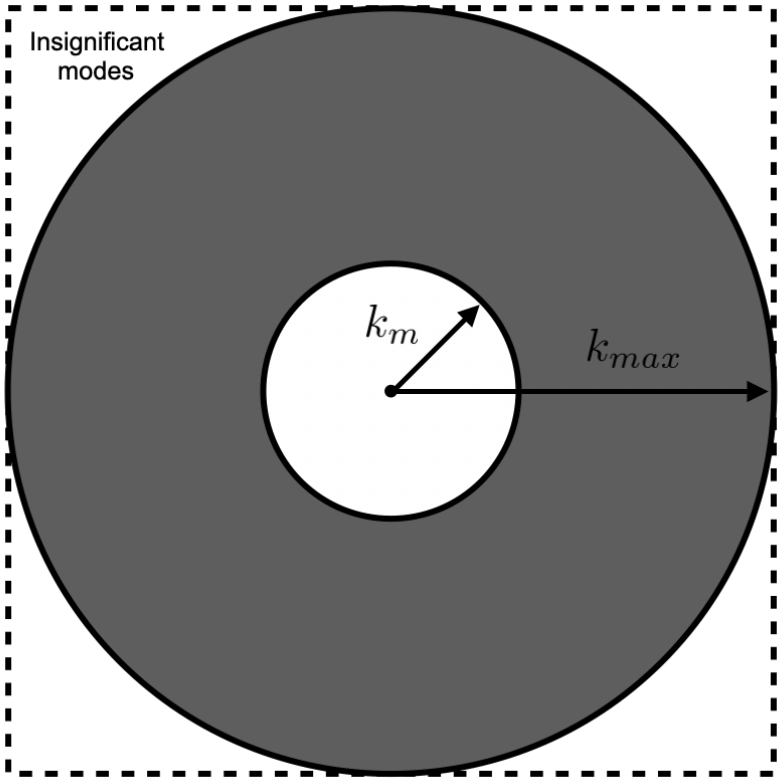

Figure 4.14: Representation of the resolved and unresolved subspaces in the wavenumber space. Circle with radius k_m encloses the resolved modes. Gray shaded area denotes the unresolved subspace. k_{max} is the highest wavenumber in DNS and unresolved dynamics calculations.

With the AIM approximation, $d\boldsymbol{w}/dt = 0$, the unresolved variables with wavenumber $\vec{k}$ can be approximated as

$$\boldsymbol{w}_{\vec{k}}^{j+1} = -(\mu|k|^2)^{-1}\boldsymbol{Q}\mathcal{R}(\boldsymbol{u}, \boldsymbol{w}^j), \tag{4.9}$$

where j is the iteration index. As mentioned in Chap. III, the unresolved dynamics can be approximated by solving Eq. 4.9 with a fixed-point iterative method.

One concern is that whether the reconstructed velocity field is physically constrained. It can be shown that the AIM approximation satisfies continuity conservation. If the initial guess of the sub-grid field is precisely divergence-free, regardless of

the iterative method, this approximation preserves this condition in the unresolved dynamics. However, if the initial guess of the unresolved velocity field does not satisfy the continuity equation, its residual error will grow exponentially. For the velocity vector corresponding to wavenumber $\vec{k}$ with initial guess $\boldsymbol{w}^0$ and j iterations in Eq. 4.9,

$$\begin{aligned} \bigtriangledown .\boldsymbol{w}^0_{\vec{k}} &= \epsilon, \\ \bigtriangledown .\boldsymbol{w}^j_{\vec{k}} &= \big((\mu|k|^2)^{-1}B\big)^j\epsilon, \end{aligned} \tag{4.10}$$

where ϵ is the residual of the continuity equation for the initial guess of the velocity vector. At each unresolved mode, the error grows at a rate proportional to the inverse of the wavenumber. Hence, the smallest unresolved scale (close to $|\vec{k}| = k_m$) has the highest growth rate.

4.1.2.3 Validity of the AIM for HIT

As discussed in Sec. 4.1.1.3 for the KSE, the key assumption in the AIM method is that the linear operator dominates the unresolved dynamics. In Navier-Stokes equations, the linear operator is the Stokes operator. Even though this operator is dissipative, and it possesses the required properties for AIM analysis (Chap. III), it does not satisfy the spectral gap condition enforced by available theories on the existence of an IM [98]. However, the existence of an IM for Navier-Stokes equations might be proven by theories with more relaxed prerequisites. If the linear operator is dominant in the unresolved dynamics, these dynamics are asymptotically small, and the long-time dynamics of the system lie in the IM. To compare the prevailing effect of the linear term in the resolved and unresolved sub-spaces, the variation of the energy budget of the linear and nonlinear terms of governing equations (Eqs. 3.9 and 3.10) are monitored over several eddy turnover times for case II in Tab. 4.2 with $k_m = 8$.

The linear and nonlinear terms, discussed in Sec. 4.1.2.2, are obtained from the

DNS computation, where the full-dimensional solution ($\boldsymbol{v}$) is projected onto the $\boldsymbol{u}$ and $\boldsymbol{w}$ subsets using the operators $\boldsymbol{P}$ and $\boldsymbol{Q} = \mathcal{I} - \boldsymbol{P}$, respectively. The energy budget is defined as the magnitude of each term in spectral space. The same analysis for the KSE in Sec. 4.1.1.3 shows that in the resolved subspace, the nonlinear terms are considerably larger. While approaching the unresolved subspace, the linear term gains more energy. The linear and nonlinear terms are of the same order of magnitude in the unresolved subspace of the KSE. Figure 4.15 shows the variation of the energy budget for the unresolved (left) and resolved (right) dynamics. In the resolved subspace of the HIT, the nonlinear term is dominant. However, unlike in the KSE, the linear operator is not important in the unresolved dynamics. Even though the linear term becomes larger in the unresolved part, the nonlinear term remains important for all modes. This behavior is consistent over different AIM resolutions (different k_m values) until the truncated system becomes as descriptive as the AIM.

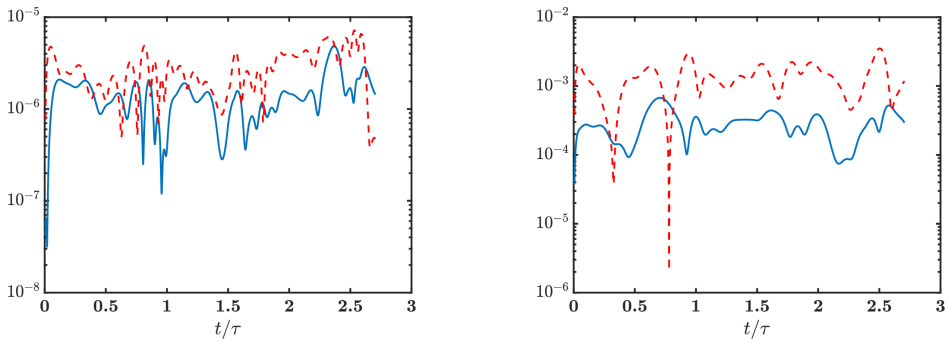

Figure 4.15: Energy budget of the governing equation for $n_g = 64^3$, $k_m = 8$, left: budget-study of the unresolved dynamics averaged over unresolved sub-space, $|\vec{k}| > k_m$. Linear term, $\mathcal{A}\boldsymbol{w}$: —, nonlinear term, $\boldsymbol{Q}\mathcal{R}(\boldsymbol{u}, \boldsymbol{w})$: - -. Right: budget-study of the resolved dynamics for $k \leq k_m$ averaged over all resolved modes. Linear term, $\mathcal{A}\boldsymbol{u}$: —, nonlinear term $\boldsymbol{P}\mathcal{R}(\boldsymbol{u}, \boldsymbol{w})$: - -.

4.1.2.4 Dimension of AIM

For each case in Tab. 4.2, different values of k_m are considered such that the number of degrees of freedom for the largest approximate inertial manifold is around 30 percent

of the degrees of freedom of DNS. The magnitude of the velocity field in physical space is shown in Fig. 4.16 for case IV (see Tab. 4.2) and $k_m = 32$. Figure 4.16 shows that the AIM-augmented field captures the dominant spatial features in the flow, even though the unresolved dynamics are overestimated.

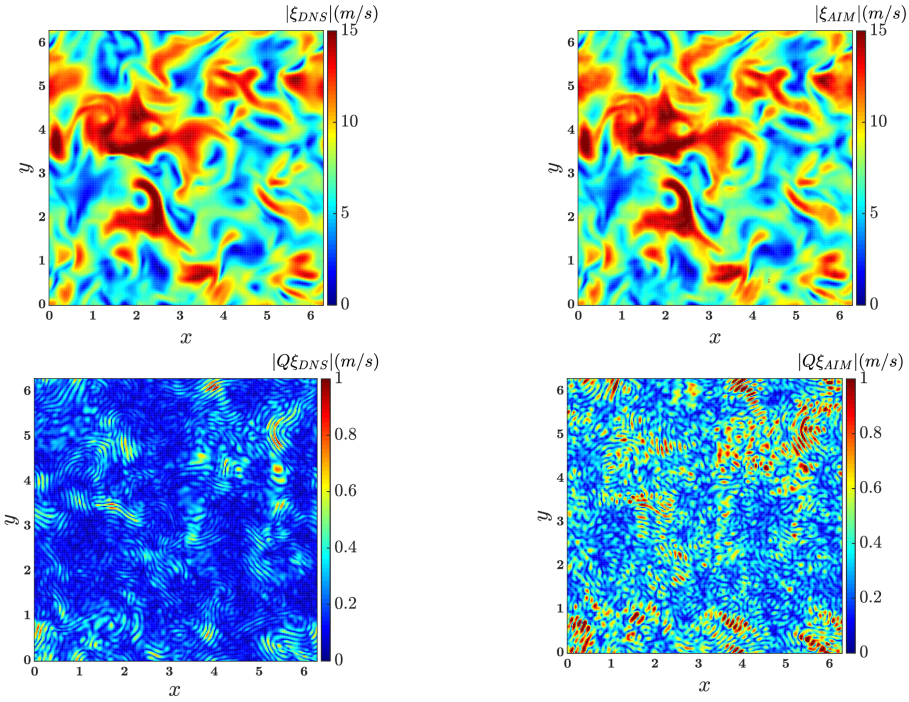

Figure 4.16: Magnitude of the velocity vector in a plane of the computational domain for $n_g = 256^3$, top left: DNS, top right: AIM-reconstructed field, bottom left: DNS field projected onto the unresolved subspace, and bottom right: approximated unresolved dynamics by AIM. The last three fields are obtained for $k_m = 32$, $m/n_g = 0.0042$.

Figures 4.17 and 4.18 show the effect of AIM resolution on accuracy. In all cases, by increasing the number of resolved modes AIM accuracy improves. Figure 4.18 shows that the dynamics of the sub-grid flow field are estimated with reasonable accuracy when using the information of the resolved modes alone (about five percent of the DNS modes). Figure 4.19 shows the L_2-norm of the difference between AIM estimation of the unresolved scales ($\boldsymbol{w}$) and the DNS solution as a function of AIM resolution (m). The error decreases with increasing resolution; similar to the results obtained with KSE, the rate of convergence is not constant. This behavior is consistent for all cases

with different DNS resolutions.

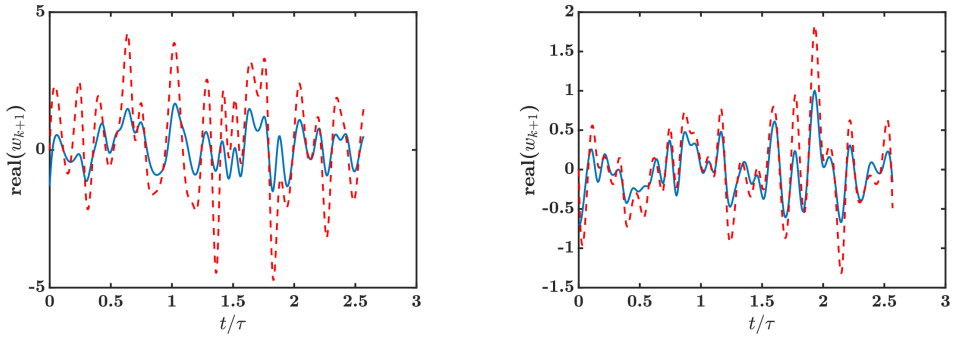

Figure 4.17: Effect of AIM resolution m, on the estimation of dominant unresolved mode for $n_g = 256^3$, left: $k_m = 32$, $m/n_g = 0.0042$, and right: $k_m = 72$, $m/n_g = 0.047$. DNS: —, AIM: - -.

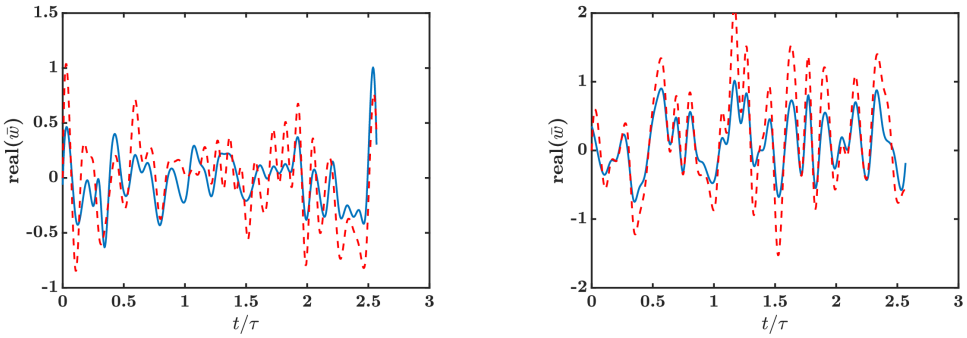

Figure 4.18: Effect of AIM resolution (m) on the estimation of average unresolved dynamics for $n_g = 256^3$. Left: $m/n_g = 0.0042$, right: $m/n_g = 0.047$. DNS: —, AIM: - -.

4.1.2.5 Statistical accuracy

Similar to the analysis of KSE in Sec. 4.1.1.5, the AIM modeling is assessed in terms of the statistics of the approximated flow field. The turbulent kinetic energy spectrum reconstructed with AIM is compared to that of DNS in Fig. 4.20 (top left), showing that the spectrum differs fundamentally from that of the KSE. The largest wavenumbers of the unresolved scales are not approximated accurately, which can cause stability issues in a modeling setup. This behavior can have two possible explanations which are discussed below.

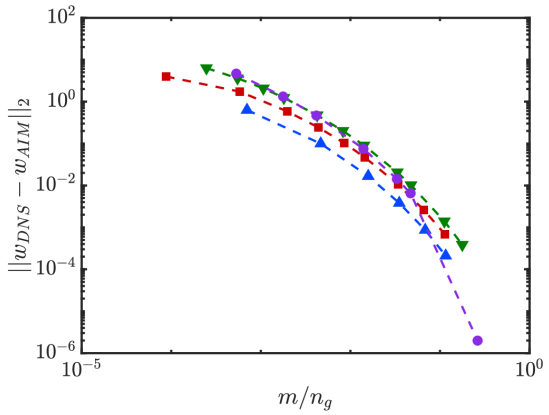

Figure 4.19: Effect of AIM resolution (m) on L_2-norm of the difference between exact and approximated unresolved dynamics $||\boldsymbol{w}_{DNS} - \boldsymbol{w}_{AIM}||_2$. $n_g = 32^3$: ▲, $n_g = 64^3$: ■, $n_g = 128^3$: ▼, $n_g = 256^3$: ●.

In the governing equations of HIT, the forcing term is linear but counteracts dissipation, which is combined with other nonlinear terms in AIM formulation,

$$\begin{aligned} &\frac{d}{dt}v_i(\vec{k},t) + \mu|k|^2 v_i(\vec{k},t) - Bv_i(\vec{k},t) + k_i\frac{\vec{f}.\vec{k}}{|k|^2} - f_i = 0, \\ &\mathcal{A}v_i = \mu|k|^2 v_i(\vec{k},t), \\ &\mathcal{R}(v)_i = -Bv_i(\vec{k},t) + k_i\frac{\vec{f}.\vec{k}}{|k|^2} - f_i. \end{aligned} \tag{4.11}$$

Estimating the unresolved dynamics with only one iteration ($j = 1$) in Eq. 4.9 neglects the forcing term. The impact of this formulation is not critical at higher wavenumbers ($|\vec{k}| >> k_m$), where the dissipative linear operator ($\mathcal{A} \propto |\vec{k}|^2$) becomes more dominant compared to the constant linear forcing coefficient (B). Therefore, there is no energy over-estimation at small scales. This may explain the discrepancy between AIM and DNS in the unresolved modes close to the cut-off wavenumber. To examine this explanation, the following experiment is conducted: the influence of the forcing term is removed by performing AIM on HIT and forcing only large scales to sustain turbulence. In this case, the forcing coefficient B is zero for unresolved modes. Figure 4.20 (top right) shows that AIM performance is improved when unresolved

modes are not forced. However, there is still a small overestimation of energy close to the cut-off wavenumber.

Furthermore, this persistent error in the energy spectrum may be related to the first order (one iteration, $j = 1$) approximation in Eq. 4.9. Approximating unresolved dynamics with additional iterations could be used to test this conjecture. Considering Eq. 4.9 with $j = 1$, the nonlinear term only accounts for the interaction between the resolved scales. Implementing a fixed-point iterative method for solving Eq. 4.9 will include interactions among all scales in the resolved and unresolved sub-spaces. Previous studies of the two-dimensional Navier-Stokes equations have shown that the fixed-point iteration has a unique bounded solution with a convergence rate exponentially proportional to the smallest eigenvalue of the linear operator projected onto the unresolved subspace ($\mathcal{A}|_{\boldsymbol{Q}\mathcal{H}}$) [187].

The unresolved dynamics are approximated by a preconditioned nonlinear Newton method. To ensure robustness, a successive over-relaxation (SOR) approach is used instead of the Newton scheme [215]. Figure 4.20 (bottom) shows that higher-order estimation with only three iterations and SOR coefficient of 0.2 removes the energy build-up issue. This higher-order estimation is more effective closer to the cut-off wavenumber, which is in the inertial range of the energy spectrum where the nonlinearity of the energy cascade dominates the dynamics.

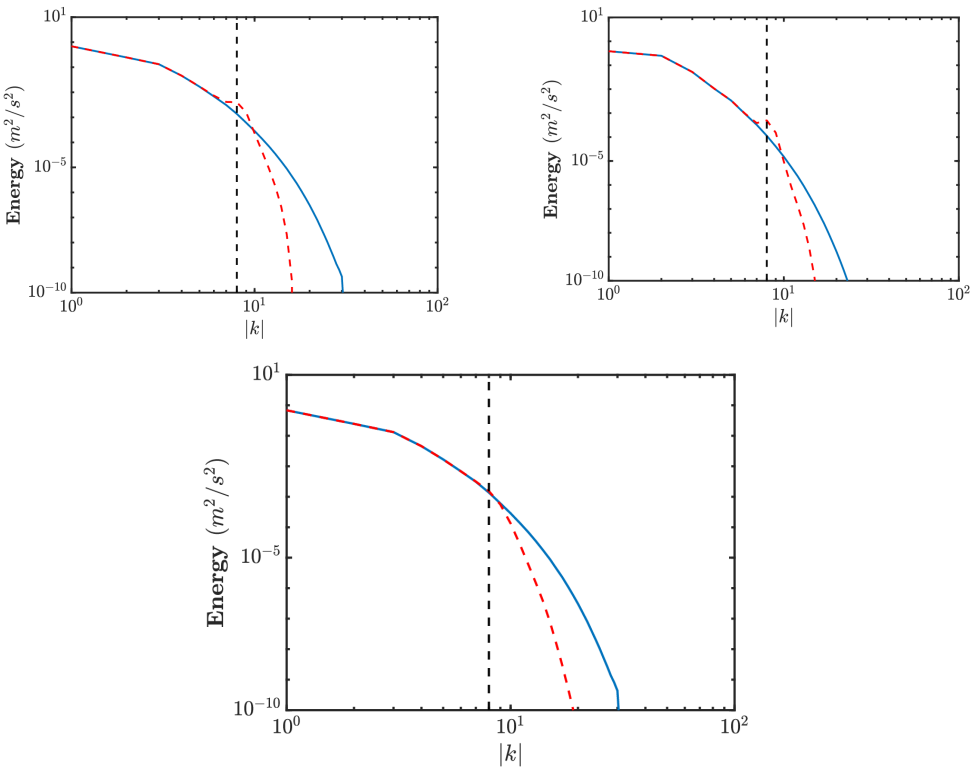

Figure 4.20: Energy spectrum reconstruction for $n_g = 64^3$, $k_m = 8$. Top left: all scales are uniformly forced and $j = 1$ in Eq. 4.9, top right: only resolved scales are forced and $j = 1$ in Eq. 4.9, and bottom: all scales are uniformly forced with $j = 2$ in Eq. 4.9. DNS: —, AIM: - -.

4.1.2.6 Higher order statistics

In modeling the small-scale structures of the field from information at the large scales, the vorticity vector ($\vec{\omega}$), or its scalar equivalent, the enstrophy (z), is another important quantity describing the energy cascade between these scales. Given in Eq. 4.12, enstrophy measures dissipation of energy due to rotational or vortical motions, and its prediction leads to identifying vortex structures and measuring momentum dissipation from rotation,

$$\begin{aligned} \vec{\omega} &= \bigtriangledown \times \vec{\xi} \\ z &= \frac{1}{2}(\vec{\omega}.\vec{\omega}). \end{aligned} \tag{4.12}$$

Figure 4.21 compares the time evolution of the total energy and enstrophy, achieved with different AIM resolutions, with DNS. By increasing the number of resolved modes, the AIM approximation becomes more accurate. For $k_m = 32,\ m/n_g = 0.0042$, the difference between total energy estimated by AIM and computed from DNS is negligible, but there is a discernible error in total enstrophy prediction. This behavior shows that the dissipation of energy is not captured accurately at the smallest scales.

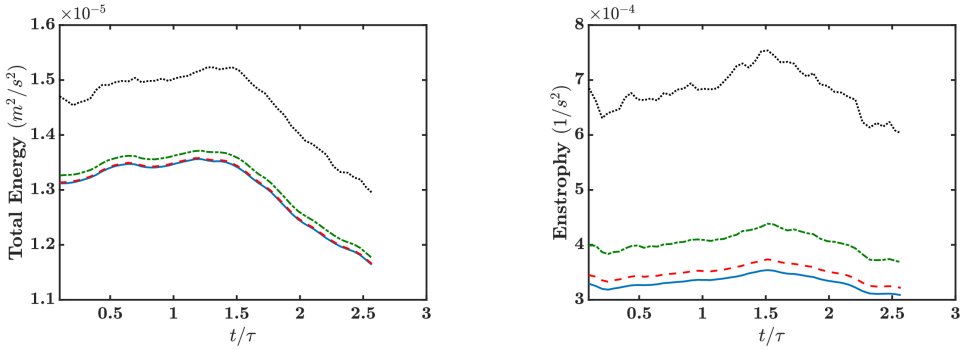

Figure 4.21: Effect of AIM resolution on recovery of total energy and enstrophy for $n_g = 256^3$. The highest resolution of AIM contains only 0.4 percent of DNS modes. DNS: —, AIM with $k_m = 16,\ m/n_g = 5.33 \times 10^{-4}$: ▪▪▪, AIM with $k_m = 24,\ m/n_g = 0.0018$: ·-·-, AIM with $k_m = 32,\ m/n_g = 0.0042$: - - -.

To further understand the method's ability to capture the spatial structure of the turbulent flow, the helicity field is also explored. Helicity is defined as the integral of the scalar product of the vorticity and velocity vectors, and is a measure of their alignment in the flow,

$$H = \int_V \vec{\xi} \cdot \vec{\omega} dV, \tag{4.13}$$

where the integral is over the computational domain. Helicity is related to nonlinear vortex stretching and impedes the cascade of energy between scales. While a higher helicity is associated with coherent and long-lasting structures, a lower helicity indicates higher dissipation at small scales. Helicity density is defined as the dot product of the velocity and vorticity vectors: $\bar{h} = \langle \vec{\xi} \cdot \vec{\omega} \rangle$. Helicity is the integral of helicity density over the considered volume. Here, helicity density is computed at different

AIM resolutions. Figure 4.22 shows that AIM with a sufficiently large dimension can capture helicity quite accurately. Helicity can also be studied as a dimensionless local quantity named relative helicity density [216],

$$h = \frac{\vec{\xi} \cdot \vec{\omega}}{|\vec{\xi}||\vec{\omega}|} = \cos(\theta), \tag{4.14}$$

which is defined as the cosine of the angle between velocity and vorticity vectors. In this definition, the instantaneous total velocity and vorticity fields are used. Regions with $h \approx \pm 1$ correspond to coherent large-scale structures. Previous studies suggest $\overline{h^2} = \overline{\cos^2\theta} \approx 0.333$ for a flat relative helicity density probability distribution function (PDF), where $\overline{h^2}$ is the average value of the PDF [216]. Larger or smaller values correspond to a greater or less helical behavior, respectively. Figure 4.22 (right) compares the fluctuating relative helicity density PDF approximated by AIM with DNS results. As shown, AIM modeling predicts more dissipative vortical motion and fewer sustained structures, both in the PDF distribution and in the average helicity density of the field.

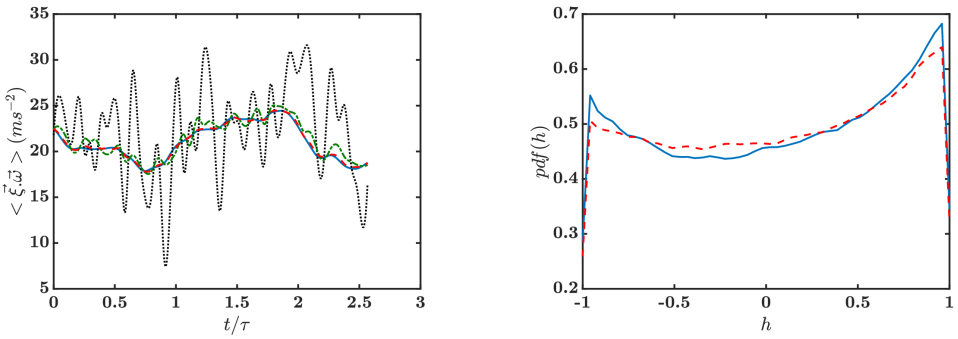

Figure 4.22: Prediction of helicity density by AIM. Left: convergence to DNS by increasing AIM resolution for $n_g = 256^3, 5.33 \times 10^{-4} < m/n_g < 0.0042$; DNS: —, AIM with $k_m = 16$: ▪▪▪, AIM with $k_m = 24$: ···, AIM with $k_m = 32$: - -. Right: The relative helicity density PDF for $n_g = 128^3, k_m = 16$. ($\overline{h^2}_{DNS} = 0.3639$, $\overline{h^2}_{AIM} = 0.3540$); DNS: —, AIM: - -.

Higher-order moments of velocity derivatives provide information about the small-

scale structure, including the transfer of energy between different scales and the inertial range. For this purpose, the derivative skewness is defined as

$$S = -\frac{\langle (\frac{\partial \xi_1}{\partial x_1})^3 \rangle}{\langle (\frac{\partial \xi_1}{\partial x_1})^2 \rangle^{3/2}}, \tag{4.15}$$

with ξ_1 as the velocity component in x-direction, and $\langle \cdot \rangle$ denotes spatial average. By this definition, derivative skewness is positive, and it is related to vortex stretching and energy cascade in the dissipation range. Prediction of such higher-order statistics of small-scale quantities is essential for rare events consideration [6]. Figure 4.23 shows that AIM with sufficiently large dimension can track exact derivative skewness with significant dimension reduction ($m/N = 0.03$). Since the small scales are important for such derivative quantities, these results show that AIM can recover a portion of this information (Fig. 4.23, right).

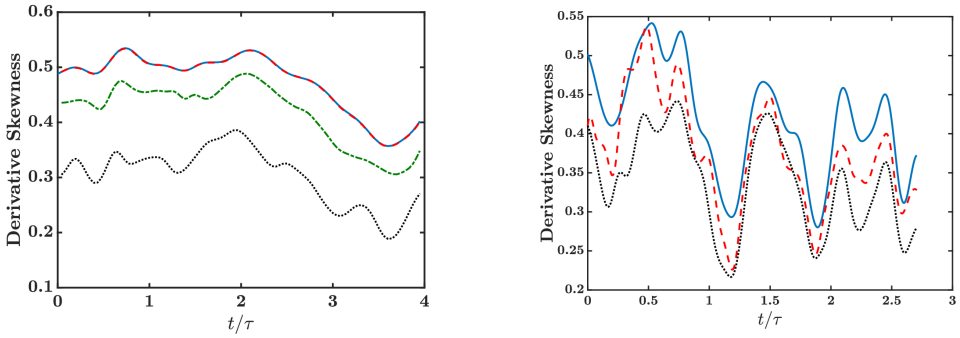

Figure 4.23: Prediction of velocity-derivative skewness by AIM. Left: convergence with resolution for $n_g = 128^3, 0.0018 < m/n_g < 0.0334$; DNS: —, AIM with $k_m = 12$: ..., AIM with $k_m = 16$: -·-, AIM with $k_m = 32$: - -. Right: comparison of AIM with filtered DNS velocity field for $n_g = 64^3, m/n_g = 0.0044$. DNS: —, AIM: - -, Projected DNS: -·-.

4.1.2.7 A priori comparison with other models

Here, the AIM approximation is compared against the Smagorinsky model [41] in the LES approach. As discussed in Sec. 2.1.2, LES approaches are dominated by implicitly filtered LES. To make the comparison meaningful, explicit filtering of LES

is considered here. Conventional LES SGS models represent the subfilter stress terms, which can be considered as a lower order projection of the small scale information. They do not reconstruct the subfilter field. Also, there has been other works in the past relating SGS modeling to AIM, albeit theoretically (see, for instance, [68]). Here a numerical test is done to compare the *a priori* AIM and one LES model. The deviatoric part of the subgrid-scale stress tensor (τ_{ij}) modeled by LES is compared with the exact SGS obtained from the DNS. To make the comparison fair, *a priori* LES model is conducted similar to such analysis in previous studies [83, 217, 218]. The constant-coefficient Smagorinsky model [41, 219] is defined as

$$\begin{aligned} \tau_{ij} &= -2\nu_T \bar{S}_{ij} \\ \nu_T &= (C_s\Delta)^2 (2\bar{S}_i j \bar{S}_{ij})^{1/2}, \end{aligned} \tag{4.16}$$

where $\nu_T(x,t)$ is the eddy viscosity, and $\bar{S}_{ij}$ is the resolved strain-rate tensor. The eddy viscosity is defined based on the constant C_s and the filter width Δ. In this study, $C_s = 0.2$ is chosen among various values tested for C_s. For *a priori* LES modeling, the filtered velocity field is obtained from the DNS data. A sharp spectral filter is used to project the DNS field onto the resolved field of LES. The exact SGS stress tensor is computed by Eq. 2.11. To compare AIM with the Smagorinsky model, SGS stress tensor is computed from Eq. 2.11 from the AIM-reconstructed field. The DNS calculation is done on a $n_g = 64^3$ grid, and the cut-off wavenumber for the AIM projection and sharp spectral filter is $k_c = 8$. The sharp spectral filter is chosen as the filtering operator to make the resolved (filtered) field identical for LES and AIM. The SGS stress tensor is recovered on a $N = 16^3$ grid. Figure 4.24 shows the τ_{12} obtained from the DNS data (left) and modeled by AIM (middle) and LES (right). Both AIM and LES models predict more dissipation compared to the DNS field. The Smagorinsky model has roughly captured some large features of the exact field, while the AIM prediction looks like an intensified DNS field. Figure 4.25 compares the

volume-averaged mean subgrid-scale stresses $< \tau_{ij} >$, which shows that both models are considerably different from the exact SGS stress.

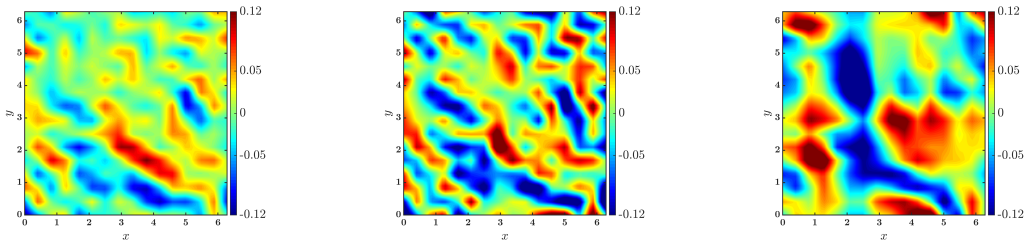

Figure 4.24: Subgrid scale shear stress, τ_{12} (m^2/s^2). Left: Exact SGS shear stress from DNS data, middle: SGS shear stress modeled by AIM, and right: SGS shear stress modeled by Smagorinsky model (Eq. 4.16).

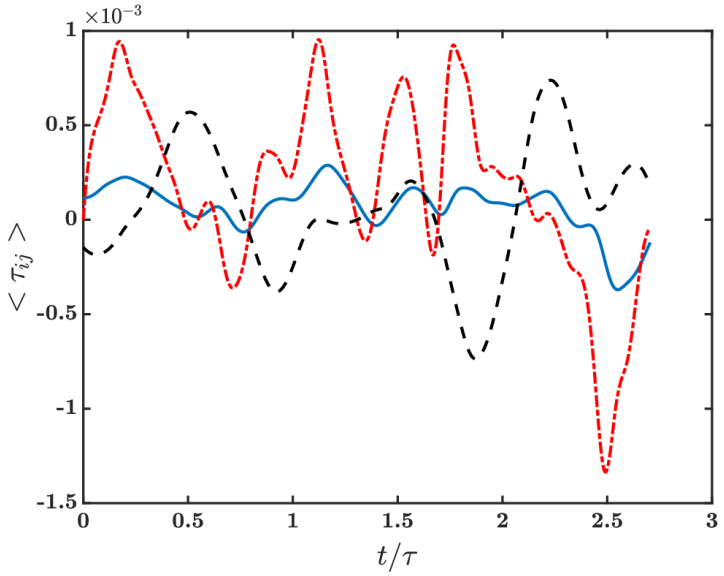

Figure 4.25: Volume averaged SGS stresses $< \tau_{ij} >$. DNS: —, AIM: ···, LES: - -.

4.2 A posteriori analysis of AIM for turbulent flows

In this section, the proposed reduced-order model is assessed *a posteriori* for the forecast of turbulent dynamics in the KSE and HIT over a range of parameters relevant to the dimension of the attractor. By tracking the dynamics of the system in a lower-dimensional space, convergence of the AIM model to the full-dimensional

solution is shown for the KSE which possesses an IM. A computationally efficient framework of AIM is investigated for HIT because it is a more realistic problem of interest. The proposed model is assessed in the forecast of the long-term statistics, dynamics of spatial statistics, and small scales contribution to the resolved subspace. Finally, the reduced-order model performance is compared against other prevalent turbulence models.

4.2.1 The Kuramoto-Sivashinsky equation

The goal is to evolve dynamics of the resolved subspace alone. Equation 4.4 can be written as

$$\frac{u_k^{n+1}-u_k^n}{\Delta t}+(\mu q_k^4-q_k^2)u_k^n+\frac{iq_k}{2}\boldsymbol{P}\Bigg(\sum_{\substack{1\le|l|\le n_F/2\\ 1\le|k-l|\le n_F/2}}(\boldsymbol{u}^n,\boldsymbol{w}^n)_l(\boldsymbol{u}^n,\boldsymbol{w}^n)_{k-l}\Bigg)=0, \tag{4.17}$$

where n is time step iteration and $\boldsymbol{w}^n$ is approximated by Eq. 4.6 using $\boldsymbol{u}^n$. Initial condition of Eq. 4.17 is the projected initial condition of DNS simulations ($\boldsymbol{P}g(x)$). Similar to the full-dimensional simulation, the exponential time difference fourth order Runge-Kutta method (ETDRK4) [206, 207] with standard 3/2 de-aliasing is implemented for the reduced-order modeling.

4.2.1.1 Stability and AIM convergence

The KSE exhibits spatiotemporal chaos, where infinitesimal perturbations can lead to exponential energy accumulation. The quadratic nonlinear term transports energy from the low linearly unstable modes to the high modes with rapid exponential decay. Therefore, insufficient spatial resolution cannot capture energy dissipation and leads to numerical instability. Table 4.1 shows the required minimum resolution (N_{min}), for the stability of the solution as well as the maximum resolution (N_{DNS}) used in

the high fidelity solution of this study. The objective of the proposed reduced-order model is to evolve the dynamics of the system on an AIM spanned by $m \ll N_{min}$.

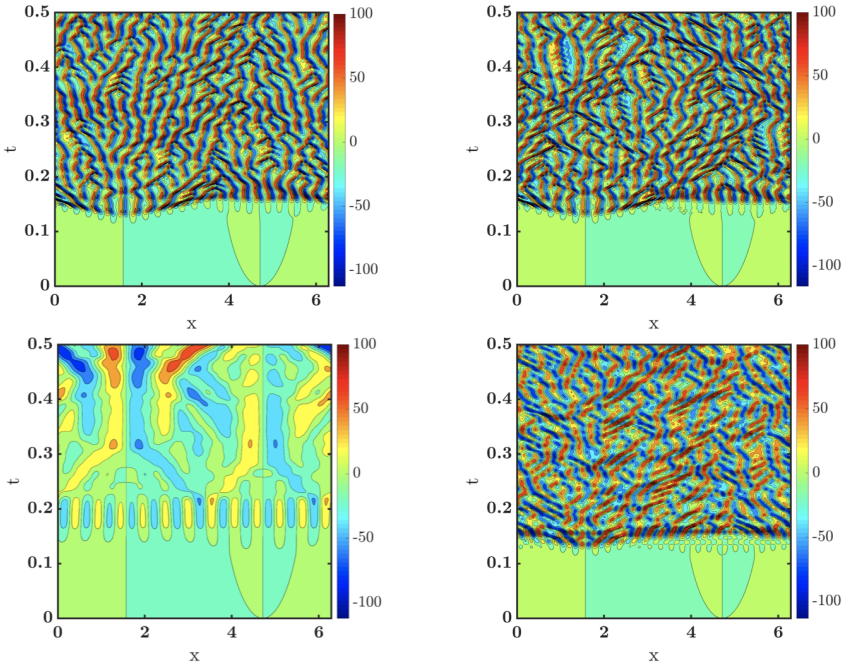

Figure 4.26: Solution of the KSE, $\xi(x,t)$, for Re = 158.11. Top left: DNS with $N_{DNS} = 2048$, top right: AIM with $m = 256$, bottom left: AIM with $m = 64$, bottom right: AIM with $m = 128$. Only part of the computational domain is shown.

Figure 4.26 shows convergence of AIM prediction for Re = 158.11 with $64 \leq m \leq 256$. It can be observed that at $t > 0.15$, the dynamics enter the chaotic regime, where a truncated system with 512 Fourier modes for the same Reynolds number becomes unstable and blows up. Including the AIM subgrid model in the evolution of the resolved modes stabilizes the solution and predicts transition to turbulence. The lowest dimensional AIM cannot capture the transition to chaotic dynamics, and it only retains the large-scale structures of the laminar region. However, at this resolution AIM dimension is much lower than the minimum resolution required for stability. By increasing the AIM dimension, the prediction is improved considerably, and a 256-dimensional AIM captures most of the dynamics in the chaotic region.

The accuracy of the model prediction depends on the size of the AIM, m, and the

accuracy of the approximation of the unresolved dynamics. The KSE is known to have a relatively low-dimensional inertial manifold which scales as Re [174, 183]. Here, the model accuracy is assessed for a range of resolutions m, and Fig. 4.27 shows the root mean square of the error between AIM prediction and the full-dimensional system solution in physical space computed in the chaotic regime ($t > 0.15$), over a range of Re numbers and AIM dimensions. The AIM resolution is normalized by the integer part of the Reynolds number [Re], which is the number of linearly unstable modes. The AIM prediction converges uniformly to the exact solution when the approximate IM is large enough to contain all of the unstable dynamics. These results suggest that strong convergence properties can be obtained for resolutions exceeding this point, which is in agreement with prior works [174, 183].

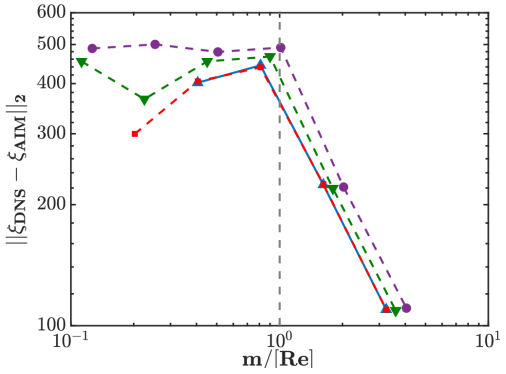

Figure 4.27: L_2-norm of the spatiotemporal error of AIM prediction in physical space; Re = 158.11: ▲, Re = 316.23: ■, Re = 569.21: ▼, Re = 1011.93: ●. Vertical dashed line marks m = [Re].

4.2.1.2 Prediction of statistical properties

In the AIM model, the ground assumption is that the unresolved variables respond instantly to the resolved dynamics, i.e. $d\boldsymbol{w}/dt = 0$. The validity of this assumption and the rate of convergence to the fixed-point solution of Eq. 4.6 has been assessed in Sec. 4.1. The optimum number of iterations depends on the Re number and the resolution of AIM, m. Seeking the fixed-point solution can be computationally

expensive, and its feasibility should be judged based on the improved accuracy of the resolved dynamics prediction. Figure 4.28 (left) shows the energy spectrum of Fourier modes in the resolved and unresolved subspaces. The modeled resolved spectrum generally follows the DNS spectrum, but there are discrepancies at the largest resolved scales. The reconstructed unresolved spectrum can be improved by implementing more iterations in Eq. 4.6. The first-order approximation ($j = 1$) considers only the nonlinear interaction between the resolved scales for the transfer of energy to the unresolved scales. This approximation is improved by seeking the fixed-point solution of Eq. 4.6 with more iterations to reconstruct the unresolved modes. However, unlike the unresolved dynamics, this higher-order approximation does not improve the resolved dynamics spectrum significantly. To assess this higher-order approximation more precisely, the probability density function of the resolved modes is compared for different numbers of iterations (j), in Eq. 4.6. Figure 4.28 (right) compares the PDF of real part of Fourier mode at the cut-off wavenumber for Re = 158.11 and $m = 256$ predicted by AIM and DNS. It is shown that a higher-order approximation of the unresolved dynamics gives a better prediction of the resolved scales throughout the distribution.

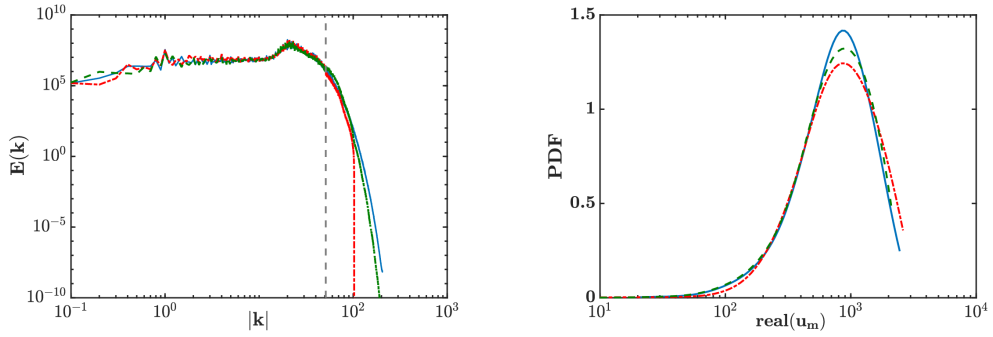

Figure 4.28: Left: Energy spectrum of the KSE at $Re = 316.23$. DNS: —, AIM with $m = 512$ and $j = 1$ in Eq.4.6: ···, AIM with $m = 512$ and $j = 4$ in Eq.4.6: —. Right: PDF of real part of u_m predicted by AIM and DNS at $Re = 158.11$, $m = 256$; DNS: —, AIM with $j = 1$ in Eq. 4.6: ···, AIM with $j = 3$ in Eq. 4.6: - -.

4.2.2 Homogeneous isotropic turbulence

Following the construction of an AIM for the Navier-Stokes equations in Sec. 4.1.2.2, dynamics of the HIT can be tracked on the inertial manifold by evolving only the resolved variables,

$$\frac{u_i^{n+1} - u_i^n}{\Delta t}(\vec{k}, t) + \mu|k|^2 u_i^n(\vec{k}, t) - B u_i^n(\vec{k}, t) + \mathcal{R}(\boldsymbol{u}^n, \boldsymbol{w}^n) = 0, \tag{4.18}$$

where $\boldsymbol{w}^n$ is obtained from Eq. 4.9 using $\boldsymbol{u}^n$. With this approximation of the unresolved dynamics, the governing equations of the resolved dynamics (Eq. 4.18) is closed and can be evolved in time independently.

Before any spatial discretization, the unresolved subspace is infinite-dimensional. After spatial discretization, the unresolved subspace is the subspace between approximated IM and the entire state space. To develop a low-dimensional AIM, the unresolved subspace becomes considerably higher dimensional such that solving Eq. 4.9 can be adversely expensive in terms of cost and memory. This limitation can be lifted by considering only part of the unresolved dynamics that resides in a close neighborhood of the resolved subspace. Such simplification is in agreement with the exponential tracking property of dissipative dynamical systems [172], and the lower grid resolution reduces the computational and memory cost of the approach. By removing the exponentially decaying dynamics, the stiffness of the problem reduces and a larger time step can be used.

Unlike the KSE, the rate of convergence in Eq.4.9 is slower than quadratic, and more iterations are needed to approximate higher modes in the unresolved subspace which can make the AIM approach inefficient (Sec. 4.1.2.5). Removing the smallest unresolved scales from the computational grid makes the AIM approach more efficient in two ways: 1) by reducing the size of the domain, the cost of computing the nonlinear term $\mathcal{R}(\boldsymbol{u}, \boldsymbol{w})$, decreases; 2) higher-order approximations of Eq. 4.9 are required to

reconstruct smaller unresolved scales, which can be avoided. Therefore, the unresolved subspace can be decomposed into unresolved but represented scales approximated by Eq. 4.9 and unresolved and unrepresented scales with wavenumbers larger than the Nyquist wavenumber (k_{n_g}) of the computational grid. The decomposition of the computational domain is shown in Fig. 4.29. AIM dimension refers to m which determines the degrees of freedom of the resolved subspace, and AIM resolution is n_g of AIM simulation including both resolved and represented unresolved subspaces. The effect of the unresolved and unrepresented scales on the dynamics of the system needs to be modeled.

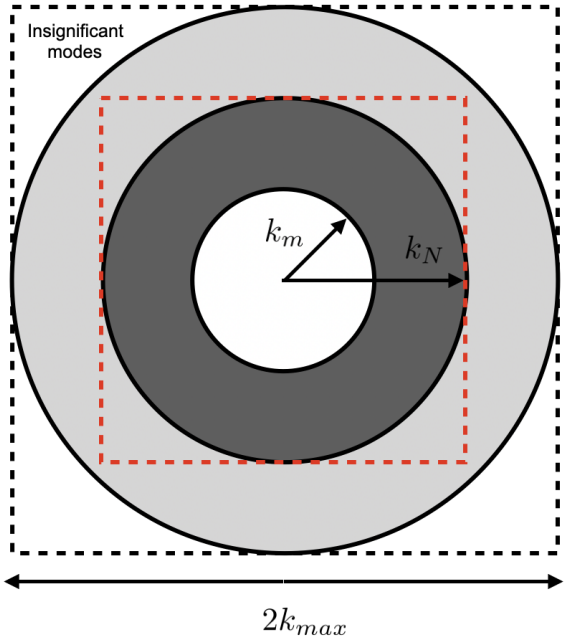

Figure 4.29: Representation of the resolved and unresolved subspaces in wavenumber space. Circle with radius k_m encloses the resolved modes. Light gray shaded area denotes the unresolved and unrepresented modes, and dark gray area represents unresolved but represented modes. k_{max} is the highest wavenumber in DNS calculations, and k_N is the highest wavenumber in AIM-ROM calculations. Dashed red rectangle is computational domain of AIM-ROM.

The *a priori* analysis has demonstrated that approximating only the larger unresolved scales reconstructs the interaction between resolved and unresolved dy-

namics sufficiently. However, it cannot provide adequate dissipation in the system (Sec. 4.1.2.6). Adding a dissipative modeling component similar to the eddy-viscosity approach can address this shortcoming.

4.2.2.1 A modified approximate inertial manifold

As discussed in Chap. II, most eddy-viscosity subfilter models in LES assume that the SGS contribution to the filtered field is dissipative and thus cannot predict the transfer of energy to the large scales (backscatter). An improvement has been made by adding additional non-dissipative terms to these models such as in the mixed model and the scale-similarity model [68, 83]. Dynamic subfilter modeling can also account for backscatter in transitional flows if locally negative eddy-viscosity is allowed [61]. On the contrary, AIM recovers the nonlinear interaction between the resolved and unresolved scales by reconstructing the subfilter field without assuming a forward cascade of energy. The recovered unresolved energy spectrum which is mostly dominated in a neighborhood of the resolved subspace (Sec. 4.1.2.5), can be used to determine the rate of backward/forward transfer of energy between the resolved and unresolved subsets. The energy stored in the unresolved scales either transfers backward to the resolved scales or transfers forward to the smaller unresolved scales where it finally gets dissipated by molecular viscosity. If only part of the unresolved modes is represented in the unresolved subspace, the portion of their energy that is not supposed to backscatter should be drained from the system. Therefore, energy virtually transferred to the unresolved and unrepresented scales needs to be dissipated. First, the AIM approximation is studied to determine whether backward/forward energy transfer is captured accurately.

The subgrid-scale dissipation, ϵ_{SGS} is defined as

$$\epsilon_{SGS} = \tau_{ij}\overline{S}_{ij}, \tag{4.19}$$

where $\tau_{ij} = \overline{u_i u_j} - \overline{u_i}\ \overline{u_j}$ is the SGS stress, and $\overline{S}_{ij} = \left(\frac{\partial u_i}{\partial x_j} + \frac{\partial u_j}{\partial x_i}\right)$ is the resolved-scales strain rate. When the unresolved scales remove energy from the resolved ones (forward scatter), ϵ_{SGS} is negative; and if SGS transports energy to the resolved scales (backscatter), SGS dissipation is positive. Therefore, forward and backward energy transfer can be defined as [60]

$$\begin{aligned} \epsilon_- &= 0.5\big(\epsilon_{SGS} - |\epsilon_{SGS}|\big) \\ \epsilon_+ &= 0.5\big(\epsilon_{SGS} + |\epsilon_{SGS}|\big). \end{aligned} \tag{4.20}$$

The forward energy scatter will eventually dissipate at the smallest scales. If the smallest unresolved scales are discarded, this energy needs to be removed to avoid energy accumulation beyond the decomposition wavenumber. Reconstructed energy spectrum can provide the rate of energy dissipation at the unresolved scales. A dynamic spatially varying viscosity can be determined to dissipate the forward cascade of energy beyond the cut-off wavenumber

$$|\hat{\epsilon}_-| = 2\mu_T(k)|k|^2 E(k), \tag{4.21}$$

where $\hat{\epsilon}_-$ is the Fourier transform of forwarding cascade of energy. With this turbulent viscosity, the effective viscosity at the unresolved scales is: $\mu_{eff} = \mu + \mu_T$, and the unresolved dynamics are approximated by

$$\boldsymbol{w}_{\vec{k}}^{j+1} = -(\mu_{eff}^{j}|k|^2)^{-1}\boldsymbol{Q}\mathcal{R}(\boldsymbol{u}, \boldsymbol{w}^j)_{\vec{k}}. \tag{4.22}$$

It should be noted that μ_{eff} changes at each iteration. For $j = 1$, $\mu_{eff} = \mu$ because the unresolved subspace is not reconstructed yet. By implementing more iterations, the modified viscosity is updated with the reconstructed unresolved scales.

Backward and forward scatter of energy occur at all scales, and turbulent viscosity

obtained from Eq. 4.21 can be defined at both resolved and unresolved scales. Three different approaches have been considered: 1) modifying viscosity only at the resolved subspace, 2) modifying viscosity at both resolved and unresolved subspaces, and 3) modifying viscosity only at the unresolved subspace. Here, the effective viscosity is modified only at the represented unresolved scales, as the forward energy transfer from resolved scales will eventually dissipate at the unresolved scales. Besides, modifying the effective viscosity at the unresolved scales improves the inertial manifold theory requirements by increasing the spectral gap of the linear operator of the Navier-Stokes equations. As unresolved scales become more dissipative, the separation of scales between resolved and unresolved scales is more prominent. In turn, the assumption that unresolved scales equilibrate to the AIM dynamics is more justified.

4.2.2.2 Numerical tests

For this *a posteriori* study, a different set of HIT cases are considered for two reasons. First, higher resolutions of HIT at higher Re numbers are considered to allow the investigation of AIM at higher-dimensional systems. Second, the forcing of the velocity field has been limited to the large energy-containing scales. Since part of the unresolved scales are removed, a uniform forcing at all scales would not have been reasonable for model comparison. Statistics of turbulence are independent of forcing scheme [220], and previous studies have shown dimension of the attractor of the system is also independent of forcing scheme [213].

Direct numerical simulations of HIT of two spatial resolutions are used to investigate the accuracy of the AIM prediction. Table 4.3 shows the numerical setup for DNS cases. The Taylor microscale Reynolds number Re_λ and the Kolmogorov length scale η (Δx is grid spacing in each direction), are monitored over the initialization time to make sure the turbulent field is fully developed and resolved. Only Fourier modes with $|\vec{k}| \leq k_f$ are being forced, and the flow statistics are monitored for several

eddy turnover times (τ) to ensure the forcing method does not lead to instability and energy pile-up at small scales.

Grid Resolution (n_g)	μ	Re_λ	$\eta/\Delta x$	B	k_f	D_{KY}
256^3	0.05	91.54	0.55	5	8	6.9257×10^4
512^3	0.01	290.27	0.23	8	8	6.4165×10^6

Table 4.3: Numerical setup for HIT

Current theories cannot prove the existence of an inertial manifold for the Navier-Stokes equations [98]. However, in systems dominated by coherent structures, the dynamics of the system are confined to a low-dimensional attractor. Direct estimations of this attractor dimension for turbulent flows using the Kaplan-Yorke conjecture [99] showed that attractor dimensions are orders of magnitude lower than the number of degrees of freedom required by DNS [34, 100], and for forced HIT, it is shown that the attractor dimension scales with $\left(\frac{L}{\eta}\right)^{2.8}$ [100] where L is the domain length. For the turbulent fields considered here, this estimated attractor dimension (D_{KY}) is used as a reference for the assessment of AIM accuracy over a range of AIM dimensions. It should be mentioned that when an inertial manifold exists, it contains the attractor of the system. Hence, an AIM should be larger than the attractor of the system regardless of the existence of an inertial manifold.

To evaluate the proposed AIM model against common turbulence modeling approaches in terms of accuracy and efficiency, large-eddy simulations with constant and dynamic Smagorinsky subfilter models [41] have been conducted. To make resolved subsets of LES and AIM similar, a sharp spectral filter is used for LES. However, the resulted variable separations are not identical. The resolved subspace of AIM in the wavenumber space is a sphere with radius k_m, while the same cut-off wavenumber in LES resolves all the wavenumbers enclosed in a cube of side length $2k_m$. Following the conventional LES practices, the subfilter field representation is implicit such that the subfilter scales are not represented on the computational grid, and their contribution

is modeled by the Smagorinsky eddy viscosity model. On the other hand, AIM reconstructs the subfilter field either entirely or just a subspace of it. Therefore, for the same cut-off wavenumber, the computational grid of AIM is larger because it contains the unresolved but represented scales.

4.2.2.3 Prediction of backward/forward energy transfer

First, AIM prediction (Eq. 4.9) has been examined to see if the reconstructed turbulent field captures forward and backward scatter of energy between resolved and unresolved scales accurately. Figure 4.30 shows the rate of energy transfer over the range of scales for 256^3 field with $k_m = 16$. As expected, subgrid-scale energy transfer is dominated closer to the cut-off wavenumber and at larger unresolved scales. This behavior confirms that there is no need to recover all of the unresolved subspace, and approximating only the largest unresolved scales is sufficient to capture subgrid-scale effects on resolved dynamics. It can be seen that AIM captures energy transfer towards both the larger and the smaller scales. However, it overestimates the backward scatter at the unresolved scales. This is due to the limited approximation of the unresolved scales, and by implementing more iterations in Eq. 4.9 and recovering smaller unresolved scales, this approximation improves.

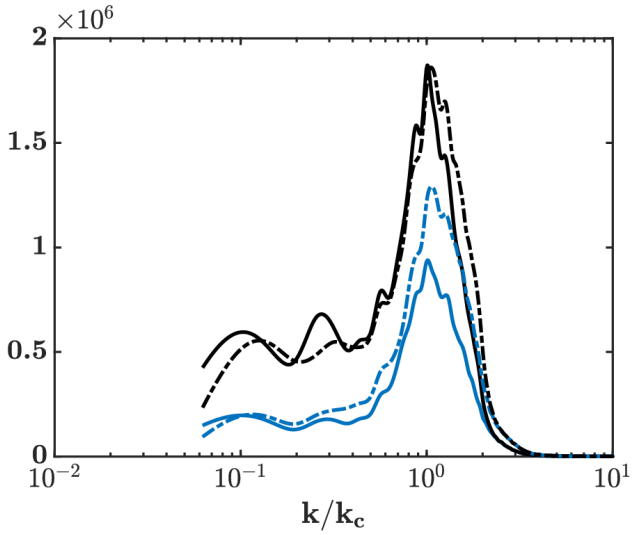

Figure 4.30: Spectrum of backward (—) and forward (—) SGS dissipation rate for $n_g = 256^3$ and $k_m = 16$. DNS: solid lines, AIM: dashed lines.

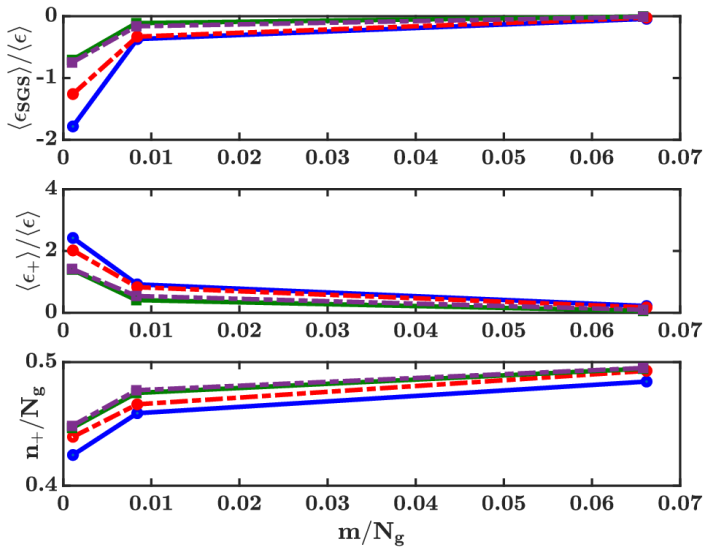

Figure 4.31: Top: subgrid-scale dissipation, middle: SGS backscatter. Both values are normalized by total resolved dissipation. Bottom: fraction of points with backscatter of the energy in the computational domain. DNS of 256^3: —●—, AIM-ROM for 256^3: ··●··. DNS of 512^3: —■—, AIM-ROM for 512^3: ··■··. Horizontal axis is resolved subspace dimension normalized by the full-dimensional system dimension (m/n_g).

Statistics describing the energy transfer between resolved and unresolved subspaces are provided in Fig. 4.31 where the (SGS) dissipation (top) and energy backscatter of

the subfilter field (middle) as a function of the normalized AIM dimension (m/n_g) are shown. Here, the SGS dissipation and backscatter of energy to the resolved scales are computed from turbulence fields modeled by the AIM over a range of dimensions, m. Also, DNS fields are filtered, and the exact values of these quantities are computed at different filtering widths for comparison with AIM. At each cut-off wavenumber, the SGS dissipation ($\langle\epsilon_{SGS}\rangle$), and the energy backscatter ($\langle\epsilon_{+}\rangle$) are normalized by the total resolved dissipation ($\langle\epsilon\rangle$). It can be seen that by increasing the filter width, i.e. by using a lower AIM resolution, the amount of SGS dissipation increases. Accordingly, the amount of backscatter of energy to the resolved scales increases, because the cut-off wavenumber is farther away from the rapidly dissipative scales, and a larger part of the inertial range is in the unresolved subspace. The number of points in the physical domain experiencing energy backscatter is almost independent of the cut-off wavenumber (Fig. 4.31, bottom), which shows that even when the amount of energy backscatter is not considerable compared to the total dissipation, subgrid energy backscatter occurs between the smallest scales at the dissipation range. AIM predicts the same characteristics, but more points in the field experience backscatter. This is not surprising as AIM models nonlinear interaction between the scales but does not have a completely dissipative component. Overall, these results show that AIM can capture energy transfer between resolved and unresolved subspaces accurately, and this property can be used to implement a dynamic dissipative component to account for the unresolved and unrepresented scales (Eq. 4.22).

4.2.2.4 Prediction of turbulent statistics

Turbulent statistics predicted by the original and modified AIM models are compared against the DNS calculations in Fig. 4.32, where turbulent kinetic energy is computed based on the resolved field and total dissipation rate is computed based on the effective viscosity in each of the modeling approaches including LES. It can be observed that

AIM approximation alone cannot predict enough dissipation in the system, but adding a dissipative component solves this problem, and dissipation is almost accurately predicted by the modified AIM model. This improvement in AIM prediction is not dominant in the turbulent kinetic energy as the modified viscosity removes energy only from the unresolved scales. These statistics show that AIM models outperform the dynamic Smagorinsky approach, however, here all of the unresolved subspace is approximated by AIM with only two iterations in Eqs. 4.9 and 4.22, and decomposing the unresolved subspace into represented and unrepresented components provide a closer comparison to LES.

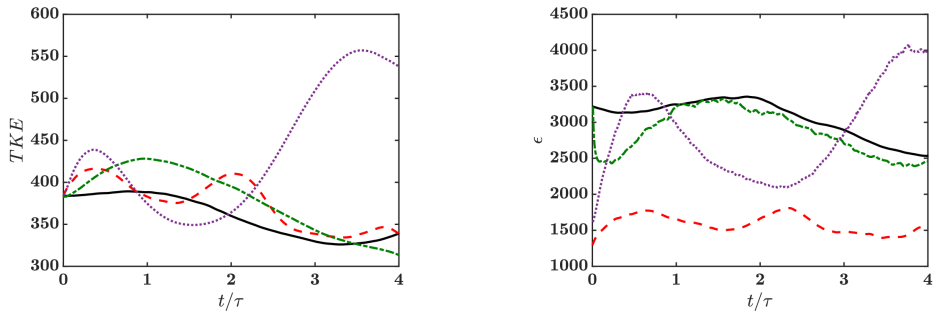

Figure 4.32: Time evolution of resolved turbulent kinetic energy (left) and dissipation rate (right) of 256^3 field with $k_m = 16$. DNS: —, AIM: - -, modified AIM: -·-, LES with dynamic Smagorinsky model: . . . .

To assess the modified AIM approach in modeling the effect of unresolved and unrepresented scales, only part of the unresolved subspace is kept in the computational domain and approximated by AIM. Figure 4.33 shows the statistics for the 256^3 field and $k_m = 16$ where the unresolved subspace dimension in AIM is reduced by discarding higher wavenumbers and using a lower grid resolution. While reducing the unresolved subspace dimension does not affect the turbulent kinetic energy of the resolved subspace substantially, it underestimates total dissipation in the system considerably. This behavior is predictable as in the lowest dimensional unresolved subspace ($n_g = 64^3$ for $k_m = 16$) the largest unresolved wavenumber reconstructed by AIM is 30.2 and $k/k_m < 2$ in Fig. 4.30, which shows a considerable amount of

forward scatter of energy is discarded. In this case, the dimension of AIM, m, is only 0.75 of the estimated dimension of the system's attractor (D_{KY} in Tab. 4.3). By increasing the AIM resolution, approximation of the unresolved dynamics and AIM prediction improve considerably. Considering approximate inertial manifolds for the 512^3 case with two different dimensions obtained from $k_m = 64$ and $k_m = 128$ results in $m/D_{KY} \approx 0.5$ and $m/D_{KY} \approx 4$. Figure 4.34 compares the time evolution of turbulent kinetic energy and dissipation rate predicted by AIM against the DNS data. By increasing the AIM dimension, both approximations have improved especially earlier in the prediction time.

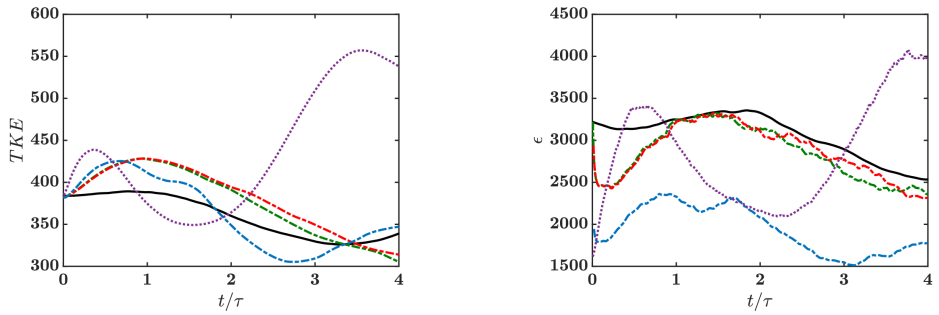

Figure 4.33: Time evolution of resolved turbulent kinetic energy (left) and dissipation rate (right) of 256^3 field with $k_m = 16$. DNS: —, modified AIM with $n_g = 256^3$: ···, modified AIM with $n_g = 128^3$: -·-, modified AIM with $n_g = 64^3$: - - -, LES with dynamic Smagorinsky model: . . . .

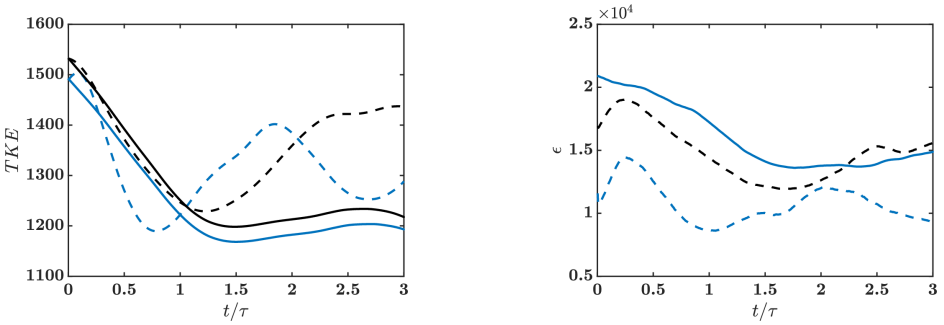

Figure 4.34: Time evolution of resolved turbulent kinetic energy (left) and total dissipation rate (right) of 512^3 field with $k_m = 64$ (blue lines) and $k_m = 128$ (black lines). Solid lines are obtained from DNS, and dashed lines are predicted by modified AIM model. Since total dissipation does not depend on k_m, only one line is shown here in dissipation evolution (right).

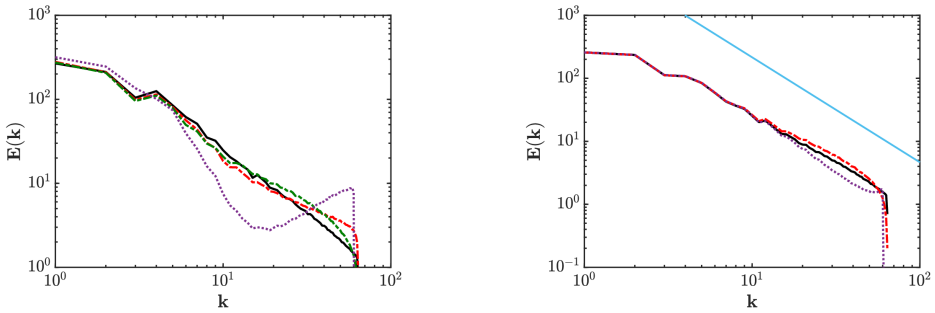

Figure 4.35: Left: resolved kinetic energy spectrum of forced 512^3 field for $k_m = 64$; DNS: —, AIM: -·-, modified AIM: -·-, LES with dynamic Smagorinsky model: . . . Right: resolved kinetic energy spectrum of decaying 512^3 field for $k_m = 64$. DNS: —, modified AIM: -·-, LES with dynamic Smagorinsky model: . . .

Resolved energy spectrum of the 512^3 field predicted by DNS, AIM and LES models for projection wavenumber $k_m = 64$ is compared in Fig. 4.35 (left). At this resolution, the AIM dimension m is almost half of the estimated dimension of the system's attractor (D_{KY} in Tab. 4.3). However, the energy spectrum is captured quite accurately by AIM except for the smallest resolved scales which their energy is overestimated. This issue has been alleviated in the modified AIM model. The spectrum predicted by the dynamic Smagorinsky model is quite different from the exact spectrum which can be due to the limited forcing of the large scales. The

dynamic Smagorinsky approach relies on the scale-similarity between larger resolved scales, smaller resolved scales and unresolved scales. Limited forcing at the larger resolved scales can falsely impose a higher rate of energy transfer at the smaller scales and lead to overshooting of energy at the smallest resolved scales. To test this explanation, the same initial condition for the 512^3 field in Tab. 4.3 is used for decaying HIT where there is no force. Figure 4.35 (right) shows the energy spectrum predicted by DNS, modified AIM and LES at $t/\tau \approx 1$, and it can be seen that the LES spectrum follows the exact spectrum even though it is more dissipative at the smallest resolved scales.

Finally, contours of the velocity field predicted by DNS, modified AIM, and LES models are compared in Fig. 4.36. Here, the decaying 512^3 field has been chosen for comparison since it allows for a fixed time step and comparison of various models at one instant where $t/\tau_0 \approx 1$. Both modeled fields look quite similar to the DNS field, but it can be seen that AIM preserves more details of the smaller structures. It should be mentioned that in decaying HIT, as turbulent energy dissipates, the size of the attractor changes and shrinks. Hence the approximation of AIM becomes more accurate for longer prediction times.

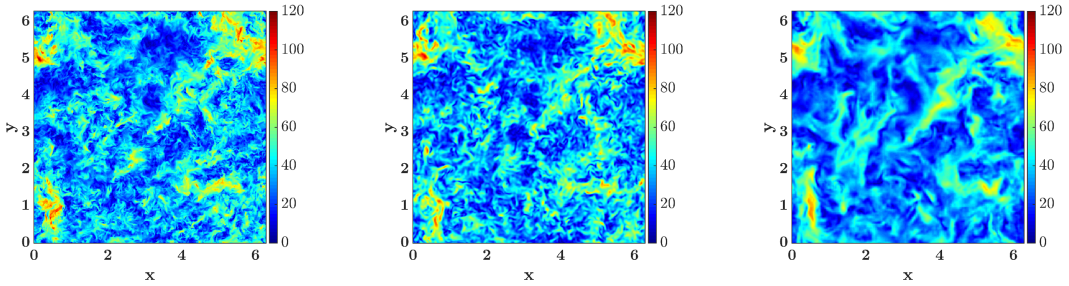

Figure 4.36: Magnitude of the velocity vector in a plane of the computational domain for decaying 512^3 field, left: DNS, middle: modified AIM with $k_m = 64$ and $m/D_{KY} \approx 0.5$, and right: LES with $n_g = 128^3$. LES field is interpolated into a higher resolution for demonstration purposes.

Computational cost of AIM and LES models are compared over a range of cut-off wavenumbers in Fig. 4.37, where computational costs of AIM and LES models are

normalized by the cost of the corresponding DNS. The comparison is based on the reduced grid resolution of the models (N/N_g), where N is the grid resolution of AIM or LES simulations, and N_g is the grid resolution of the corresponding DNS. It is shown that AIM is more expensive than the constant Smagorinsky model, but it is more efficient compared to the dynamic LES modeling. It should be mentioned that for the same grid resolution of AIM and LES, the resolved space in AIM is lower-dimensional, and it is not possible to compare computational cost of these models at the same accuracy.

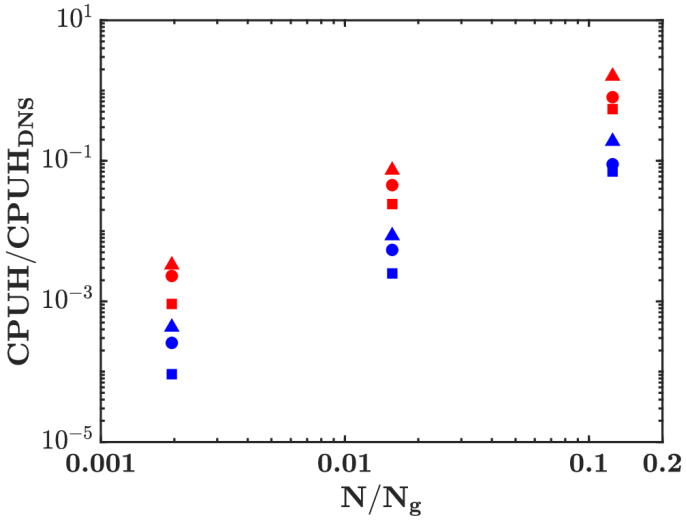

Figure 4.37: Reduced computational cost of DNS of $N_g = 256^3$ with AIM: ●, dynamic Smagorinsky: ▲, and constant Smagorinsky: ■ models. Reduced cost of DNS of $N_g = 512^3$ with AIM: ●, dynamic Smagorinsky: ▲, and constant Smagorinsky: ■ models.

4.3 Summary

The reduced-order model of turbulent flows developed in Chap. III based on the inertial manifold theory is investigated in this chapter. The proposed model has been examined on two canonical flows: one-dimensional Kuramoto-Sivashinsky equation and homogeneous isotropic turbulence governed by three-dimensional Navier-Stokes equations. First, an *a priori* analysis of the AIM approximation is conducted for both

systems.

The proposed AIM approximation is examined using a wide range of parameters in terms of the number of resolved scales (the dimension of the AIM) and the Reynolds or bifurcation numbers (directly proportional to the dimension of the attractor). In all configurations, for a sufficiently large dimension of the AIM, the dynamics of the unresolved variables are captured quite accurately. For the KSE, the statistics of the unresolved scales in the neighborhood of the inertial manifold are captured more accurately than the smaller scales farther away from the approximated IM. Smaller scales in the unresolved dynamics are less responsive to the dynamics of the IM, and there is a time delay in their response. Similar behavior was observed for the HIT case. A higher-order estimation of the unresolved dynamics, where the interactions between the resolved and unresolved dynamics are included, improves the AIM estimation of the unresolved dynamics.

In the *a posteriori* study, dynamics of the system are tracked in a lower-dimensional manifold determined in-situ without invoking ad-hoc assumptions about underlying statistics of turbulence. The approximate inertial manifold model has been studied over a range of parameters such as the AIM dimension, the size of the attractor, and the recoverable unresolved subspace dimension. The KSE is known to possess a low-dimensional inertial manifold, and convergence properties of the proposed AIM are following the estimated dimension of this manifold. HIT sets more challenges since the existence of an IM is still under question for three-dimensional Navier-Stokes equations. However, it has been shown that AIM with dimensions smaller than the estimated size of the attractor can capture the dynamics of the system quite accurately. Finally, AIM performance and cost have been compared with the dynamic Smagorinsky model in LES. It is shown that AIM outperforms LES in predicting statistical properties of turbulence and reconstructing features of the field, while its computational overhead is comparable.

CHAPTER V

AIM-Based Combustion Modeling

Discussion of combustion models in Sec. 2.2 revealed that developing models that circumvent the need for external manifold development would be a significant advance in ensuring the predictive accuracy of efficient combustion models. In this chapter, a different manifold-based approach is used, which utilizes the notion of inertial manifolds. Based on this concept, an analysis of the use of IM theories for modeling turbulent reacting flows is conducted. Here, an approximate inertial manifold is utilized, where the flow is decomposed into resolved and unresolved scales similar to conventional LES filtering. However, unlike in conventional LES, the small scales are directly reconstructed through a steady-state assumption. In Chap. IV, this approach has been tested for non-reacting turbulent flows. Here, AIM is extended to turbulent flames. The AIM approach combines adaptive deconvolution principles with state-space decomposition such as intrinsic low-dimensional manifold (ILDM) [122] or computational singular perturbation (CSP) [125]. The main advantage of the IM-based approach is that the manifold can be identified using the linear part of the governing equations, namely the viscous or diffusion operators, rather than by the eigendecomposition of the Jacobian matrix. Additionally, unlike the flamelet-type approaches where the manifold is constructed *a priori*, the AIM approach will extract this manifold *in-situ*. As a result, additional sub-filter closures for scalar dissipation

or mixing time scales are not needed.

This chapter focuses on exploring the validity and accuracy of the inertial manifold theory for canonical turbulent flames. Compared to the previous analysis on chaotic flows, this problem challenges the AIM approximation in different ways. The non-linear chemical source term lacks the scale separation property of the convection term, and the thermochemical properties of the chemistry field affect the level of local flame strength causing extinction or reignition, which implies strong interaction between turbulence and chemistry.

5.1 Problem configuration and numerical approach

Turbulent combustion developing in homogeneous isotropic turbulence is used to assess the AIM approach. The one-step chemical global reaction is used to emulate combustion while neglecting density variations. The reaction rate parameters are obtained from prior work [221], which has been previously used to study unsteady flamelet modeling [222]. This flow configuration is solved using a pseudo-spectral approach, with the full resolution of the length and time scales providing the DNS solution. Additionally, the AIM-based simulations with reduced degrees of freedom, as well as a truncated simulation with the same degrees of freedom as the AIM but with no additional modeling, are conducted. The governing equations include transport equations for the three velocity components, mixture fraction, and progress variable. The velocity field is considered to be incompressible, leading to the following set of equations,

$$\begin{aligned} &\frac{\partial \xi_i}{\partial t} + \xi_j \frac{\partial \xi_i}{\partial x_j} = -\frac{1}{\rho}\frac{\partial p}{\partial x_i} + \nu \frac{\partial}{\partial x_j}\left(\frac{\partial \xi_i}{\partial x_j}\right) + B\xi_i, \\ &\frac{\partial \xi_i}{\partial x_i} = 0, \end{aligned} \tag{5.1}$$

where ξ_i is the velocity component in the i^{th} direction, p is the hydrodynamic pressure, ν is the kinematic viscosity and ρ is the density. To obtain statistical stationarity

of turbulent features, large-scale forcing is employed. Here, a constant linear forcing term is used with the coefficient B tuned to compensate for the viscous dissipation [211, 212].

The global one-step chemistry is the following reversible reaction,

$$F + rO \rightleftharpoons (r+1)P, \tag{5.2}$$

where r is the stoichiometric ratio, which is the mass of oxidizer consumed with unit mass of fuel. For modeling purposes, mixture fraction is defined as

$$Z = \frac{rY_F - Y_O + Y_{O\infty}}{rY_{F\infty} + Y_{O\infty}}, \tag{5.3}$$

where Y_F and Y_O are mass fractions of fuel and oxidizer, respectively. The unmixed values of fuel and oxidizer ($Y_{F\infty},\ Y_{O\infty}$) are unity which results in $Z_s = 1/(r+1)$ for the stoichiometric value of the mixture fraction. In this work, $r = 1$ has been chosen resulting in $Z_s = 0.5$. The transport equations for mixture fraction and progress variable are

$$\frac{\partial Y_i}{\partial t} = -\boldsymbol{\xi} \cdot \nabla Y_i + D\nabla^2 Y_i + \omega_i. \tag{5.4}$$

Here, D is the coefficient of molecular diffusion of species, and reaction rate (ω_i) is zero in the governing equation of mixture fraction. In the current formulation, the product mass fraction (Y_P) is equivalent to the normalized temperature θ, and the reacting field is determined by solving for Z and θ, with the Schmidt number ($Sc = \nu/D$) equal to 0.7 for both scalars. For the reversible chemistry (Eq. 5.2) with an equilibrium constant K, the production rate of the products can be expressed as [223],

$$\omega_P = (r+1)A \exp\left(\frac{-\beta}{\alpha}\right) \exp\left(\frac{-\beta(1-Y_P)}{1-\alpha(1-Y_P)}\right) \left(Y_F Y_O - \frac{1}{K} Y_P^{r+1}\right), \tag{5.5}$$

where A is a pre-exponential factor, β is the Zeldovich number, and α is the dimensionless heat release parameter. These parameters are defined such that the reaction rate is strongly temperature-dependent, which can lead to local extinction and reignition controlled by the interaction of turbulent mixing and reaction [221].

The relative impact of turbulence on flame stability can be controlled using the reaction rate parameters. For this purpose, a Damkohler number is defined as $Da = \tau_\chi/\tau_c$, which is the ratio of turbulent mixing and reaction time scales. The local mixing time scale is characterized by the inverse of the scalar dissipation rate, $\chi = 2D\nabla Z \cdot \nabla Z$. Considering the chemistry of the flame, the Damkohler number can be expressed as [224],

$$Da = 16r^r(1 - Z_{st})^2 l_r^{2+r} A \exp\left(\frac{-\beta}{\alpha}\right)/\chi_s, \tag{5.6}$$

where l_r characterizes the width of the reaction zone, and χ_s is the dissipation rate of the mixture fraction at the stoichiometric mixture. Reaction thickness l_r is defined as $l_r = l_d Da^{-1/3}$ [225], where $l_d = (D/\chi)^{1/2}$ is the diffusive thickness. The statistics conditioned on the stoichiometric mixture fraction are obtained by averaging over this reaction thickness. Here, the pre-exponent A is chosen as the control parameter that is used to modify the Damkohler number (Table 5.1). Five different flame behaviors ranging from stable combustion to localized extinction and reignition and finally global extinction are observed for different values of Da considered. Table 5.2 provides characteristics of the flow field and thermochemistry parameters of the reacting field.

Flame I	Flame II	Flame III	Flame IV	Flame V
8×10^3	8×10^4	10^5	8×10^5	8×10^6

Table 5.1: Pre-exponent factor A for different flames

n_g	Re_λ	$k_{max}\eta$	B	Sc	α	β	K
256^3	83.25	1.72	5	0.7	0.87	4.0	100

Table 5.2: Characteristics of turbulence and thermochemistry parameters

5.1.1 DNS calculations and flame behavior

For the DNS calculations, the set of governing equations is solved in a 2π length cube with periodic boundary conditions using a pseudo-spectral code [226, 227]. A two-thirds dealiasing rule is used for the non-linear terms [228]. Exact time integration is used for the linear viscous term and RK2 is used for the other terms [229, 230]. Since small incompressibility errors can grow fast in a spectral formulation, it is necessary to remove the divergence error at every time step [213, 214]. At each time step, the velocity field is projected on the divergence-free space [213]. Turbulent field statistics such as the Taylor microscale Reynolds number $Re_\lambda = \frac{u'\lambda_g}{\nu}$, and the Kolmogorov length scale $\eta = (\frac{\nu^3}{\epsilon})^{1/4}$, are monitored over the initialization time to make sure the turbulent field is fully developed, where λ_g is computed as $\sqrt{15\frac{\nu}{\epsilon}}u'$ [6], u' is the fluctuating velocity and ϵ is the dissipation of turbulent kinetic energy. To resolve the velocity and conserved scalar field $k_{max}\eta > 1$ is required, where $k_{max} = 15/32N$ is the cut-off wavenumber and N is the number of grid points in one direction of the computational domain [231]. The flow statistics are monitored for approximately 200 eddy turnover times (τ) to ensure a fully developed forced statistically stationary flow field. The long transient time is chosen to make sure that the forcing does not lead to instability and energy pile-up at small scales, and the forcing energy is balanced with dissipation. The combustion and AIM investigation period starts when the flow becomes statistically stationary.

After the flow reaches statistical stationarity, the computational domain is filled homogeneously with blobs of fuel and oxidizer, corresponding to Z equal to one and zero respectively, such that the volume average of mixture fraction is equal to its stoichiometric value ($\langle Z_0 \rangle = Z_s$). The progress variable (normalized temperature) is initialized with solutions of the steady flamelet model, which is obtained from the

steady version of the following time-dependent flamelet model,

$$\frac{\partial Y_i}{\partial t} = \frac{\chi}{2}\frac{\partial^2 Y_i}{\partial Z^2} + \omega_i. \tag{5.7}$$

For initializing the temperature field, the scalar dissipation rate is modeled as $\chi(Z) = \chi_s \exp\left(-2\mathrm{erf}^{-1}\left[(2Z-1)^2\right]\right)$, [232].

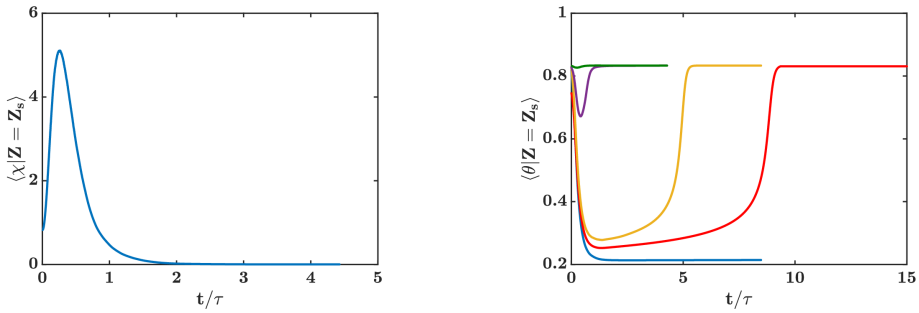

Figure 5.1: Left: time evolution of conditionally averaged mixture fraction dissipation rate $\langle\chi|Z=Z_s\rangle$; right: time evolution of conditionally averaged temperature $\langle\theta|Z=Z_s\rangle$, for different flames with different pre-exponential factors, A. Flame I: —, flame II: —, flame III: —, flame IV: —, flame V: —.

Figure 5.1 shows time evolution of mixture fraction dissipation rate (left) and temperature (right) at the stoichiometric mixture fraction. Due to straining, the scalar dissipation rate increases initially, and its fluctuations disrupt the stoichiometric surface. Strong fluctuations of turbulent mixing cause excessive heat losses at the flame surface leading to extinguished regions. When the reaction is faster than mixing, combustion heat release compensates for this heat loss leading to sustained high temperatures. By increasing the pre-exponential factor A, the flame behavior changes from global extinction to various degrees of localized extinction and reignition, and finally to the stably burning flame at equilibrium conditions. Local extinction is due to the fluctuations of the scalar dissipation rate. When the maximum fluctuation of scalar occurs, the reacting surface deviates from the equilibrium condition. At this transient moment, Da is computed from Eq. 5.6 for flames $I-V$ corresponding to

$A \in (8 \times 10^3, 8 \times 10^6)$. Figure 5.2 shows the Da number versus the flame thickness parameter $Z^* = Z_{rms}/l_r$ where Z_{rms} is the root mean square mixture fraction, and l_r is the width of the reaction zone in mixture fraction space. Relation between Da and Z^* shows the competition between turbulence and chemistry time and length scales. When the reaction is on average faster than mixing with the smaller reaction layer thickness (larger Z^*), stable combustion occurs (flame V). As Da is decreased, for a given Z^*, departure from equilibrium increases, and beyond a critical Da reaction can no longer balance heat loss of turbulent mixing, and global extinction occurs (flame I). At this critical Da, when localized extinction occurs, molecular mixing eventually overcomes the influence of turbulent straining and leads to the decrease of the scalar gradients. This process is accompanied by gradual reignition; ultimately the reacting scalar field returns to the stable burning solution. In the case of diffusion flames, there is no exact definition of critical Da, and it is determined based on the DNS cases considered (flames II, III and IV in this study) [223].

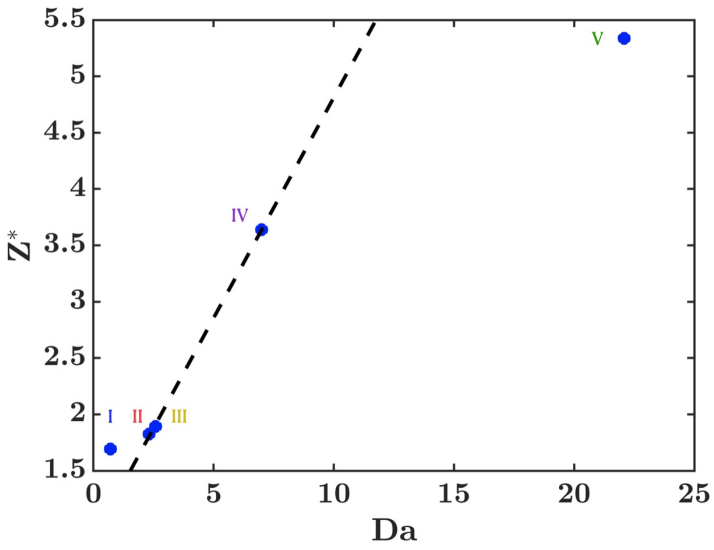

Figure 5.2: Sketch of $Da - Z^*$ relation for different flame behaviors. Dashed line shows the critical Da number. All values are computed at transient moment when $\langle \chi | Z = Z_s \rangle$ has its maximum value ($t/\tau \approx 0.25$). Legends colors are same as in Fig. 5.1.

5.2 Construction of an AIM for turbulent flames

In this section, the proposed approximate inertial manifold (Sec. 3.2.1) is constructed for the turbulent combustion cases discussed in Sec. 5.1. To develop an AIM, governing equations of the flow field and combustion scalars can be rearranged as Eq. 3.2 using the Stokes operator ($\nu\nabla^2\xi_i$ in Eq. 5.1) as the linear operator of the Navier-Stokes equations and the diffusion operator as the linear operator of the conserved and reacting scalars. Since the construction of an AIM for the underlying turbulent field is discussed in detail in Sec. 4.1.2.2, it is not stated here. Let $\hat{Y}_i = \mathcal{F}(Y_i)$ be the Fourier transform of scalars describing reaction field. Equation 5.4 can be rearranged as

$$\frac{d\hat{Y}_i}{dt} + D|k|^2\hat{Y}_i + \mathcal{F}(\boldsymbol{\xi}\cdot\nabla Y_i - \omega_i) = 0. \tag{5.8}$$

The projection operator that defines the resolved scales is parameterized using a three-dimensional wavenumber k_m, such that modes with wave numbers $\sqrt{k_x^2+k_y^2+k_z^2} \leq k_m$ are included in the resolved subspace. The number of modes satisfying this requirement is the dimension of AIM, m. By applying projections $\boldsymbol{P}$ and $\boldsymbol{Q} = \mathcal{I} - \boldsymbol{P}$ into Eq. 5.8, governing equations for the resolved and unresolved subspaces are obtained as

$$\frac{dy_i}{dt} + D|k|^2 y_i + \boldsymbol{P}\mathcal{R}(\boldsymbol{y},\boldsymbol{y'}) = 0, \tag{5.9}$$

and

$$\frac{dy_i'}{dt} + D|k|^2 y_i' + \boldsymbol{Q}\mathcal{R}(\boldsymbol{y},\boldsymbol{y'}) = 0, \tag{5.10}$$

where $y_i = \boldsymbol{P}\hat{Y}_i$, and $y_i' = \boldsymbol{Q}\hat{Y}_i$. Utilizing AIM assumption $d\boldsymbol{y'}/dt = 0$, the unresolved dynamics can be approximated by

$$y_i'^{j+1} = -(D|k|^2)^{-1}\big(\boldsymbol{Q}\mathcal{R}(\boldsymbol{y},\boldsymbol{y'^j})\big). \tag{5.11}$$

It is important to ensure reconstructed scalar fields do not violate mass conservation, and only physical realizations of the chemical composition space are reached by AIM. For this purpose, at each iteration of Eq. 5.11, for out of bound values of scalars chemical reaction term is set to zero. This is enough to ensure AIM only accesses physical trajectories of the chemical composition space, and there is no need for clipping mass fractions after reconstruction of species vector of variables. In this study, different values of k_m have been used to examine the performance and convergence of AIM approximation. The goal is to assess AIM performance in the prediction of different flame behaviors.

5.2.1 A priori analysis of the AIM for turbulent flames

In this section, the performance of AIM approximation is assessed *a priori* such that the unresolved dynamics are approximated by the information of the exact resolved dynamics. For each AIM resolution (m), the resolved modes ($\boldsymbol{u}$) are obtained by projection of the DNS data, then the unresolved variables ($\boldsymbol{w}$) are approximated using Eq. 5.11. The full-dimensional vector of variables reconstructed by AIM ($\boldsymbol{u}_{DNS}+\boldsymbol{w}_{AIM}$) is compared against the DNS data. In this regard, this analysis is different from conventional LES analyses. Note that LES models approximate the effect of the unresolved features in the resolved scale equation. As a result, the unresolved features are not directly reconstructed in conventional LES. Hence, the *a priori* analysis of sub-filter terms typically involves the comparison of the modeled term to the true sub-filter term. In the AIM approach, similar to deconvolution-based models [73, 74, 156, 233, 234], a representation of the unresolved scales is obtained. Hence, the full reconstructed field can be directly compared to the DNS field.

Global behavior of different flames is studied for various AIM resolutions in Fig. 5.3. Here, the time evolution of mixture fraction dissipation rate and temperature at the stoichiometric surface are compared. As discussed in Sec. 5.1.1, enhanced gradients

imposed by the underlying turbulent field disrupt the flame surface and induces localized extinction. Competition between chemistry and mixing time scales either results in reignition or higher levels of extinction that cause global quenching of the flame. Figure 5.3 (left) compares the time evolution of the mixture fraction dissipation rate modeled by AIM against the DNS results. Since AIM reconstructs the full-dimensional vector of variables, the dissipation rate can be computed directly without further modeling of the small scales. By increasing the AIM resolution m, the approximation becomes closer to the exact field. However, the maximum dissipation rate is underestimated by AIM. Here, the highest resolution AIM is obtained with $k_m = 64$ and is spanned by only three percent of the DNS modes.

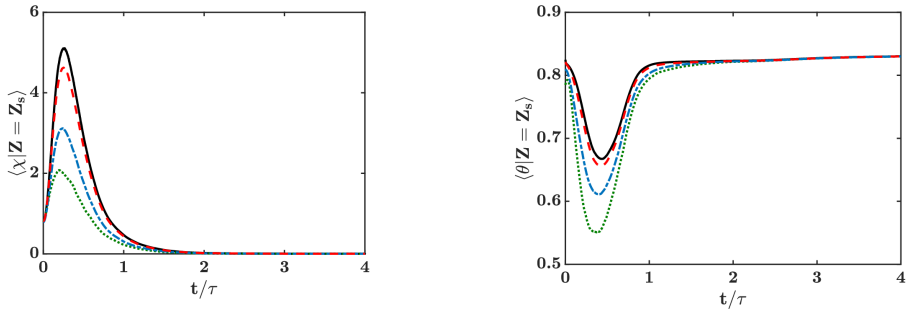

Figure 5.3: Left: time evolution of conditionally-averaged mixture fraction dissipation rate $\langle\chi|Z = Z_s\rangle$; right: time evolution of conditionally averaged temperature $\langle\theta|Z = Z_s\rangle$ for flame IV. DNS: —, AIM with $k_m = 16$: ···, AIM with $k_m = 32$: -·-, AIM with $k_m = 64$: - -.

Approximations of the conditionally averaged temperature $\langle\theta|Z = Z_s\rangle$, by different AIM resolutions (m) is compared against the DNS data for flame IV (Fig. 5.3, right). In this case, initially, the flame experiences a nominal temperature drop at the stoichiometric surface which shows localized extinction due to straining. Since the stoichiometric surface is still engulfed by a relatively high-temperature fuel and oxidizer mixture, the reaction rate increases, and the flame re-ignites and reaches an equilibrium state quickly. It is shown that flame-front temperature reconstructed by AIM follows similar behavior, but experiences more severe extinction and slower

return to stably burning flame. The reason behind this discrepancy between AIM and DNS can be the fast-moving trajectory of the system on the manifold such that the scale-separation between resolved and unresolved dynamics is not present.

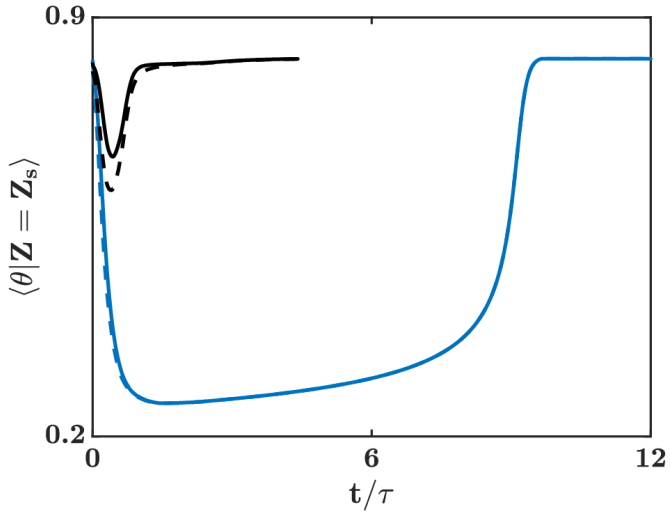

Figure 5.4: Time evolution of conditionally averaged temperature $\langle\theta|Z = Z_s\rangle$. DNS of flame II: —, and flame IV: —, AIM with $k_m = 32$ for flame II: -- and flame IV: --.

The reasoning above can be verified by comparing the AIM prediction of flames II and IV. Figure 5.4 compares conditionally averaged temperature at the flame surface reconstructed by AIM with $k_m = 32$ against the DNS data for fast and slow extinction and reignition events. At the same resolution, AIM approximation is significantly more accurate in the extent of the extinction and pace of the reignition for flame II. In this flame, the chemical reaction is slower, on average, than turbulence mixing. Initially, scalar fluctuations caused by turbulent mixing leads to extinction, and since the chemical reaction is slower, it cannot overcome the influence of turbulent straining. After a while, scalar gradients are decreased due to molecular mixing. This process is accompanied by gradual reignition; ultimately the reacting scalar field returns to the steady flamelet solution.

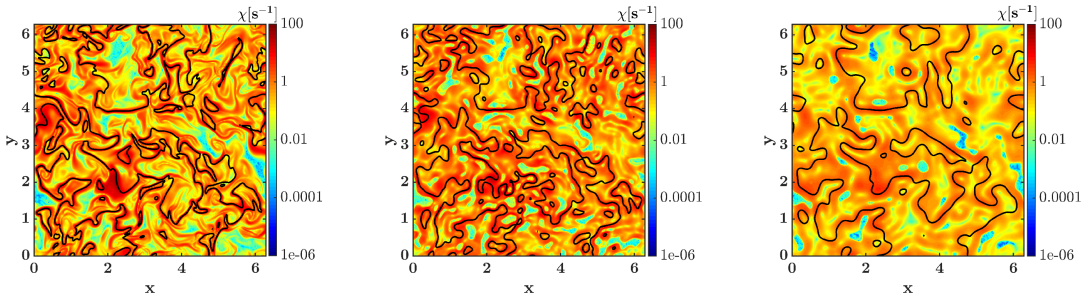

Figure 5.5: Mixture fraction dissipation rate $\chi = 2D(\nabla Z)^2$, in a plane of the computational domain at $t/\tau \approx 0.5$ when flame IV is locally extinguished. Left: DNS, middle: AIM, right: projected DNS field (only resolved scales). Projection cut-off wavenumber is $k_m = 16$. Black lines represent stoichiometric mixture, $Z = Z_s$.

In diffusion flames, the chemical reaction is controlled by strain and is proportional to the dissipation rate of reactants. By reconstruction of the small-scale quantities with AIM, scalar dissipation and chemical reaction rates can be directly computed from reconstructed temperature and mixture fraction fields without explicit modeling. Figure 5.5 shows the dissipation rate contours plotted when the mean temperature is the lowest (see Fig. 5.3). The presence of high dissipation rate values at the stoichiometric surface leads to local extinction. It is seen that the AIM reconstruction overall captures such structures, but differences can be found in the top right and top left corners of the domain where only small-scale reaction structures are present. At this cut-off wavenumber projection ($k_m = 16$), AIM dimension (m) is 0.05 percent of the DNS degrees of freedom. The dissipation rate computed from the projected DNS field, which includes only the resolved scales, is shown in Fig. 5.5 (right). At this projection cut-off wavenumber, large features of the field are preserved but small scales and maximum dissipation rates are not captured. AIM approximation can recover many of the small features.

An important component of turbulent combustion models is the prescription of the scalar dissipation rate, both for mixture fraction [132, 235] and reacting scalars [121, 148, 153]. More commonly, a time-scale is prescribed for the dissipation of scalar

variance [153, 236]. The characteristic time scale T_j, for dissipation of scalar energy can be defined as [237],

$$T_j = \langle Y_j^2 \rangle / \langle 2D(\nabla Y_j)^2 \rangle. \tag{5.12}$$

Models for this time scale typically assume that scalar dissipation is directly proportional to turbulent energy dissipation [6]. It has been widely observed that modeling of these terms has a first-order impact on the simulation predictions, but models even for non-reacting scalars such as mixture fraction can introduce large errors [114]. Since turbulent mixing enhances the gradients of species, which is nonlinearly impacted by Arrhenius chemistry, reacting scalar gradients can be locally steepened due to small-scale reaction zones. As a result, the length and time scales associated with reacting species can be vastly different from the predominantly turbulent mixing controlled non-reacting scalar properties. In addition, there is a time lag in the response of chemistry to turbulent straining, which can be seen in Figure 5.1. It shows that the scalar dissipation rate is initially increasing due to the straining effects of the turbulent field, and the maximum of scalar variations at the flame surface occurs at $t/\tau \approx 0.25$. The interplay of mixing and reaction leads to the extinction of flames $I - IV$, but this extinction happens after a finite time depending on the chemistry time scale. For instance, flames II and III are quenched by $t/\tau \approx 1.37$ when almost all of the scalar variations are dampened. On the other hand, flame IV responds much quicker to the turbulent mixing effects and experiences localized extinction at $t/\tau \approx 0.5$. So, even if the time scale for the dissipation of conserved scalar energy can be assumed to be proportional to the turbulent energy dissipation rate, the characteristic time scale for the reacting scalars need not follow this relation.

Only for infinitely fast irreversible chemistry or slow chemistry, where the assumption of dissipation balancing production is sufficiently accurate, is the characteristic time scale of all reacting scalars nearly identical and can be assumed to be proportional to the conserved scalar time scale [238]. Here, the ratio of progress variable

and mixture fraction time scales is compared for two flames experiencing minimal and maximal extinction under the straining effects of the turbulent field. Figure 5.6 compares some properties of flame II and flame IV, and the capability of AIM to reproduce them. The time scale ratio of reacting and conserved scalars (T_θ/T_Z), shows that on average, the reaction is faster than mixing. However, in flame IV with minimal extinction, the difference between time scales is more prominent, since this flame reignites quickly when the micro-scale mixing overcomes straining effects (Fig. 5.4).

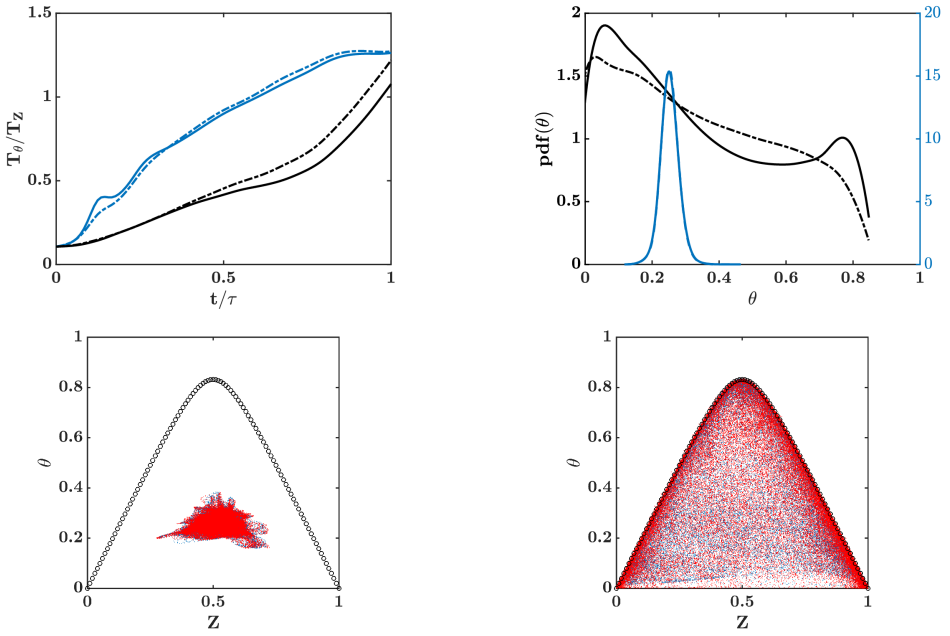

Figure 5.6: Top: time evolution of mixing time scale ratio of reactive and conserved scalars (T_θ/T_Z) (left) and probability distribution of temperature at $t/\tau = 0.5$ (right) for flames II (blue) and IV (black). DNS of flame II: —, and flame IV: —, AIM with $k_m = 32$ for flame II: -- and flame IV: --. Bottom: conditional distribution of temperature at $t/\tau = 0.5$ for flame II (left) and flame IV (right). DNS: blue dots, AIM: red dots and steady flamelet solutions: black circles.

Properties of temperature (progress variable) as these flames experience their extinction are compared further. The conditional distribution of temperature depicts very different behaviors. Flame II is globally extinguished, and there is little variation in the temperature field. On the contrary, flame IV experiences local extinction due to

breakage of flamelets, and since the micromixing of reactants is fast enough to enhance gradients, the flame re-ignites across the entire range of mixture fraction values. This is shown by the large variation of temperature (Fig. 5.6, bottom). Comparison of the probability distribution of temperature for these two flames illustrates their different responses to the straining turbulent field. AIM succeeds in representing these characteristics quite accurately, but the AIM approach is marginally better in flame II. This is expected since the trajectory is varying quickly in flame IV as compared to flame II.

Additional statistics of the scalar dissipation rate computed from the AIM reconstructed mixture fraction field is provided in Fig. 5.7, where three approximate inertial manifolds are compared against the DNS data at a time instance where the mixture fraction fluctuations (standard deviation of the field) is maximum. Overall, by increasing the AIM resolution (m), the approximation improves and converges to the exact solution. Figure 5.7 (top) shows that the conditional average of χ is captured quite accurately with the higher dimensional AIMs, but conditionally averaged fluctuations of mixture fraction are underestimated closer to the stoichiometric mixture fraction value even at the highest resolution AIM. The distribution of the range of scales in the mixture fraction field fluctuations is compared between DNS and AIM reconstructed fields with the normalized spectrum of the mixture fraction dissipation rate (Fig. 5.7, bottom left). The wavenumber space is scaled with the smallest scale of the scalar field $\eta_Z = \eta Sc^{-3/4}$, where η is the Kolmogorov scale and η_Z is the Batchelor's scale. AIM approximation can model the dissipation rate of mixture fraction at large scales, where there is a plateau in the spectrum corresponding to the inertial range of the turbulent scales, but the dissipation rate of the mixture fraction is underestimated at the small scales. The approximation improves by increasing the AIM resolution, but it cannot recover the small-scale dissipation rate entirely. Finally, the probability distribution of the dissipation rate (Fig. 5.7 bottom right) shows that in the lower-

dimensional AIM, the maximum of χ is underestimated, and the range of scales is not captured accurately. However, the approximation is considerably improved by increasing m.

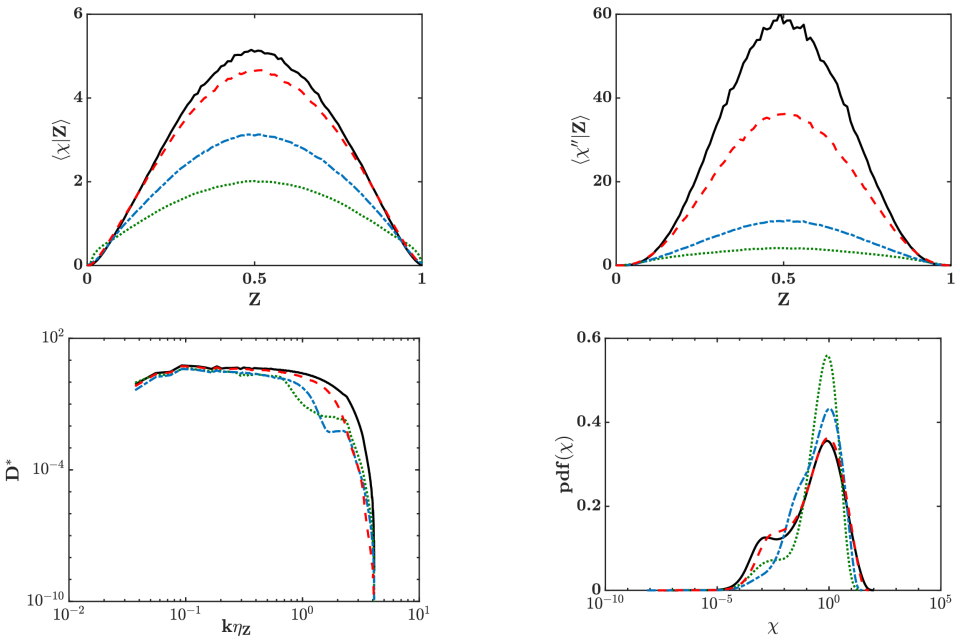

Figure 5.7: Statistical properties of mixture fraction dissipation rate χ, at $t/\tau \approx 0.25$. Top: conditional average (left) and conditional variance (right) of χ in mixture fraction space. Bottom: spectrum of the scalar dissipation rate normalized by $D(\epsilon\eta_Z)^{-1/3}\langle\chi\rangle$, where ϵ is the total dissipation, and $\eta_Z = \eta Sc^{-3/4}$ (left); and probability distribution function of χ (right). DNS: —, AIM with $k_m = 16$: ···, AIM with $k_m = 32$: ···, AIM with $k_m = 64$ - -.

Statistics of the temperature field and chemical reaction source term for flame III are presented in Fig. 5.8, showing that flame III experiences a mild extinction followed by reignition (top left). The conditional distribution of temperature in mixture fraction space shows large scatter, indicating regions of local extinction as well as fully burning pockets. AIM approximation with $k_m = 32$ can capture this variation, both in terms of the conditional mean and variance of temperature. While there is a slight underprediction of the conditional mean of reaction source term (bottom left), this effect is minimal in the prediction of the conditional mean of

temperature. AIM reconstruction overestimates variance of the chemical reaction source term, indicating that overall the predictions show a higher degree of extinction.

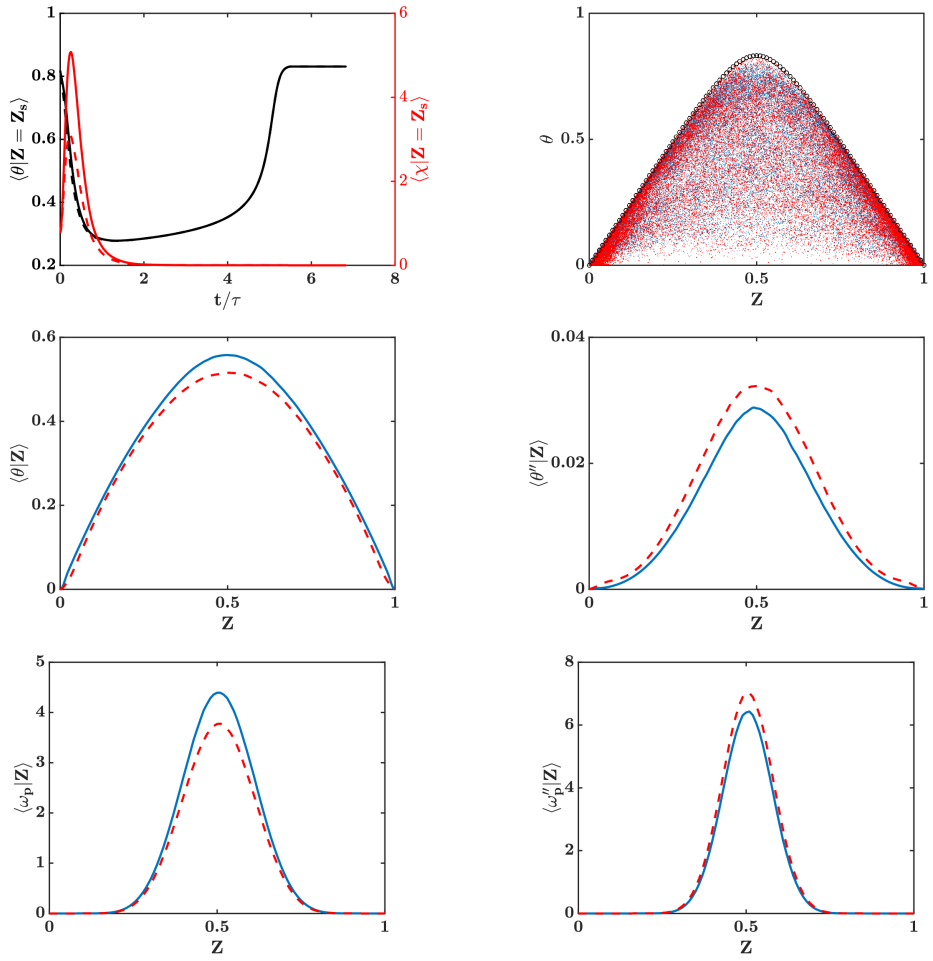

Figure 5.8: Statistical properties of flame III; top left: time evolution of conditional average of temperature and mixture fraction dissipation rate at $Z = Z_s$; DNS: solid lines, AIM: dashed lines. Each color represents values for the matching vertical axis. Top right: Conditional distribution of temperature in mixture fraction space (same legend as in Fig. 5.6, bottom). Middle: conditional mean (left) and variance (right) of temperature. Bottom: conditional mean (left) and variance (right) of chemical reaction source term (w_p). DNS: —, AIM: - -. Cut-off wavenumber for AIM projection is $k_m = 32$. Instantaneous plots are taken at $t/\tau \approx 0.25$ where $\langle\chi|Z = Z_s\rangle$ is maximum.

Finally, the temperature field of flame III reconstructed by a lower resolution AIM is compared against the DNS field in Fig. 5.9. Snapshots are taken when the mean

dissipation rate at the flame surface is the highest. Details of the flame distribution are captured in the AIM reconstructed field, but the flame temperature is underestimated in some regions.

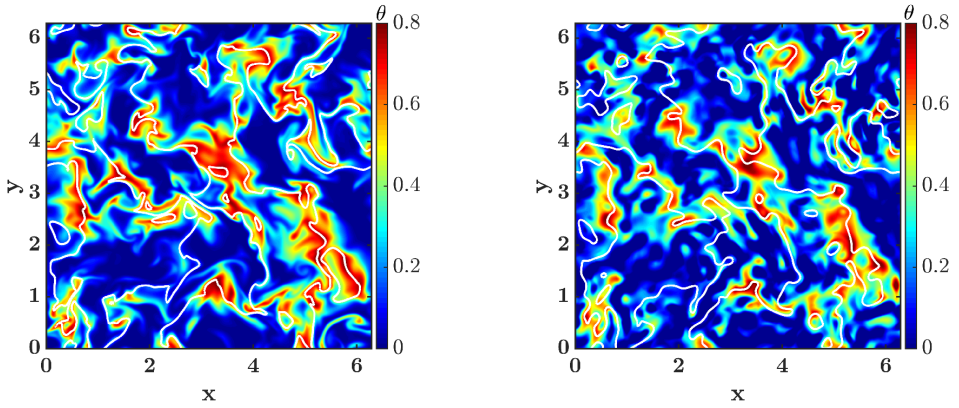

Figure 5.9: Temperature field for flame III at $t/\tau = 0.25$, when $\langle \chi | Z = Z_s \rangle$ is maximum. Left: DNS, right: AIM with $k_m = 16$. White lines represent $Z = Z_s$.

5.2.2 A posteriori analysis of AIM

In this section, the performance of AIM approximation is assessed *a posteriori* such that only the resolved dynamics are evolved to the next time step (Eq. 5.9), while the unresolved variables are approximated using the information of the resolved variables (Eq. 5.11), and the nonlinear term $\boldsymbol{P}\mathcal{R}(\boldsymbol{u}+\boldsymbol{w})$, is computed from the AIM-reconstructed full-dimensional vector of variables to close the governing equation of resolved variables. For each AIM resolution (m), the full-dimensional field modeled by AIM is compared against the DNS field. Here, three different AIM dimensions ($k_m = 16, 32, 64$) are analyzed for different Damkohler numbers. The velocity and scalar fields are evolved using the AIM, but the scalar field properties are discussed below.

The time evolution of dissipation rate of mixture fraction at stoichiometric mixture modeled by AIM is shown in Fig. 5.10 (left). Convergence of AIM prediction to the exact solution is different from the *a priori* analysis, and the lowest dimensional AIM

($k_m = 16$) overpredicts the dissipation rate. The reason for this behavior is that the approximate inertial manifold at this resolution ($k_m = 16, m = 8937$) is lower-dimensional than the estimated attractor dimension for the underlying turbulent field [100]. The insufficient resolution cannot reconstruct the dissipative range of the turbulent motions which manifests as enhanced mixing and a higher degree of turbulence. Spatial variation of the mixture fraction dissipation rate under the effect of turbulent straining is compared in Fig. 5.10 (middle and right). When turbulent mixing is dominant ($t/\tau \approx 0.25$), the stoichiometric mixture, represented with black lines, experiences the steepest gradients and becomes corrugated. It can be seen that a moderate resolution AIM ($k_m = 32$) can capture details of spatial structures quite accurately but it overestimates the scalar dissipation rate at less dissipative regions.

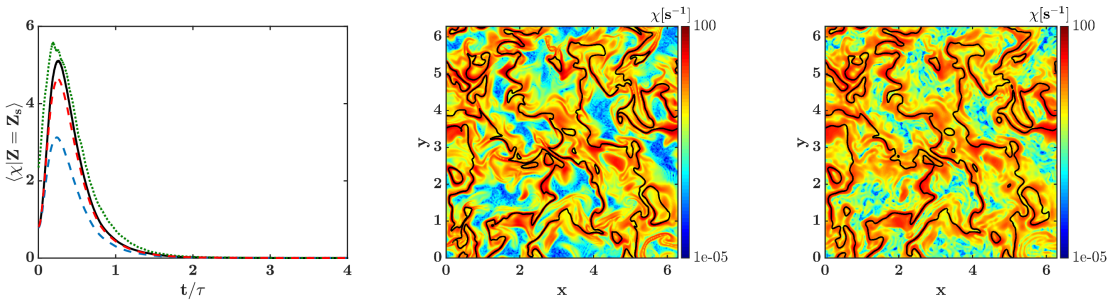

Figure 5.10: Left: time evolution of conditionally averaged χ at stoichiometric mixture; DNS:—, AIM with $k_m = 16$: ···, AIM with $k_m = 32$: -·-, AIM with $k_m = 64$ - -. Contour of χ in a plane of domain obtained from the DNS data (middle) and from AIM model with $k_m = 32$ (right). Black lines in contour plots mark stoichiometric mixture $Z = Z_s$, and fields are extracted at $t/\tau \approx 0.25$.

AIM model performance in modeling scalar dissipation rate is evaluated further in Fig. 5.11. While probability distribution and the conditional distribution of χ are captured well at higher resolutions, the conditional standard deviation of the dissipation field is underestimated considerably. The results shown here are when the turbulence effects are most prominent. In all cases, as the system moves towards equilibrium, the AIM performance improves.

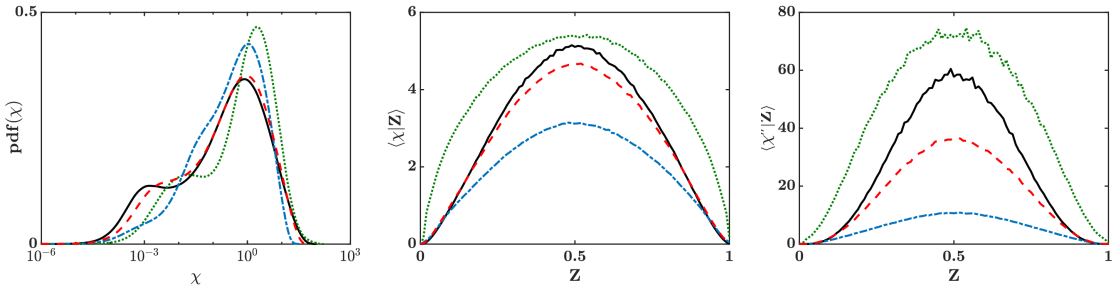

Figure 5.11: Convergence of AIM-ROM in modeling mixture fraction dissipation rate $\chi = 2D(\nabla Z)^2$ at $t/\tau \approx 0.25$, when maximum straining effect occurs. Left: probability density function of χ, middle: conditional expectation of χ, and right: conditional variance of χ. DNS:—, AIM with $k_m = 16$: ···, AIM with $k_m = 32$: ···, AIM with $k_m = 64$ - -.

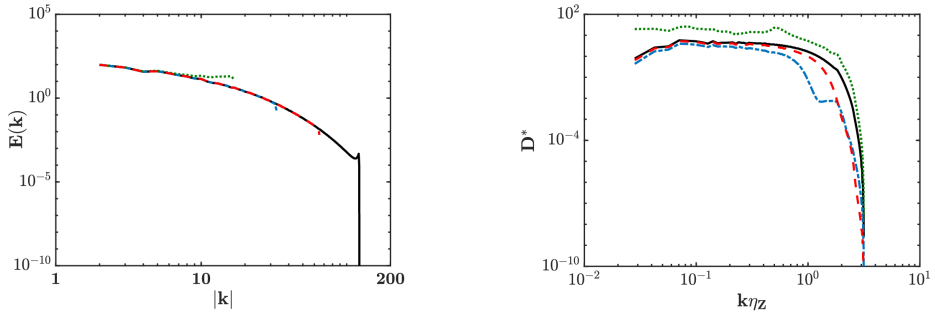

Figure 5.12: Convergence of AIM-ROM in modeling energy spectrum of the velocity field (left) and mixture fraction dissipation rate (right) at $t/\tau \approx 0.25$, when maximum straining effect occurs. DNS:—, AIM with $k_m = 16$: ···, AIM with $k_m = 32$: ···, AIM with $k_m = 64$ - -.

In Fig. 5.12, the AIM modeled field is compared against the DNS field in the spectral space by comparing the energy spectrum of the velocity field (left) and scalar dissipation rate (right) at different resolutions. The modeled turbulent energy spectrum contains only the modeled (resolved) scales at each AIM resolution. Different AIM resolutions can capture the large energy-containing and inertial range scales accurately. At the smallest AIM dimension ($k_m = 16$), the energy spectrum of the smaller resolved scales (close to the cut-off wavenumber) is overestimated, as there is not enough dissipation at this resolution. This behavior has led to a more turbulent field at this resolution, which enhances mixing of the scalars and results in higher

dissipation rate energy of scalars (Fig. 5.12, right). For higher-dimensional AIM, the energy spectrum of turbulent field and mixture fraction dissipation rate is captured more accurately but still underestimated at the smallest scales.

Figure 5.13 (left) compares T_θ/T_Z for flames II and IV up to $t/\tau = 1$, when both flames experience the highest scalar dissipation, causing flame II to globally quench, but only partial extinction in flame IV. The conditional distribution of temperature of these flames when they experience their maximum extinction is compared in Fig. 5.13 (right). As explained in the *a priori* analysis (Sec. 5.2.1), the faster reactions in flame IV leads to smaller time scales, which are captured by the AIM approach. The global extinction reduces the support of the temperature distribution function, with the near-Gaussian spread for flame II. On the other hand, there is a broader distribution for flame IV, with significant regions of low temperature consistent with the local extinction-reignition process.

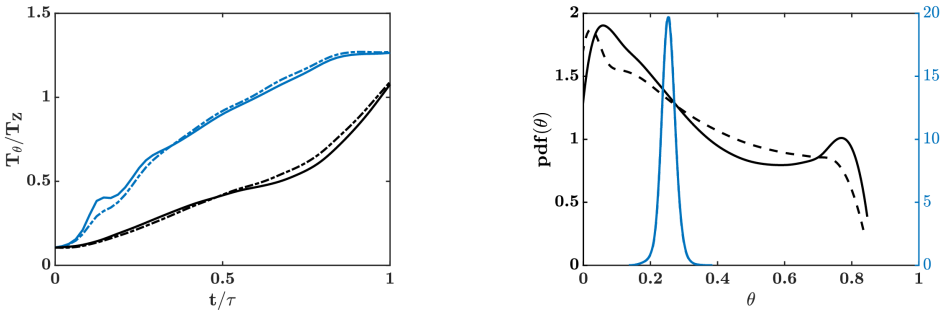

Figure 5.13: Left: time evolution of mixing time scale ratio of progress variable and mixture fraction (T_θ/T_Z), right: probability distribution of temperature at $t/\tau \approx 0.5$. DNS of flame II: —, and flame IV: —, AIM with $k_m = 32$ for flame II: -- and flame IV: --.

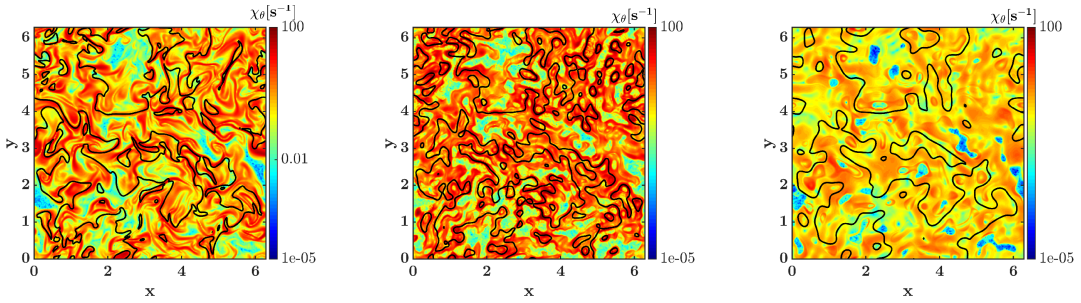

Figure 5.14: Dissipation rate of progress variable $\chi_\theta = 2D(\nabla\theta)^2$, for flame IV at $t/\tau = 0.5$ when flame is locally extinguished. Left: DNS, middle: AIM, right: no model prediction. Projection operator is at $k_m = 16$. Black lines represent stoichiometric mixture.

Dissipation rate of the progress variable (temperature) of flame IV when local extinction is maximum (lowest conditional temperature in Fig. 5.3, right). Near the stoichiometric mixture fraction surface (shown by black lines), higher reaction rates impose steeper temperature gradients, which emphasizes the reaction effects on small-scale mixing. Modeling of χ_θ with the lowest dimensional AIM considered here can reproduce most features of the field. However, the dissipation rate is overestimated in general. Compared to the reduced-order evolution of dynamics without any form of reconstruction of the unresolved modes (Fig. 5.14, right), AIM has managed to recover small-scale features of the field.

Figure 5.15 compares some statistics of temperature field for flame IV predicted by AIM-ROM against the DNS data. Global behavior of the flame is compared in Fig. 5.15 (top left) showing the time evolution of conditioned temperature and mixture fraction dissipation rate. Overall, AIM captures the local extinction and subsequent reignition, but it overpredicts the extent of extinction. Given that the dissipation rate is underpredicted at the flame surface, this result shows that AIM suppresses reactions away from the stoichiometric surface. Distribution of temperature and mixture fraction dissipation rate at stoichiometric mixture at $t/\tau \approx 0.5$ illustrates more details of extinction (Fig. 5.15,top right). While part of the stoichiometric mixture is burning close to the steady flamelet solution, localized extinction has

created considerable cold and non-burning regions. Bi-modal distribution of the temperature shown in Fig. 5.13 (right) is evidence of this locally extinguished flame. It can be seen that the range of scalar dissipation values is underestimated by AIM. In particular, burning flamelets under higher strain rates are not captured. Additionally, AIM predicts lower reaction rates and temperatures under medium strain rates. These behaviors result in overprediction of the extent of extinction. Conditional distribution of temperature and its variance are compared in Fig. 5.15 (bottom). Overall, AIM can predict flame structure reasonably well and handles local extinction and reignition without any additional modeling.

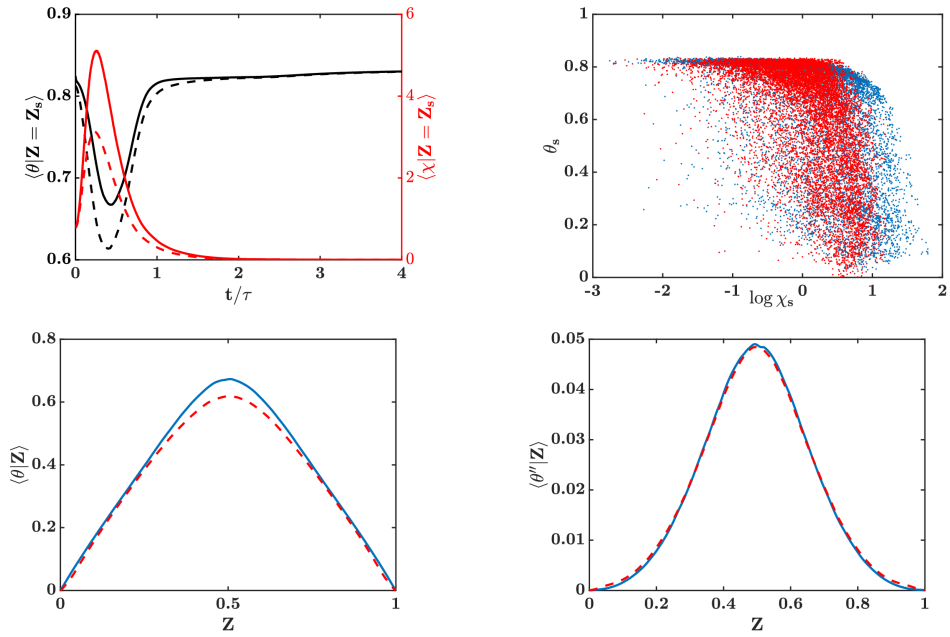

Figure 5.15: Statistical properties of flame IV. Top left: time evolution of conditionally averaged temperature and mixture fraction dissipation rate. Solid lines are DNS results, and dashed lines are AIM-ROM results with $k_m = 32$. Top right: the distribution of temperature and mixture fraction dissipation rate at stoichiometric surface at $t/\tau = 0.5$. Bottom: conditional mean (left) and variance (right) of temperature at $t/\tau = 0.5$; DNS: —, AIM: - -.

5.3 Summary

In this chapter, the theory of inertial manifolds is used to develop reduced-order models of turbulent combustion. In this approach, the dynamic interplay of turbulence and chemistry is tracked in a low-dimensional manifold determined *in-situ* without invoking laminar flame structures or statistical assumptions about the underlying turbulent flow. Direct numerical simulations of initially non-premixed fuel-air mixtures developing in forced isotropic turbulence have been carried out to investigate the proposed model. Reaction rate parameters are varied to allow for varying levels of extinction and reignition. The AIM performance in capturing different flame behaviors is assessed both *a priori* and *a posteriori*. It is shown that AIM captures the dynamics of the flames including extinction and reignition. Moreover, AIM provides scalar dissipation rate, mixing time for reactive scalars, and closures for nonlinear terms without any additional modeling.

CHAPTER VI

Summary, Conclusions and Future Directions

6.1 Summary

The objective of this dissertation is to provide a framework for the development of a reduced-order description of multi-physics multi-scale systems in the context of turbulent reacting flows. The goal is to develop models that can track distinct trajectories of the system without limiting assumptions about the underlying turbulent flow or flame structures. The theory of inertial manifolds is leveraged for deriving a modeling approach for turbulent combustion. The foundations of this modeling principle are fundamentally different from other modeling practices in turbulence or turbulent combustion. The proposed model is investigated on canonical turbulent flows and turbulent flames. The rest of this section summarizes the chapter-by-chapter advances presented in this work.

Chapter I:

In this chapter, the need for a predictive model of combustion devices, when such devices deviate from their design point, is discussed. Several examples of transient events in combustors are provided to emphasize the importance of these events in the efficiency, robustness, and pollutant formation of modern energy conversion systems. The computational challenge of direct methods for an extensive analysis of combustion devices is discussed, and a need for reduced-order descriptions of practical reacting

flows is outlined. It is further explained why models driven for statistically stationary systems cannot address this need.

Chapter II:

Predominant modeling approaches in turbulence and turbulent combustion are reviewed in this chapter. It is discussed that current models are geared toward statistically stationary systems, and they provide an ensemble average of all possible realizations of the flow. In particular, combustion models depend on external manifold developments based on the thermochemical composition of laminar flame structures. This comprehensive image of state-of-the-art models reveals the need for models that can track distinctive trajectories of reacting flows far from normal behavior. To predict deviation from nominal conditions in energy conversion systems a paradigm shift in modeling perspective is essential. The development of models that do not rely on statistical assumptions about small-scale turbulent features or canonical flame configurations is critical for the predictive accuracy of these tools.

Chapter III:

In this chapter, the theory of inertial manifolds is introduced. The existence of an inertial manifold for certain systems is discussed, and key properties of such manifolds are provided. A reduced-order model describing reacting flows is developed by invoking a dynamical systems perspective. Based on the inertial manifold theory, governing equations of the system are utilized for the decomposition of the system's dynamics into resolved and unresolved subsets. An inertial form describing the dynamical behavior of the system in a low-dimensional manifold is derived. Particularly, it is shown that the proposed model recovers a single realization of the unresolved field for a given resolved field. Therefore, distinct trajectories of the system can be tracked, which is essential for the forecast of transient events.

Chapter IV:

The suitability of approximate inertial manifolds in the prediction of turbulent flows is

examined in this chapter. Two canonical chaotic flows with different complexities and properties are considered. The one-dimensional Kuramoto-Sivashinsky equation is known to possess a relatively low-dimensional inertial manifold. Current theories can only provide an upper bound for the dimension of this manifold. In this chapter, the possibility of approximating the IM is investigated over a wide range of parameters such that the KSE is in a fully chaotic regime. Strong convergence properties conform with theoretical works. Convergence of the proposed AIM suggests a low-dimensional manifold spanned by unstable modes of the KSE. An AIM-based ROM is used to track the dynamical behavior of the system in a considerably lower-dimensional manifold.

The proposed model is also examined for homogeneous isotropic turbulence dictated by the three-dimensional Navier-Stokes equations. The existence of an IM for the Navier-Stokes equations is still an open question. The AIM approach tries to locate a neighborhood of the attractor in the state space. The AIM is studied over a wide range of parameters such as the dimension of the AIM, the dimension of the unresolved subspace, and the Reynolds number, which is directly proportional to the dimension of the attractor. Convergence properties of the approximate inertial manifold for HIT were found to be considerably different from the KSE. However, in all configurations considered, for AIMs with dimensions of the same order as the estimated size of the attractor, convergence rates improve. The AIM-based ROM can reconstruct nonlinear interaction between resolved and unresolved dynamics effectively, especially for the dynamics in the vicinity of the AIM. Higher-order approximations of an AIM are required to reconstruct smaller scales in the unresolved subspace. Another modeling component similar to eddy viscosity models in LES is introduced to account for these scales and to make the model computationally more efficient.

Chapter V:

The theory of inertial manifolds is used to develop reduced-order models of turbulent combustion. In this chapter, the dynamics of turbulent flames are tracked in a low-

dimensional manifold determined *in-situ* without invoking laminar flame structures or statistical assumptions about the underlying turbulent flow. Direct numerical simulations of initially non-premixed fuel-air mixtures developing in forced isotropic turbulence have been carried out to investigate the proposed model. Reaction rate parameters are varied to allow for varying levels of extinction and reignition. The AIM performance in capturing different flame behaviors is assessed both *a priori* and *a posteriori*. It is shown that the small-scale dynamics are reconstructed fairly accurately, even when the AIM contains only a small number of resolved modes. In particular, the AIM-reconstructed field captures various degrees of localized extinction and reignition due to the interplay of straining and molecular diffusion. This assessment of AIM approximation encourages the development of reduced-order models using the inertial manifold theory for more practical combustion systems.

6.2 Conclusions

In multiscale complex nonlinear systems, it is desired to predict the dynamical behavior without resolving all of the scales within the system through direct numerical simulations. In this context, the approximate inertial manifold methodology is a valuable alternative, naturally yielding a reduced-order approach while capturing the dominant dynamics of the problem. Casting the discretized governing equations as a dynamical system provides a path for the decomposition of variables without relying on traditional scale-separation methods, such as spatial filtering. Here, governing equations of the system have been leveraged to define resolved variables and recover unresolved variables to directly compute the nonlinear term. The underlying notion is that the slow modes of the dynamical system will traverse a stable low-dimensional manifold, and the fast variables are at a steady state that is controlled only by the slow variables. In this study, the suitability of the inertial manifold theory for the prediction of reacting turbulent flows is assessed.

The existence of an inertial manifold is not yet proven for turbulent flows. Nevertheless, the construction of an AIM for the Navier-Stokes equations shows promising results. The AIM-based reduction requires that the dimension of the reduced-order model should be higher than the dimension of the attractor. Since exactly obtaining the attractor dimension is not feasible for most practical problems, the AIM reduction for different dimensions is used to understand the validity of this approximation. Convergence properties of the AIM conform with direct estimations of the size of the attractor for these systems proving the proposed AIM can approximate the dynamics of the attractor.

For a given resolved field, AIM reconstructs a single realization of the unresolved dynamics. This contribution of an AIM to the resolved dynamics can also be seen as a subgrid-scale model. In all configurations, for a sufficiently large dimension of the AIM, the unresolved dynamics were found to respond to the dynamics of the AIM instantaneously. However, smaller scales in the unresolved dynamics are less responsive to the dynamics of the IM, and there is a time delay in their response. A higher-order estimation of the unresolved dynamics, where the interactions between the resolved and unresolved dynamics are included, improves the AIM estimation of the unresolved dynamics. The rate of convergence is controlled by the nonlinear interaction between resolved and unresolved scales. However, turbulence is broadband, and the approximation of unresolved dynamics farther from the approximate inertial manifold can be cost-prohibitive. It is shown that reconstruction of the entire unresolved subspace is not necessary, and recovering the unresolved dynamics in the vicinity of the AIM captures the nonlinear interaction sufficiently. The information recovered by AIM is used to model the effect of the dynamics far from the AIM. The modified AIM approach is robust, efficient, and more accurate in the prediction of long-time statistics of the system. The modified model shows the capacity of the AIM approach for an adaptive modeling framework.

Assessment of the AIM approach for turbulent flames proves it an effective alternative for combustion modeling. The main advantage of the AIM approach is that it models the small-scale features using a self-consistent approximation. In other words, no external modeling information regarding the structure of the chemical manifold or energy spectrum is needed. Forced isotropic turbulence with one-step chemical reaction and neglecting density variations is considered. The parameters of the reaction rate are varied to allow for local extinction and reignition. Extinction and reignition are considered deviations from laminar flames burning at equilibrium in a turbulent flow. Competing time scales of micro-mixing and chemical reaction determine the flame dynamics.

Considering one-step chemical reaction and neglecting density variations are significant simplifications of end applications. However, the purpose of this study is the interplay of turbulent mixing and reaction rate in flame dynamics. Various reignition pace for different flames is due to different mechanisms that derive reignition. In a fast reignition, mixing of cold and hot spots enhanced by underlying turbulent field triggers reignition. On contrary, a gradual reignition is controlled by the chemical reaction rate. AIM decomposition is based on the linear operator of the system, and accurate prediction of flame behaviors controlled by chemical reaction is very promising for this approach. For all the cases studied, the AIM reconstruction captures the variations in the small scales. The model is particularly accurate when the large scales evolve slowly in time, for instance through a gradual reignition process rather than a sudden return to equilibrium. Moreover, the AIM approach can provide scalar dissipation rate, mixing time for reactive scalars, and closures for nonlinear terms without any additional modeling. In this context, it overcomes some of the limitations of manifold-based techniques such as flamelet-generated or flamelet-based approaches.

In the AIM-based ROM, approximation of the small scales is used to obtain the closure terms and evolve the dynamics of the AIM. This feedback to the simulation

does not cause an accumulation of errors, and the model predicts various dynamics of the flames. In particular, extinction and re-ignition processes are well-captured. Overall, the results of this study are promising. It shows for the first time that dynamical systems-based modeling can be used to close turbulent reacting flow systems. While the concept of manifolds is well-known in the combustion community, this term generally refers to laminar flame or other non-turbulent configuration-based representation. In this work, a fully turbulent manifold has been constructed through the AIM procedure.

6.3 Future challenges and recommendations

Studying the attractor of chaotic systems provides new paths for the development of reduced-order models to predict and control complex systems. Direct methods for finding the topology of the attractor are prohibitively expensive, but strong convergence properties observed for approximate inertial manifolds over a range of problems considered in this dissertation show the potential of this approach in locating the attractor of more practical systems. The next steps will involve extensions to non-homogeneous systems such as wall-bounded flows, for which the AIM approach should be cast in physical space [194]. Similar to multi-grid methods, a hierarchy of discretizations can be used for AIM formulation in physical space. The inherent assumption of AIM formulation is the relative dominance of the linear operator at the unresolved dynamics. A budget study of the solution provides a premise for adaptive mesh refinement using the AIM formulation.

To assess the potentials of the IM theory for combustion systems, more realistic combustion processes should also be considered. The promising results of this work show that AIM can capture the interplay of micro-mixing and chemical reactions without any additional mixing model. But AIM relies on the linear operator for decomposition of dynamics of the system, and it might not be suitable for modeling

detailed chemistry mechanisms. Other approaches such as the G-scheme, which uses both linear and nonlinear operators for decomposition of slow/fast dynamics, are more amenable for combustion manifold development [166]. Currently, such approaches suffer from the cost of computing the Jacobian of the governing equations. The development of an adaptive chemistry approach can compensate for shortcomings of each of these approaches in cost and accuracy to develop chemistry manifolds on the fly.

The approximate inertial manifold approach provides a promising framework for the mitigation of extreme events. Extreme events, driven by events in the tails of the distribution, arise spontaneously in chaotic dynamical systems. It is shown that some regions of the attractor are more likely to contain the precursors of extreme events [239, 240]. A parameterization of the attractor provides the path to search for regions with a higher likelihood of extreme events and mitigate such events. In particular, a phase-space parameterization allows minimal control mechanism on the degrees of freedom that trigger the formation of an extreme event [239]. The system experiencing the extreme event and the system with mitigated extreme events share the same attractor. An approximation of this attractor reduces the search for precursors of extreme events to a low-dimensional manifold of the state-space.

BIBLIOGRAPHY

BIBLIOGRAPHY

[1] Chong, S. T., Hassanaly, M., Koo, H., Mueller, M. E., Raman, V., and Geigle, K.-P., "Large eddy simulation of pressure and dilution-jet effects on soot formation in a model aircraft swirl combustor," *Combustion and Flame*, Vol. 192, 2018, pp. 452–472.

[2] Ebi, D. and Clemens, N. T., "Experimental investigation of upstream flame propagation during boundary layer flashback of swirl flames," *Combustion and Flame*, Vol. 168, 2016, pp. 39–52.

[3] An, Q., Kwong, W. Y., Geraedts, B. D., and Steinberg, A. M., "Coupled dynamics of lift-off and precessing vortex core formation in swirl flames," *Combustion and Flame*, Vol. 168, 2016, pp. 228–239.

[4] Barwey, S., Hassanaly, M., An, Q., Raman, V., and Steinberg, A., "Experimental data-based reduced-order model for analysis and prediction of flame transition in gas turbine combustors," *Combustion Theory and Modelling*, Vol. 23, No. 6, 2019, pp. 994–1020.

[5] Read, R. W., *Experimental investigations into high-altitude relight of a gas turbine*, Ph.D. thesis, University of Cambridge, 2008.

[6] Pope, S. B., *Turbulent Flows*, Cambridge University Press, 2000.

[7] Raman, V. and Hassanaly, M., "Emerging trends in numerical simulations of combustion systems," *Proceedings of the Combustion Institute*, Vol. 37, No. 2, 2019, pp. 2073–2089.

[8] Wagner, J., Yuceil, K., and Clemens, N., "Velocimetry measurements of unstart of an inlet-isolator model in Mach 5 flow," *AIAA journal*, Vol. 48, No. 9, 2010, pp. 1875–1888.

[9] Koo, H. and Raman, V., "Large-eddy simulation of a supersonic inlet-isolator," *AIAA journal*, Vol. 50, No. 7, 2012, pp. 1596–1613.

[10] Sforzo, B., Kim, J., Jagoda, J., and Seitzman, J., "Ignition probability in a stratified turbulent flow with a sunken fire igniter," *Journal of Engineering for Gas Turbines and Power*, Vol. 137, No. 1, 2015, pp. 011502.

[11] Tang, Y., Hassanaly, M., Raman, V., Sforzo, B., and Seitzman, J., "A comprehensive modeling procedure for estimating statistical properties of forced ignition," *Combustion and Flame*, Vol. 206, 2019, pp. 158–176.

[12] Hassanaly, M. and Raman, V., "Computational Tools for Data-poor Problems in Turbulent Combustion," *AIAA Scitech 2019 Forum*, 2019, p. 0998.

[13] Sommerer, Y., Galley, D., Poinsot, T., Ducruix, S., Lacas, F., and Veynante, D., "Large eddy simulation and experimental study of flashback and blow-off in a lean partially premixed swirled burner," *Journal of Turbulence*, Vol. 5, No. 37, 2004.

[14] Heeger, C., Gordon, R., Tummers, M., Sattelmayer, T., and Dreizler, A., "Experimental analysis of flashback in lean premixed swirling flames: upstream flame propagation," *Experiments in fluids*, Vol. 49, No. 4, 2010, pp. 853–863.

[15] Konle, M., Kiesewetter, F., and Sattelmayer, T., "Simultaneous high repetition rate PIV–LIF-measurements of CIVB driven flashback," *Experiments in Fluids*, Vol. 44, No. 4, 2008, pp. 529–538.

[16] Stöhr, M., Boxx, I., Carter, C., and Meier, W., "Dynamics of lean blowout of a swirl-stabilized flame in a gas turbine model combustor," *Proceedings of the Combustion Institute*, Vol. 33, No. 2, 2011, pp. 2953–2960.

[17] Oberleithner, K., Stöhr, M., Im, S. H., Arndt, C. M., and Steinberg, A. M., "Formation and flame-induced suppression of the precessing vortex core in a swirl combustor: experiments and linear stability analysis," *Combustion and Flame*, Vol. 162, No. 8, 2015, pp. 3100–3114.

[18] Richardson, L. F., *Weather prediction by numerical process*, Cambridge university press, 1922.

[19] Kolmogorov, A. N., "The local structure of turbulence in incompressible viscous fluid for very large Reynolds numbers," *Dokl. Akad. Nauk SSSR*, Vol. 30, 1941, pp. 299–303.

[20] Kolmogorov, A. N., "Dissipation of energy in locally isotropic turbulence," *Dokl. Akad. Nauk SSSR*, Vol. 32, 1941, pp. 19–21.

[21] George, W. K. and Hussein, H. J., "Locally axisymmetric turbulence," *Journal of Fluid Mechanics*, Vol. 233, 1991, pp. 1–23.

[22] Domaradzki, J. A., "Nonlocal triad interactions and the dissipation range of isotropic turbulence," *Physics of Fluids A: Fluid Dynamics*, Vol. 4, No. 9, 1992, pp. 2037–2045.

[23] Zhou, Y., "Interacting scales and energy transfer in isotropic turbulence," *Physics of Fluids A: Fluid Dynamics*, Vol. 5, No. 10, 1993, pp. 2511–2524.

[24] Van Atta, C. and Antonia, R., "Reynolds number dependence of skewness and flatness factors of turbulent velocity derivatives," *The Physics of Fluids*, Vol. 23, No. 2, 1980, pp. 252–257.

[25] Piomelli, U., "Large-eddy and direct simulation of turbulent flows," *Lecture series-van Kareman Institute for fluid dynamics*, Vol. 4, 2000, pp. G1–G70.

[26] Law, C. K., "Combustion at a crossroads: Status and prospects," *Proceedings of the Combustion Institute*, Vol. 31, No. 1, 2007, pp. 1–29.

[27] Lu, T. and Law, C. K., "Linear time reduction of large kinetic mechanisms with directed relation graph: n-Heptane and iso-octane," *Combustion and flame*, Vol. 144, No. 1-2, 2006, pp. 24–36.

[28] Fiorina, B., "Accounting for complex chemistry in the simulations of future turbulent combustion systems," *57th AIAA Aerospace Sciences Meeting*, 2019.

[29] O'Brien, J., Towery, C. A., Hamlington, P. E., Ihme, M., Poludnenko, A. Y., and Urzay, J., "The cross-scale physical-space transfer of kinetic energy in turbulent premixed flames," *Proceedings of the Combustion Institute*, Vol. 36, No. 2, 2017, pp. 1967–1975.

[30] Kolla, H., Hawkes, E., Kerstein, A., Swaminathan, N., and Chen, J., "On velocity and reactive scalar spectra in turbulent premixed flames," *Journal of Fluid Mechanics*, Vol. 754, 2014, pp. 456–487.

[31] O'Brien, J., Urzay, J., Ihme, M., Moin, P., and Saghafian, A., "Subgrid-scale backscatter in reacting and inert supersonic hydrogen-air turbulent mixing layers," *Journal of fluid mechanics*, Vol. 743, 2014, pp. 554.

[32] Kazbekov, A. and Steinberg, A. M., "Physical space analysis of cross-scale turbulent kinetic energy transfer in premixed swirl flames," *Combustion and Flame*, Vol. 229, 2021, pp. 111403.

[33] Temam, R., "Induced trajectories and approximate inertial manifolds," *ESAIM: Mathematical Modelling and Numerical Analysis*, Vol. 23, No. 3, 1989, pp. 541–561.

[34] Keefe, L., Moin, P., and Kim, J., "The dimension of attractors underlying periodic turbulent Poiseuille flow," *Journal of Fluid Mechanics*, Vol. 242, 1992, pp. 1–29.

[35] Vastano, J. A. and Moser, R. D., "Short-time Lyapunov exponent analysis and the transition to chaos in Taylor-Couette flow," *Journal of Fluid Mechanics*, Vol. 233, 1991, pp. 83–118.

[36] Kalnay, *Atmospheric Modeling, Data Assimilation and Predictability*, Cambridge University Press, 2003.

[37] Hassanaly, M. and Raman, V., "Numerical convergence of the Lyapunov spectrum computed using low Mach number solvers," *Journal of Computational Physics*, Vol. 386, 2019, pp. 467–485.

[38] Hassanaly, M. and Raman, V., "Ensemble-LES analysis of perturbation response of turbulent partially-premixed flames," *Proceedings of the Combustion Institute*, Vol. 37, No. 2, 2019, pp. 2249–2257.

[39] Temam, R., "Do inertial manifolds apply to turbulence?" *Physica D: Nonlinear Phenomena*, Vol. 37, No. 1-3, 1989, pp. 146–152.

[40] Duraisamy, K., Iaccarino, G., and Xiao, H., "Turbulence modeling in the age of data," *Annual Review of Fluid Mechanics*, Vol. 51, 2019, pp. 357–377.

[41] Smagorinsky, J., "General circulation experiments with the primitive equations: I. The basic experiment," *Monthly weather review*, Vol. 91, No. 3, 1963, pp. 99–164.

[42] Mansour, N., Moin, P., Reynolds, W., and Ferziger, J., "Improved methods for large eddy simulations of turbulence," *Turbulent shear flows I*, Springer, 1979, pp. 386–401.

[43] Moin, P. and Kim, J., "Numerical investigation of turbulent channel flow," *Journal of fluid mechanics*, Vol. 118, 1982, pp. 341–377.

[44] Rogallo, R. S. and Moin, P., "Numerical simulation of turbulent flows," *Annual Reviews of Fluid Mechanics*, Vol. 16, 1984, pp. 99–137.

[45] Sagaut, P., *Large eddy simulation for incompressible flows: an introduction*, Springer Science & Business Media, 2006.

[46] Raman, V. and Hassanaly, M., "Emerging Trends in Numerical Simulations of Combustion Systems," *Proceedings of the Combustion Institute*, Vol. 37, 2019, pp. 2073–2089.

[47] Leonard, A., "Energy cascade in large-eddy simulations of turbulent fluid flows," *Advances in geophysics*, Vol. 18, Elsevier, 1975, pp. 237–248.

[48] Leslie, D. and Quarini, G., "The application of turbulence theory to the formulation of subgrid modelling procedures," *Journal of fluid mechanics*, Vol. 91, No. 1, 1979, pp. 65–91.

[49] Piomelli, U., Moin, P., and Ferziger, J. H., "Model consistency in large eddy simulation of turbulent channel flows," *The Physics of fluids*, Vol. 31, No. 7, 1988, pp. 1884–1891.

[50] Ghosal, S. and Moin, P., "The Basic Equations for the LES of Turbulent Flows in Complex Geometry," *Journal of Computational Physics*, Vol. 118, 1995, pp. 24–37.

[51] Vasilyev, O., Lund, T., and Moin, P., "A general class of commutative filters for LES in complex geometries," *Journal of Computational Physics*, Vol. 146, No. 1, Oct. 1998, pp. 82–104.

[52] Boussinesq, J., "Essai Sur La Theorie Des Eaux Courantes," *Mem. Presentes Acad. Sci.*, Vol. 23, 1877, pp. 46.

[53] Jimenez, J. and Moser, R. D., "Large-eddy simulations: where are we and what can we expect?" *AIAA journal*, Vol. 38, No. 4, 2000, pp. 605–612.

[54] Liu, S., Meneveau, C., and Katz, J., "On the properties of similarity subgrid-scale models as deduced from measurements in a turbulent jet," *Journal of Fluid Mechanics*, Vol. 275, 1994, pp. 83–119.

[55] Lilly, D. K., "The Representation of Small-scale Turbulence in Numerical Simulation Experiments," *Proceedings of the IBM Scientific Computing Symposium on Environmental Sciences*, edited by H. H. Goldstine, IBM, Yorktown Heights, NY, 1967, pp. 195–210.

[56] Champagne, F., Friehe, C., LaRue, J., and Wynagaard, J., "Flux measurements, flux estimation techniques, and fine-scale turbulence measurements in the unstable surface layer over land," *Journal of Atmospheric Sciences*, Vol. 34, No. 3, 1977, pp. 515–530.

[57] Lesieur, M. and Metais, O., "New trends in large-eddy simulations of turbulence," *Annual review of fluid mechanics*, Vol. 28, No. 1, 1996, pp. 45–82.

[58] Sreenivasan, K. R., "On the universality of the Kolmogorov constant," *Physics of Fluids*, Vol. 7, No. 11, 1995, pp. 2778–2784.

[59] Mason, P. J. and Thomson, D. J., "Stochastic backscatter in large-eddy simulations of boundary layers," *Journal of Fluid Mechanics*, Vol. 242, 1992, pp. 51–78.

[60] Piomelli, U., Cabot, W. H., Moin, P., and Lee, S., "Subgrid-scale backscatter in turbulent and transitional flows," *Physics of Fluids A: Fluid Dynamics*, Vol. 3, No. 7, 1991, pp. 1766–1771.

[61] Germano, M., Piomelli, U., Moin, P., and Cabot, W. H., "A dynamic subgrid-scale eddy viscosity model," *Physics of Fluids*, Vol. 7, 1991, pp. 1760–1765.

[62] Piomelli, U., "Large-eddy simulation-Present state and future perspectives," *36th AIAA Aerospace Sciences Meeting and Exhibit*, 1998, p. 534.

[63] Germano, M., "Turbulence: the filtering approach," *Journal of Fluid Mechanics*, Vol. 238, 1992, pp. 325–336.

[64] Lilly, D. K., "A Proposed Modification of the Germano Subgrid-scale Closure Method," *Physics of Fluids A*, Vol. 4, 1992, pp. 633–635.

[65] Vreman, B., Geurts, B., and Kuerten, H., "Large-eddy simulation of the turbulent mixing layer," *Journal of fluid mechanics*, Vol. 339, 1997, pp. 357–390.

[66] Meneveau, C. and Lund, T. S., "The dynamic Smagorinsky model and scale-dependent coefficients in the viscous range of turbulence," *Physics of fluids*, Vol. 9, No. 12, 1997, pp. 3932–3934.

[67] Cook, A. W., "Determination of the constant coefficient in scale similarity models of turbulence," *Physics of Fluids*, Vol. 9, No. 5, 1997, pp. 1485–1487.

[68] Bardina, J., Ferziger, J., and Reynolds, W., "Improved subgrid-scale models for large-eddy simulation," *13th Fluid and Plasma Dynamics Conference*, 1980, p. 1357.

[69] Bardina, J., *Improved turbulence models based on large eddy simulation of homogeneous, incompressible, turbulent flows*, Ph.D. thesis, Stanford University, 1983.

[70] Shah, K. and Ferziger, J., "A new non-eddy viscosity subgrid-scale model and its application to channel flow," *Annual Research Briefs*, 1995, pp. 73–90.

[71] Borue, V. and Orszag, S. A., "Local energy flux and subgrid-scale statistics in three-dimensional turbulence," *Journal of Fluid Mechanics*, Vol. 366, 1998, pp. 1–31.

[72] Domaradzki, J. A. and Saiki, E. M., "A subgrid-scale model based on the estimation of unresolved scales of turbulence," *Physics of Fluids*, Vol. 9, No. 7, 1997, pp. 2148–2164.

[73] Adams, N. and Stolz, S., "On the approximate deconvolution procedure for LES," *Phys. Fluids*, Vol. 2, 1999, pp. 1699–1701.

[74] Stolz, S., Adams, N. A., and Kleiser, L., "An approximate deconvolution model for large-eddy simulation with application to incompressible wall-bounded flows," *Physics of fluids*, Vol. 13, No. 4, 2001, pp. 997–1015.

[75] Pantano, C. and Sarkar, S., "A subgrid model for nonlinear functions of a scalar," *Physics of Fluids*, Vol. 13, No. 12, 2001, pp. 3803–3819.

[76] Mellado, J., Sarkar, S., and Pantano, C., "Reconstruction subgrid models for nonpremixed combustion," *Physics of fluids*, Vol. 15, No. 11, 2003, pp. 3280–3307.

[77] Langford, J. A. and Moser, R. D., "Optimal LES formulations for isotropic turbulence," *Journal of Fluid Mechanics*, Vol. 398, 1999, pp. 321.

[78] Hughes, T. J., Mazzei, L., and Jansen, K. E., "Large eddy simulation and the variational multiscale method," *Computing and visualization in science*, Vol. 3, No. 1, 2000, pp. 47–59.

[79] Hughes, T. J., Mazzei, L., Oberai, A. A., and Wray, A. A., "The multiscale formulation of large eddy simulation: decay of homogeneous isotropic turbulence," *Physics of fluids*, Vol. 13, No. 2, 2001, pp. 505–512.

[80] Hughes, T. J. R., Oberai, A. A., and Mazzei, L., "Large eddy simulation of turbulent channel flows by the variational multiscale method," *Physics of Fluids*, Vol. 13, 2001, pp. 1784–1799.

[81] Desjardins, O., Blanquart, G., Balarac, G., and Pitsch, H., "High order conservative finite difference scheme for variable density low Mach number turbulent flows," *Journal of Computational Physics*, Vol. 227, No. 15, 2008, pp. 7125–7159.

[82] Martin, M. P., Piomelli, U., and Candler, G. V., "Subgrid-scale models for compressible large-eddy simulations," *Theoretical and Computational Fluid Dynamics*, Vol. 13, No. 5, 2000, pp. 361–376.

[83] Meneveau, C. and Katz, J., "Scale-invariance and turbulence models for large-eddy simulation," *Annual Review of Fluid Mechanics*, Vol. 32, No. 1, 2000, pp. 1–32.

[84] Moin, P., "Advances in large eddy simulation methodology for complex flows," *International journal of heat and fluid flow*, Vol. 23, No. 5, 2002, pp. 710–720.

[85] Pitsch, H., "Large-Eddy Simulation of Turbulent Combustion," *Annual Review of Fluid Mechanics*, Vol. 38, 2006, pp. 453–482.

[86] Beck, A. and Kurz, M., "A perspective on machine learning methods in turbulence modeling," *GAMM-Mitteilungen*, Vol. 44, No. 1, 2021, pp. e202100002.

[87] Parish, E. J. and Duraisamy, K., "A paradigm for data-driven predictive modeling using field inversion and machine learning," *Journal of Computational Physics*, Vol. 305, 2016, pp. 758–774.

[88] Ling, J., Kurzawski, A., and Templeton, J., "Reynolds averaged turbulence modelling using deep neural networks with embedded invariance," *Journal of Fluid Mechanics*, Vol. 807, 2016, pp. 155–166.

[89] Milano, M. and Koumoutsakos, P., "Neural network modeling for near wall turbulent flow," *Journal of Computational Physics*, Vol. 182, No. 1, 2002, pp. 1–26.

[90] Maulik, R. and San, O., "A neural network approach for the blind deconvolution of turbulent flows," *arXiv preprint arXiv:1706.00912*, 2017.

[91] Bode, M., Gauding, M., Kleinheinz, K., and Pitsch, H., "Deep learning at scale for subgrid modeling in turbulent flows: regression and reconstruction," *International Conference on High Performance Computing*, Springer, 2019, pp. 541–560.

[92] Berkooz, G., Holmes, P., and Lumley, J. L., "The proper orthogonal decomposition in the analysis of turbulent flows," *Annual review of fluid mechanics*, Vol. 25, No. 1, 1993, pp. 539–575.

[93] Wang, Z., Akhtar, I., Borggaard, J., and Iliescu, T., "Proper orthogonal decomposition closure models for turbulent flows: a numerical comparison," *Computer Methods in Applied Mechanics and Engineering*, Vol. 237, 2012, pp. 10–26.

[94] Ghate, A., Towne, A., and Lele, S., "Broadband reconstruction of inhomogeneous turbulence using spectral proper orthogonal decomposition and Gabor modes," *Journal of Fluid Mechanics*, Vol. 888, 2020, pp. R1.

[95] Srinivasan, P., Guastoni, L., Azizpour, H., Schlatter, P., and Vinuesa, R., "Predictions of turbulent shear flows using deep neural networks," *Physical Review Fluids*, Vol. 4, No. 5, 2019, pp. 054603.

[96] Constantin, P., Foias, C., Nicolaenko, B., and Temam, R., *Integral manifolds and inertial manifolds for dissipative partial differential equations*, Vol. 70, Springer Science & Business Media, 2012.

[97] Constantin, P., Foias, C., Manley, O. P., and Temam, R., "Determining modes and fractal dimension of turbulent flows," *Journal of Fluid Mechanics*, Vol. 150, 1985, pp. 427–440.

[98] Foias, C., Sell, G. R., and Temam, R., "Inertial manifolds for nonlinear evolutionary equations," *Journal of differential equations*, Vol. 73, No. 2, 1988, pp. 309–353.

[99] Kaplan, J. L. and Yorke, J. A., "Chaotic behavior of multidimensional difference equations," *Functional Differential equations and approximation of fixed points*, Springer, 1979, pp. 204–227.

[100] Hassanaly, M. and Raman, V., "Lyapunov spectrum of forced homogeneous isotropic turbulent flows," *Physical Review Fluids*, Vol. 4, No. 11, 2019, pp. 114608.

[101] Berkooz, G., "An observation on probability density equations, or, when do simulations reproduce statistics?" *Nonlinearity*, Vol. 7, No. 2, 1994, pp. 313.

[102] Biferale, L., "Shell models of energy cascade in turbulence," *Annual Review of Fluid Mechanics*, Vol. 35, No. 1, 2003, pp. 441–468.

[103] Frisch, U., Sulem, P.-L., and Nelkin, M., "A simple dynamical model of intermittent fully developed turbulence," *Journal of Fluid Mechanics*, Vol. 87, No. 4, 1978, pp. 719–736.

[104] Schmid, P. J., "Dynamic mode decomposition of numerical and experimental data," *Journal of Fluid Mechanics*, Vol. 656, 2010, pp. 5–28.

[105] Rowley, C. W., Mezić, I., Bagheri, S., Schlatter, P., and Henningson, D. S., "Spectral analysis of nonlinear flows," *Journal of fluid mechanics*, Vol. 641, 2009, pp. 115–127.

[106] Brunton, S. L., Proctor, J. L., and Kutz, J. N., "Discovering governing equations from data by sparse identification of nonlinear dynamical systems," *Proceedings of the National Academy of Sciences*, 2016, pp. 201517384.

[107] Sharma, A. and McKeon, B., "On coherent structure in wall turbulence," *Journal of Fluid Mechanics*, Vol. 728, 2013, pp. 196–238.

[108] Pitsch, H., "Large-eddy simulation of turbulent combustion," *Annu. Rev. Fluid Mech.*, Vol. 38, 2006, pp. 453–482.

[109] Menon, S., "Subgrid combustion modelling for large-eddy simulations," *International Journal of Engine Research*, Vol. 1, No. 2, 2000, pp. 209–227.

[110] Fiorina, B., Veynante, D., and Candel, S., "Modeling Combustion Chemistry in Large Eddy Simulation of Turbulent Flames," *Flow, Turbulence and Combustion*, Vol. 94, 12 2014.

[111] Rieth, M., Proch, F., Stein, O., Pettit, M., and Kempf, A., "Comparison of the Sigma and Smagorinsky LES models for grid generated turbulence and a channel flow," *Computers & Fluids*, Vol. 99, 2014, pp. 172–181.

[112] Pitsch, H., Desjardins, O., Balarac, G., and Ihme, M., "Large-eddy simulation of turbulent reacting flows," *Progress in Aerospace Sciences*, Vol. 44, No. 6, 2008, pp. 466 – 478.

[113] Mueller, M. E. and Pitsch, H., "LES model for sooting turbulent nonpremixed flames," *Combustion and Flame*, Vol. 159, No. 6, 2012, pp. 2166 – 2180.

[114] Kaul, C. M. and Raman, V., "Analysis of a dynamic model for subfilter scalar dissipation rate in large eddy simulation based on the subfilter scalar variance transport equation," *Combustion Theory and Modelling*, Vol. 17, No. 5, 2013, pp. 804–834.

[115] Koo, H., Hassanaly, M., Raman, V., Mueller, M. E., and Geigle, K. P., "Large-eddy simulation of soot formation in a model gas turbine combustor," *Journal of Engineering for Gas Turbines and Power*, Vol. 139, No. 3, 2017, pp. 031503.

[116] Chen, Y. and Ihme, M., "Large-eddy simulation of a piloted premixed jet burner," *Combustion and Flame*, Vol. 160, No. 12, 2013, pp. 2896–2910.

[117] Sanjosé, M., Senoner, J., Jaegle, F., Cuenot, B., Moreau, S., and Poinsot, T., "Fuel injection model for Euler–Euler and Euler–Lagrange large-eddy simulations of an evaporating spray inside an aeronautical combustor," *International Journal of Multiphase Flow*, Vol. 37, No. 5, 2011, pp. 514–529.

[118] Boudier, G., Lamarque, N., Staffelbach, G., Gicquel, L., and Poinsot, T., "Thermo-acoustic stability of a helicopter gas turbine combustor using large eddy simulation," *International journal of Aeroacoustics*, Vol. 8, No. 1, 2009, pp. 69–93.

[119] Esposito, G. and Chelliah, H., "Skeletal reaction models based on principal component analysis: Application to ethylene–air ignition, propagation, and extinction phenomena," *Combustion and Flame*, Vol. 158, No. 3, 2011, pp. 477–489.

[120] Sung, C., Law, C., and Chen, J.-Y., "Augmented reduced mechanisms for NO emission in methane oxidation," *Combustion and Flame*, Vol. 125, No. 1-2, 2001, pp. 906–919.

[121] Pope, S. B., "Small scales, many species and the manifold challenges of turbulent combustion," *Proceedings of the Combustion Institute*, Vol. 34, No. 1, 2013, pp. 1–31.

[122] Maas, U. and Pope, S. B., "Simplifying chemical kinetics: intrinsic low-dimensional manifolds in composition space," *Combustion and flame*, Vol. 88, No. 3-4, 1992, pp. 239–264.

[123] Smooke, M. D., *Reduced kinetic mechanisms and asymptotic approximations for methane-air flames: a topical volume*, Springer, 1991.

[124] Peters, N. and Rogg, B., *Reduced kinetic mechanisms for applications in combustion systems*, Vol. 15, Springer Science & Business Media, 2008.

[125] Lam, S. and Goussis, D., "The CSP method for simplifying kinetics," *International journal of chemical kinetics*, Vol. 26, No. 4, 1994, pp. 461–486.

[126] Pierce, C. D. and Moin, P., "Progress-variable approach for large-eddy simulation of non-premixed turbulent combustion," *Journal of Fluid Mechanics*, Vol. 504, 2004, pp. 73–97.

[127] Pitsch, H. and Ihme, M., "An unsteady/flamelet progress variable method for LES of nonpremixed turbulent combustion," *43rd AIAA Aerospace Sciences Meeting and Exhibit*, 2005, p. 557.

[128] Van Oijen, J. A., *Flamelet-generated manifolds: development and application to premixed laminar flames*, Technische Universiteit Eindhoven Eindhoven, 2002.

[129] Gicquel, O., Darabiha, N., and Thévenin, D., "Liminar premixed hydrogen/air counterflow flame simulations using flame prolongation of ILDM with differential diffusion," *Proceedings of the Combustion Institute*, Vol. 28, No. 2, 2000, pp. 1901–1908.

[130] Cook, A. W. and Riley, J. J., "A subgrid model for equilibrium chemistry in turbulent flows," *Physics of fluids*, Vol. 6, No. 8, 1994, pp. 2868–2870.

[131] Ghosal, S., Lund, T. S., Moin, P., and Akselvoll, K., "A Dynamic Localization Model for Large-Eddy Simulation of Turbulent Flows," *Journal of Fluid Mechanics*, Vol. 286, 1995, pp. 229–255.

[132] Kaul, C. M., Raman, V., Knudsen, E., Richardson, E. S., and Chen, J. H., "Large eddy simulation of a lifted ethylene flame using a dynamic nonequilibrium model for subfilter scalar variance and dissipation rate," *Proceedings of the Combustion Institute*, Vol. 34, No. 1, 2013, pp. 1289–1297.

[133] Kent, J. and Bilger, R., "Turbulent diffusion flames," *Symposium (international) on combustion*, Vol. 14, Elsevier, 1973, pp. 615–625.

[134] Bilger, R., "The structure of diffusion flames," *Combustion science and technology*, Vol. 13, No. 1-6, 1976, pp. 155–170.

[135] Pitsch, H. and Steiner, H., "Scalar mixing and dissipation rate in large-eddy simulations of non-premixed turbulent combustion," *Proceedings of the Combustion Institute*, Vol. 28, No. 1, 2000, pp. 41–49.

[136] Raman, V., Pitsch, H., and Fox, R. O., "Hybrid large-eddy simulation/Lagrangian filtered-density-function approach for simulating turbulent combustion," *Combustion and Flame*, Vol. 143, No. 1-2, 2005, pp. 56–78.

[137] Bushe, W. K. and Steiner, H., "Conditional moment closure for large eddy simulation of nonpremixed turbulent reacting flows," *Physics of Fluids*, Vol. 11, No. 7, 1999, pp. 1896–1906.

[138] Vreman, A., Albrecht, B., Van Oijen, J., De Goey, L., and Bastiaans, R., "Premixed and nonpremixed generated manifolds in large-eddy simulation of Sandia flame D and F," *Combustion and Flame*, Vol. 153, No. 3, 2008, pp. 394–416.

[139] Cha, C. M., Kosály, G., and Pitsch, H., "Modeling extinction and reignition in turbulent nonpremixed combustion using a doubly-conditional moment closure approach," *Physics of Fluids*, Vol. 13, No. 12, 2001, pp. 3824–3834.

[140] Novoselov, A. G., Lacey, C. E., Perry, B. A., and Mueller, M. E., "Large Eddy Simulation of a turbulent lifted flame using multi-modal manifold-based models: Feasibility and interpretability," *Proceedings of the Combustion Institute*, 2020.

[141] Tang, Y., Hassanaly, M., Raman, V., Sforzo, B., and Seitzman, J., "Probabilistic modeling of forced ignition of alternative jet fuels," *Proceedings of the Combustion Institute*, 2020.

[142] Chrigui, M., Gounder, J., Sadiki, A., Masri, A. R., and Janicka, J., "Partially premixed reacting acetone spray using LES and FGM tabulated chemistry," *Combustion and flame*, Vol. 159, No. 8, 2012, pp. 2718–2741.

[143] Tang, Y., Koo, H., Lietz, C., and Raman, V., "Numerical Study on Flame Stabilization Mechanism of a multi-jet burner with LES Flamelet Approach," *54th AIAA Aerospace Sciences Meeting*, 2016, p. 1395.

[144] Knudsen, E. and Pitsch, H., "A general flamelet transformation useful for distinguishing between premixed and non-premixed modes of combustion," *Combustion and flame*, Vol. 156, No. 3, 2009, pp. 678–696.

[145] Mueller, M. E. and Pitsch, H., "Large Eddy Simulation of soot evolution in an aircraft combustor," *Physics of Fluids*, Vol. 25, 2013.

[146] Nguyen, P.-D., Vervisch, L., Subramanian, V., and Domingo, P., "Multidimensional flamelet-generated manifolds for partially premixed combustion," *Combustion and Flame*, Vol. 157, No. 1, 2010, pp. 43–61.

[147] Raman, V. and Pitsch, H., "Large-eddy simulation of a bluff-body-stabilized non-premixed flame using a recursive filter-refinement procedure," *Combustion and flame*, Vol. 142, No. 4, 2005, pp. 329–347.

[148] Givi, P., "Filtered density function for subgrid scale modeling of turbulent combustion," *AIAA journal*, Vol. 44, No. 1, 2006, pp. 16–23.

[149] Knudsen, E., Richardson, E., Doran, E., Pitsch, H., and Chen, J., "Modeling scalar dissipation and scalar variance in large eddy simulation: Algebraic and transport equation closures," *Physics of Fluids*, Vol. 24, No. 5, 2012, pp. 055103.

[150] Menon, S. and Kerstein, A. R., "The linear-eddy model," *Turbulent combustion modeling*, Springer, 2011, pp. 221–247.

[151] Klimenko, A. Y. and Pope, S. B., "The Modeling of Turbulent Reactive Flows Based on Multiple Mapping Conditioning," *Physics of Fluids*, Vol. 15, No. 7, 2003, pp. 1907–1925.

[152] Colucci, P. J., Jaberi, F. A., Givi, P., and Pope, S. B., "Filtered density function for large eddy simulation of turbulent reacting flows," *Physics of Fluids*, Vol. 10, 1998, pp. 499–515.

[153] Raman, V. and Pitsch, H., "A consistent LES/filtered-density function formulation for the simulation of turbulent flames with detailed chemistry," *Proceedings of the Combustion Institute*, Vol. 31, No. 2, 2007, pp. 1711–1719.

[154] Domingo, P. and Vervisch, L., "Large eddy simulation of premixed turbulent combustion using approximate deconvolution and explicit flame filtering," *Proceedings of the Combustion Institute*, Vol. 35, No. 2, 2015, pp. 1349–1357.

[155] Domingo, P. and Vervisch, L., "DNS and approximate deconvolution as a tool to analyse one-dimensional filtered flame sub-grid scale modelling," *Combustion and Flame*, Vol. 177, 2017, pp. 109–122.

[156] Wang, Q. and Ihme, M., "Regularized deconvolution method for turbulent combustion modeling," *Combustion and Flame*, Vol. 176, 2017, pp. 125–142.

[157] Mathew, J., "Explicit filtering for large eddy simulation as use of a spectral buffer," *arXiv preprint arXiv:1610.01738*, 2016.

[158] Mehl, C., Idier, J., and Fiorina, B., "Evaluation of deconvolution modelling applied to numerical combustion," *Combustion Theory and Modelling*, Vol. 22, No. 1, 2018, pp. 38–70.

[159] Gravemeier, V. and Wall, W. A., "An algebraic variational multiscale–multigrid method for large-eddy simulation of turbulent variable-density flow at low Mach number," *Journal of Computational Physics*, Vol. 229, No. 17, 2010, pp. 6047–6070.

[160] Gravemeier, V. and Wall, W. A., "Variational multiscale methods for premixed combustion based on a progress-variable approach," *Combustion and flame*, Vol. 158, No. 6, 2011, pp. 1160–1170.

[161] R, F. C. T., "Some analytic and geometric properties of the solutions of the evolution Navier-Stokes equations," *J. MATH. PURES APPL.*, Vol. 58, pp. 339–368.

[162] Constantin, P., Foiaş, C., and Temam, R., *Attractors representing turbulent flows*, Vol. 314, American Mathematical Soc., 1985.

[163] Foias, C. and Temam, R., "Approximation of Attractors by Algebraic or Analytic Sets," *SIAM Journal of Mathematical Analysis*, Vol. 25, 1994, pp. 1269–1302.

[164] Castañeda, N. and Rosa, R., "Optimal estimates for the uncoupling of differential equations," *Journal of Dynamics and Differential Equations*, Vol. 8, No. 1, 1996, pp. 103–139.

[165] Lam, S. and Goussis, D., "Understanding complex chemical kinetics with computational singular perturbation," *Symposium (International) on Combustion*, Vol. 22, Elsevier, 1989, pp. 931–941.

[166] Valorani, M. and Paolucci, S., "The G-Scheme: A framework for multi-scale adaptive model reduction," *Journal of Computational Physics*, Vol. 228, No. 13, 2009, pp. 4665–4701.

[167] Mori, H., "Transport, collective motion, and Brownian motion," *Progress of theoretical physics*, Vol. 33, No. 3, 1965, pp. 423–455.

[168] Zwanzig, R., "Nonlinear generalized Langevin equations," *Journal of Statistical Physics*, Vol. 9, No. 3, 1973, pp. 215–220.

[169] Gouasmi, A., Parish, E. J., and Duraisamy, K., "A priori estimation of memory effects in reduced-order models of nonlinear systems using the Mori–Zwanzig formalism," *Proceedings of the Royal Society A: Mathematical, Physical and Engineering Sciences*, Vol. 473, No. 2205, 2017, pp. 20170385.

[170] Parish, E. J. and Duraisamy, K., "Non-Markovian closure models for large eddy simulations using the Mori-Zwanzig formalism," *Physical Review Fluids*, Vol. 2, No. 1, 2017, pp. 014604.

[171] Parish, E. J. and Duraisamy, K., "A dynamic subgrid scale model for large eddy simulations based on the Mori–Zwanzig formalism," *Journal of Computational Physics*, Vol. 349, 2017, pp. 154–175.

[172] Foias, C., Sell, G. R., and Titi, E. S., "Exponential tracking and approximation of inertial manifolds for dissipative nonlinear equations," *Journal of Dynamics and Differential Equations*, Vol. 1, No. 2, 1989, pp. 199–244.

[173] Demengel, F. and Ghidaglia, J.-M., "Inertial manifolds for partial differential evolution equations under time-discretization: existence, convergence, and applications," *Journal of Mathematical Analysis and Applications*, Vol. 155, No. 1, 1991, pp. 177–225.

[174] Jolly, M., Kevrekidis, I., and Titi, E., "Approximate inertial manifolds for the Kuramoto-Sivashinsky equation: analysis and computations," *Physica D: Nonlinear Phenomena*, Vol. 44, No. 1-2, 1990, pp. 38–60.

[175] Chung, Y.-M. and Jolly, M., "A unified approach to compute foliations, inertial manifolds, and tracking solutions," *Mathematics of Computation*, Vol. 84, No. 294, 2015, pp. 1729–1751.

[176] Constantin, P., Foias, C., Nicolaenko, B., and Temam, R., "Integral manifolds and inertial manifolds for dissipative partial differential equations," *Math. Sci. Ser*, Vol. 70, 1988.

[177] Marion, M., "Approximate inertial manifolds for reaction-diffusion equations in high space dimension," *Journal of Dynamics and Differential Equations*, Vol. 1, No. 3, 1989, pp. 245–267.

[178] Jolly, M. S., "Explicit construction of an inertial manifold for a reaction diffusion equation," *Journal of Differential Equations*, Vol. 78, No. 2, 1989, pp. 220–261.

[179] Mallet-Paret, J. and Sell, G. R., "Inertial manifolds for reaction diffusion equations in higher space dimensions," *Journal of the American Mathematical Society*, Vol. 1, No. 4, 1988, pp. 805–866.

[180] Doering, C. R., Gibbon, J. D., Holm, D. D., and Nicolaenko, B., "Low-dimensional behaviour in the complex Ginzburg-Landau equation," *Nonlinearity*, Vol. 1, No. 2, 1988, pp. 279.

[181] Ghidaglia, J.-M. and Héron, B., "Dimension of the attractors associated to the Ginzburg-Landau partial differential equation," *Physica D: Nonlinear Phenomena*, Vol. 28, No. 3, 1987, pp. 282–304.

[182] Constantin, P., Foias, C., Nicolaenko, B., and Témam, R., "Spectral barriers and inertial manifolds for dissipative partial differential equations," *Journal of Dynamics and Differential Equations*, Vol. 1, No. 1, 1989, pp. 45–73.

[183] Foias, C., Nicolaenko, B., Sell, G. R., and Temam, R., "Inertial manifolds for the Kuramoto-Sivashinsky equation and an estimate of their lowest dimension," 1988.

[184] Fabes, E., Luskin, M., and Sell, G. R., "Construction of inertial manifolds by elliptic regularization," *Journal of Differential Equations*, Vol. 89, No. 2, 1991, pp. 355–387.

[185] Foias, C., Manley, O., and Temam, R., "Modelling of the interaction of small and large eddies in two dimensional turbulent flows," *ESAIM: Mathematical Modelling and Numerical Analysis*, Vol. 22, No. 1, 1988, pp. 93–118.

[186] Foias, C. and Temam, R., "The algebraic approximation of attractors: The finite dimensional case," *Physica D: Nonlinear Phenomena*, Vol. 32, No. 2, 1988, pp. 163–182.

[187] Titi, E. S., "On approximate inertial manifolds to the Navier-Stokes equations," *Journal of Mathematical Analysis and Applications*, Vol. 149, No. 2, 1990, pp. 540–557.

[188] Shvartsman, S. Y. and Kevrekidis, I. G., "Nonlinear model reduction for control of distributed systems: A computer-assisted study," *AIChE Journal*, Vol. 44, No. 7, 1998, pp. 1579–1595.

[189] Chen, W., "Approximate inertial manifolds for 2D Navier-Stokes equations," *Journal of Mathematical Analysis and Applications*, Vol. 165, No. 2, 1992, pp. 399–418.

[190] Adrover, A., Continillo, G., Crescitelli, S., Giona, M., and Russo, L., "Construction of approximate inertial manifold by decimation of collocation equations of distributed parameter systems," *Computers & Chemical Engineering*, Vol. 26, No. 1, 2002, pp. 113–123.

[191] Jauberteau, F., Rosier, C., and Temam, R., "A nonlinear Galerkin method for the Navier-Stokes equations," *Computer Methods in Applied Mechanics and Engineering*, Vol. 80, No. 1-3, 1990, pp. 245–260.

[192] Chueshov, I., "Approximate inertial manifolds of exponential order for semilinear parabolic equations subjected to additive white noise," *Journal of Dynamics and Differential Equations*, Vol. 7, No. 4, 1995, pp. 549–566.

[193] Guermond, J.-L. and Prudhomme, S., "A fully discrete nonlinear Galerkin method for the 3D Navier-Stokes equations," *Numerical Methods for Partial Differential Equations: An International Journal*, Vol. 24, No. 3, 2008, pp. 759–775.

[194] Foias, C. and Titi, E. S., "Determining nodes, finite difference schemes and inertial manifolds," *Nonlinearity*, Vol. 4, No. 1, 1991, pp. 135.

[195] Margolin, L. and Jones, D., "An approximate inertial manifold for computing Burgers' equation," *Physica D: Nonlinear Phenomena*, Vol. 60, No. 1-4, 1992, pp. 175–184.

[196] Bollt, E., "Attractor modeling and empirical nonlinear model reduction of dissipative dynamical systems," *International Journal of Bifurcation and Chaos*, Vol. 17, No. 04, 2007, pp. 1199–1219.

[197] Chorin, A. J. and Lu, F., "Discrete approach to stochastic parametrization and dimension reduction in nonlinear dynamics," *Proceedings of the National Academy of Sciences*, Vol. 112, No. 32, 2015, pp. 9804–9809.

[198] Lu, F., Lin, K. K., and Chorin, A. J., "Data-based stochastic model reduction for the Kuramoto–Sivashinsky equation," *Physica D: Nonlinear Phenomena*, Vol. 340, 2017, pp. 46–57.

[199] Kang, W., Zhang, J.-Z., Ren, S., and Lei, P.-F., "Nonlinear Galerkin method for low-dimensional modeling of fluid dynamic system using POD modes," *Communications in Nonlinear Science and Numerical Simulation*, Vol. 22, No. 1-3, 2015, pp. 943–952.

[200] Budanur, N. B. and Cvitanović, P., "Unstable manifolds of relative periodic orbits in the symmetry-reduced state space of the Kuramoto-Sivashinsky system," *Journal of Statistical Physics*, Vol. 167, No. 3-4, 2017, pp. 636–655.

[201] Foias, C., Nicolaenko, B., Sell, G. R., and Temam, R., "Inertial manifolds for the Kuramoto-Sivashinsky equation and an estimate of their lowest dimension," 1986.

[202] Michelson, D. and Sivashinsky, G., "Nonlinear analysis of hydrodynamic instability in laminar flames—II. Numerical experiments," *Acta Astronautica*, Vol. 4, No. 11-12, 1977, pp. 1207–1221.

[203] Lin, S., "Finite amplitude side-band stability of a viscous film," *Journal of Fluid Mechanics*, Vol. 63, No. 3, 1974, pp. 417–429.

[204] Kuramoto, Y., "Diffusion-induced chaos in reaction systems," *Progress of Theoretical Physics Supplement*, Vol. 64, 1978, pp. 346–367.

[205] Hyman, J. M. and Nicolaenko, B., "The Kuramoto-Sivashinsky equation: a bridge between PDE's and dynamical systems," *Physica D: Nonlinear Phenomena*, Vol. 18, No. 1-3, 1986, pp. 113–126.

[206] Kassam, A.-K. and Trefethen, L. N., "Fourth-order time-stepping for stiff PDEs," *SIAM Journal of Scientific Computing*, Vol. 26, 2005, pp. 1214–1233.

[207] Cox, S. M. and Matthews, P. C., "Exponential time differencing for stiff systems," *Journal of Computational Physics*, Vol. 176, No. 2, 2002, pp. 430–455.

[208] Foias, C., Sell, G. R., and Temam, R., "Variétés inertielles des équations différentielles dissipatives," *Comptes rendus de l'Académie des sciences. Série 1, Mathématique*, Vol. 301, No. 5, 1985, pp. 139–141.

[209] Benettin, G., Galgani, L., Giorgilli, A., and Strelcyn, J.-M., "Lyapunov characteristic exponents for smooth dynamical systems and for Hamiltonian systems; A method for computing all of them. Part 2: Numerical application," *Meccanica*, Vol. 15, 1980, pp. 21–30.

[210] Pope, S. B., "Ten questions concerning the large-eddy simulation of turbulent flows," *New journal of Physics*, Vol. 6, No. 1, 2004, pp. 35.

[211] Rosales, C. and Meneveau, C., "Linear forcing in numerical simulations of isotropic turbulence: Physical space implementations and convergence properties," *Physics of Fluids*, Vol. 17, No. 9, 2005, pp. 095106.

[212] Lundgren, T. S., "Linearly forced isotropic turbulence," *CTR Annual Research Briefs*, Center for Turbulence Research, CTR, Stanford University, 2003, pp. 461–473.

[213] Hassanaly, M., *Extreme events in turbulent combustion*, Ph.D. thesis, University of Michigan, Ann Arbor, MI, 2019.

[214] Eswaran, V. and Pope, S. B., "An examination of forcing in direct numerical simulations of turbulence," *Computers & Fluids*, Vol. 16, No. 3, 1988, pp. 257–278.

[215] Woźniakowski, H., "Numerical stability for solving nonlinear equations," *Numerische Mathematik*, Vol. 27, No. 4, 1976, pp. 373–390.

[216] Rogers, M. M. and Moin, P., "Helicity fluctuations in incompressible turbulent flows," *The Physics of Fluids*, Vol. 30, No. 9, 1987, pp. 2662–2671.

[217] McMillan, J. and Ferziger, J. H., "Direct testing of subgrid-scale models," *AIAA Journal*, Vol. 17, No. 12, 1979, pp. 1340–1346.

[218] Clark, R. A., Ferziger, J. H., and Reynolds, W. C., "Evaluation of subgrid-scale models using an accurately simulated turbulent flow," *Journal of Fluid Mechanics*, Vol. 91, No. 1, 1979, pp. 1–16.

[219] Lilly, K., "The representation of small-scale turbulence in numerical simulation experiments," 1966.

[220] Rosales, C. and Meneveau, C., "Linear forcing in numerical simulations of isotropic turbulence: Physical space implementations and convergence properties," *Physics of Fluids*, Vol. 17, 2005.

[221] Kops, S. M. D. B., *Numerical simulation of non-premixed turbulent combustion*, Ph.D. thesis, University of Washington, 1999.

[222] Pitsch, H., Cha, C. M., and Fedotov, S., "Flamelet modelling of non-premixed turbulent combustion with local extinction and re-ignition," *Combustion Theory and Modelling*, Vol. 7, No. 2, 2003, pp. 317–332.

[223] Lee, Y. Y. and Pope, S. B., "Nonpremixed turbulent reacting flow near extinction," *Combustion and Flame*, Vol. 101, 1995, pp. 501–528.

[224] Cuenot, B. and Poinsot, T., "Asymptotic and numerical study of diffusion flames with variable Lewis number and finite rate chemistry," *Combustion and Flame*, Vol. 104, 1996, pp. 111–137.

[225] Vervisch, L. and Poinsot, T., "Direct numerical simulation of non-premixed turbulent flames," *Annual review of fluid mechanics*, Vol. 30, No. 1, 1998, pp. 655–691.

[226] Moin, P. and Mahesh, K., "Direct numerical simulation: a tool in turbulence research," *Annual review of fluid mechanics*, Vol. 30, No. 1, 1998, pp. 539–578.

[227] Orszag, S. A. and Patterson Jr, G., "Numerical simulation of three-dimensional homogeneous isotropic turbulence," *Physical Review Letters*, Vol. 28, No. 2, 1972, pp. 76.

[228] Orszag, S. A., "On the elimination of aliasing in finite-difference schemes by filtering high-wavenumber components," *Journal of the Atmospheric sciences*, Vol. 28, No. 6, 1971, pp. 1074–1074.

[229] Hochbruck, M. and Ostermann, A., "Explicit exponential Runge–Kutta methods for semilinear parabolic problems," *SIAM Journal on Numerical Analysis*, Vol. 43, No. 3, 2005, pp. 1069–1090.

[230] Schulze, J. C., Schmid, P. J., and Sesterhenn, J. L., "Exponential time integration using Krylov subspaces," *International journal for numerical methods in fluids*, Vol. 60, No. 6, 2009, pp. 591–609.

[231] Eswaran, V. and Pope, S. B., "Direct Numerical Simulations of the Turbulent Mixing of a Passive Scalar," *Physics of Fluids*, Vol. 31, 1988, pp. 506.

[232] Sripakagorn, P., Mitarai, S., Kosály, G., and Pitsch, H., "Extinction and reignition in a diffusion flame: a direct numerical simulation study," *Journal of Fluid Mechanics*, Vol. 518, 2004, pp. 231–259.

[233] Stolz, S. and Adams, N. A., "An approximate deconvolution procedure for large-eddy simulation," *Physics of Fluids*, Vol. 11, No. 7, 1999, pp. 1699–1701.

[234] Germano, M., "A new deconvolution method for large eddy simulation," *Physics of Fluids*, Vol. 21, No. 4, 2009, pp. 045107.

[235] Jiménez, C., Ducros, F., Cuenot, B., and Bédat, B., "Subgrid scale variance and dissipation of a scalar field in large eddy simulations," *Physics of Fluids*, Vol. 13, No. 6, 2001, pp. 1748–1754.

[236] Dopazo, C. and Valiño, L., "PDF approach and stochastic models of the turbulent mixing of inert and reactive statistically homogeneous scalar fields," *Transport Theory and Statistical Physics*, Vol. 23, No. 1-3, 1994, pp. 339–361.

[237] Cha, C. M. and Trouillet, P., "A model for the mixing time scale of a turbulent reacting scalar," *Physics of Fluids*, Vol. 15, No. 6, 2003, pp. 1375–1380.

[238] Peters, N., *Turbulent Combustion*, Cambridge University Press, Cambridge, United Kingdom, 2000.

[239] Farazmand, M. and Sapsis, T. P., "Closed-loop adaptive control of extreme events in a turbulent flow," *Physical Review E*, Vol. 100, No. 3, 2019, pp. 033110.

[240] Blonigan, P. J., Farazmand, M., and Sapsis, T. P., "Are extreme dissipation events predictable in turbulent fluid flows?" *arXiv preprint arXiv:1807.10263*, 2018.